Linear and Non-linear Optical Properties, Surface Plasmon Resonance and Surface Scaling Behaviour of Nanostructured Cu Thin Films Fabricated via PLD Technique

A Thesis submitted in partial fulfillment of the requirements for the award of the degree of

DOCTOR OF PHILOSOPHY

by

RAHUL KESARWANI

DEPARTMENT OF PHYSICS

INDIAN INSTITUTE OF TECHNOLOGY GUWAHATI

GUWAHATI- 781039, INDIA

April 2019

Dedicated to my Parents

Rahul Kesarwani
Registration No. 126121002
Department of Physics
Indian Institute of Technology Guwahati
Guwahati-781039, Assam, India

Statement

I hereby declare that the matter embodied in this thesis is the result of investigations carried out by me at the Department of Physics, Indian Institute of Technology Guwahati, Guwahati, India, under the supervision of **Prof. Alika Khare**. This thesis has not been submitted to any university, institute or elsewhere for the award of the any degree, diploma or associate-ship.

Date: ……. **Rahul Kesarwani**

भारतीय प्रौद्योगिकी संस्थान गुवाहाटी
Indian Institute of Technology Guwahati
Department of Physics
Guwahati-781039, Assam State, INDIA
Phone: +91 361 2582705, 2582701, 2690321 to 328 (extn. 2705),
Fax: +91 361 2582749
Dr. Alika Khare
Professor
E-mail: alika@iitg.ac.in, k_alika@yahoo.com

Date: April , 2019

Certificate

This is to certify that work contained in the thesis entitled '**Linear and Non- linear Optical Properties, Surface Plasmon Resonance and Surface Scaling Behaviour of Nanostructured Cu Thin Films Fabricated via PLD Technique**' by **Mr Rahul Kesarwani** (Roll no 126121002), a student of Department of Physics, Indian Institute of Technology Guwahati, for the award of degree of Doctor of Philosophy, has been carried out under my supervision and the same has not been submitted elsewhere for the award of any other degree.

(Alika Khare)

ACKNOWLEDGEMENTS

First and foremost, I would like to thank my research supervisor, Prof. Alika Khare, for her constant support, precious advice, guidance, and supervision of the research which helped in the completion of my PhD thesis. She gave me intellectual freedom in my work and endless hours discussion to improve the quality work in all my endeavors. I am fortunate enough that I had the opportunity to work as a student under her supervision.

I am also grateful to my doctoral committee members, Prof. Seenipandian Ravi, Prof. Bosanta Ranjan Boruah, Dr. Sukanya Sharma and Dr. Shrikrishna N. Joshi for their timely reviewing and invaluable suggestions, which helped me to improve the work pertaining to PhD thesis.

I owe my thanks to present and former Head of Department of Physics, IIT Guwahati and Head of the CIF, IIT Guwahati for providing me the necessary facilities to fulfill my PhD thesis objectives. I extend my gratitude to all the faculty members of the department of physics, who supported me in several ways during this period. I would like to extend my sincere thanks to Dr. Sidananda Sarma, Mr. Chandan Burgohain, Dr. K. K. Senapati, Mr. Madhurjya Borah, Dr. Ashim Malakar and all the staffs of Physics dept. of IIT Guwahati for their kind help with various instruments.

I would like to thank MHRD, India and IIT Guwahati for providing financial assistance during my Ph.D. tenure.

It was pleasure to work with my research lab members Dr. Abu, Dr. Satchi, Dr. Indrajeet, Dr. Partha Pritam Dey, Dr. Poulami, Dr. Gyan Prakash, Dr. Shanta Kumar, Prahlad, Eshita, Gobinda, Sasmita, Sumit and Nagendra. Thanks to them for their suggestions, time, help in experiments, improving my English writing skill and kindness throughout my PhD. I am thankful to Dr. Partha Pritam Dey specially for helping me on the thin film growth analysis.

I am deeply indebted to all my friends at IIT Guwahati; Dr. Krapa, Dr. Soumen saha, Sourab, Dr. Upendra Awasthi, Ajeet, Dr. Garima, Dr. Sachin, Dr. Ram, Jitendra, Dr. Nitin, Shibananda, Bibhuti, Dr. Ramiz, Kallol, Dr. Abhijeet, Dr. Koushik, Dr. Ashis, Dr. Anabil, Dr. Sudin, Venki, Dr. Ramesh, Dr. Himanshu bhaiya, Dr. Dillip bhaiya, Dr. Onkar bhaiya, Dr. Asha, Dr. Rama, Dr. Sandeep, Dr. Biplob, Anand, Pratap, Dr. Rasmi, Dr. Biswajit Pathak, Ashish Yadav, Debu, Durgesh, Sritam, Dr. Rahul, Dr. Surjit Halder, Dr. Mahesh and others for providing a soothing environment and helping in the critical situations during my PhD, whenever I needed. I must acknowledge all my school and university friends and my PhD batch mates for their love, encouragement and support.

My special thanks and appreciation goes to my lovely parents, my brother, sister in-law, my nephew Darsh (Babu) as well as my family for their blessings, love, patience, support and understanding throughout my studies and most of all to the Almighty Nature who governs everything.

Rahul Kesarwani

Abstract

The present thesis was aimed towards the fabrication and characterization of semi-transparent nanostructured copper thin films via pulsed laser deposition technique. The linear and nonlinear optical properties and surface plasmon resonance of Cu thin films have been studied and these properties were correlated with the size and shape of the nanoparticles, surface morphology, growth dynamics and stoichiometry of the film.

The two sets of nanostructured Cu thin films were fabricated via pulsed laser deposition. The first set is deposited at room temperature as a function of deposition duration (4, 6 and 8 minutes) followed by gradual annealing up to 400°C. The second set of the films deposited directly at the substrate temperature of 400°C for the duration of 6 to 45 minutes.

The particle size distribution, surface characteristic parameters, surface scaling behaviour, power spectral density function, activation energy etc. of these films were estimated using atomic force microscopy images. The fractal nature of the as-deposited room temperature Cu film was marginal and extreme fractal but the post annealed films to a final temperature of 400ºC, the fractal nature changed to Brownian fractal irrespective of deposition time which signifies self-affine nature of the film surface.

The films deposited directly at 400ºC showed the self-affine surface up to the deposition time of 20 minutes and for longer deposited time the films reflected the mounded surface growth. The surface scaling behaviour of these films was studied from the analysis of height-height correlation function extracted from corresponding atomic force microscopy images and the scaling exponents; roughness exponent(α'), growth exponent(β') and dynamic exponent($1/z'$) of the films were estimated. From the values of the scaling exponents, it was inferred that the growth dynamics of the films was governed by shadowing mechanism due to angular nature of deposited flux arriving on the substrate from laser induced plasma and highly sticking substrate (deposition performed at substrate softening temperature ~ 400ºC).

The plasmonic features of the films were observed by recording the absorption spectra via UV-visible spectrometer. The SPR peaks of Cu films exhibited both longitudinal and transverse mode where the peak energies were found to be dependent on size, shape and aspect ratio of the Cu nanoparticles. The Bruggeman effective medium

approximation theory was applied to determine the film composition whereas the formation of the interfacial layer and plasmonic behaviour of these copper thin films deposited on the glass substrate as a function of deposition time were investigated via spectroscopic ellipsometry spectra. It was observed that as-deposited films followed the two oscillators (one Lorentz and one Gauss) dispersion model whereas gradually annealed films to a final temperature of 400°C satisfied the four oscillators (one Lorentz and three Gauss) model. SPR peaks estimated from spectroscopic ellipsometer analysis complemented well with that of observed in UV studies.

The third order nonlinear optical properties of nanostructured Cu thin films were carried out by using modified Z-scan technique under cw He-Ne laser at 632.8 nm wavelength. The Cu thin film deposited at a substrate temperature of 400°C having particle size less than 14 nm, exhibited reserve saturation absorption behaviour whereas all the other samples deposited at elevated temperature displayed saturation absorption behaviour having values of nonlinear absorption coefficient in the range of ~ 11 to 68 cm/W. The nonlinear refractive index coefficient of all the thin films showed a self-focusing properties where the value of n_2 was observed to be in the range of ~ 1.40×10^{-4} to 4.53×10^{-4} cm^2/W. These coefficients were observed to be dependent on the deposition temperature and the size of the nanoparticles. Finally, the viability of nanostructured Cu thin film as surface enhanced Raman scattering substrate for metallic single wall carbon nanotube was also tested.

CONTENTS

LIST OF FIGURES

LIST OF TABLES

ABBREVIATIONS

AFM – Atomic Force Microscopy

ALD – Atomic Layer deposition

BEMA – Bruggeman's effective medium approximation

CA – Closed Aperture

CCD – Charged Coupled Device

Config – Configuration

CL – Correaltion length

CVD – Chemical Vapor Deposition

cw – Continuous Wave

DMF – Dimethyl formamide

EDX – Electron Diffraction X-Ray

EM – Electromagnetic

FESEM – Field-Effect Scanning Electron Microscopy

FD – Fractal dimension

FFT – Fast Fourier Transformation

FWHM – Full Width at Half Maximum

FWM – Four Wave Mixing

HE – Hurst Exponent

He-Ne - Helium-Neon

HHCF – Height-Height Correlation function

LA – Longitudinal Mode

MBE – Molecular Beam Epitaxy

MR – Micro-roughness

M-SWCNT – Metallic Single-Wall Carbon Nanotubes

Nd:YAG – Neodymium-doped Yttrium Aluminium Garnet

NLO – Non Linear Optical

NLR – Non Linear Refraction

OA – Open Aperture

OL – Optical Limiting

OPA – Optical Parametric amplification

PL – Photo Luminescence

PLD – Pulsed Laser Deposition

PSDF – Power Spectral Density Function

RBM – Radial Breathing Mode

RMS – Root Mean Square

RMSE – Root Mean Square Error

RSA – Reverse Saturation Absorption

RT – Room Temperature

SA – Saturation Absorption

SE – Spectroscopic Ellipsometry

SEA – Spectroscopy Ellipsometry Analyzer

SERS – Surface Enhanced Raman Spectroscopic

SHG – Second Harmonic Generation

SPs – Surface Plasmons

SPM – Self-Phase Modulation

SPR – Surface Plasmon Resonance

SFM – Sum Frequency Generation

TM – Transverse Mode

THE – Third Harmonic Generation

UV – Ultra Violet

UV-Vis-NIR – Ultra Violet-Visible-Near Infrared

XRD – X-Ray Diffraction

SYMBOLS

~	approximately
α	linear absorption coefficient
α'	roughness exponent
β	nonlinear absorption coefficient
β'	growth exponent
Ψ	amplitude ratio of p- and s - electric field
δ_d	Penetration depth of dielectric
δ_m	penetration depth of metal
Δ	phase difference between *p*- and *s*- polarization
°C	degree Celsius
ε_o	free space permittivity
ε_1	real part of dielectric function
ε_2	imaginary part of dielectric function
ε_d	dielectric constant of material
ε_{eff}	complex effective dielectric
ε_m	dielectric constant of metal
ε_∞	residual polarization
ξ	lateral correlation length
Γ	bandwidth of SPR
Γ_o	damping constant
λ	wavelength of light
ρ	Fresnel reflection coefficient
ϕ	incident angle of plane polarized light
v_f	velocity of conduction electron
ν	spectral indies
ω_{RBM}	Raman shift of RBM band
η	noise
μm	micrometre
A	scattering process
Ag	Silver
Au	Gold
c	speed of light
cm	centimetre
Cu	copper
Cu (II)	diatomic copper
CuO	cupric oxide
Cu_2O	cuprous oxide
d	particle size
d'	dimension
d''	diameter of M-SWCNT
D	surface diffusion coefficient
D'	laser beam diameter
D_f	fractal dimension
Δz_{p-v}	separation between peak and valley position
eV	electron volt
E_a	activation energy
E_F	Fermi energy

E_i	incident electric field
E_{ip}	incident electric field for *p*-polarization
E_{is}	incident electric field for *s*-polarization
E_r	reflected electric field
E_{rp}	reflected electric field for *p*-polarization
E_{rs}	reflected electric field for *s*-polarization
f	focal length
h	surface height
HE	Hurst parameter
I_o	peak intensity at focus
I	Intensity
J	Joule
k	spatial frequency
k_m	characteristic peak
k'	extinction coefficient
k_B	Boltzmann constant
K'	spectral Strength
L	film thickness
L_{eff}	effective sample length
mbar	millibar
n	linear refractive index
N	surface density of nanoparticle
n_2	nonlinear refractive index coefficient
nm	nanometre
m	local slope
r_p	Fresnel reflection coefficient of p- polarization
r_s	Fresnel reflection coefficient of p- polarization
S	aperture size
Si	Silicon
SiO_2	glass
t	deposition time
T_{closed}	closed aperture transmittance
T_{open}	open aperture transmittance
T	Substrate temperature
w	RMS roughness
w_o	Beam diameter at focus
z	sample position w.r.t. focus
z_o	Rayleigh length

Chapter 1

Introduction

Nanostructured metallic thin films are a great potential candidate towards tunable optical devices, plasmonic devices, optoelectronic [1], integrated circuit chips [2], microprocessors [3], solar cells, [4] sensors [5] etc. The performance of the nanostructured metallic thin film based devices is highly dependent on the surface roughness, thickness, volume fraction of the constituent species of metal, composition of the interfacial layer between the substrate and film apart from linear and nonlinear optical properties, plasmonic behaviour and electrical properties [6-11]. The nanostructured thin films of noble metals (Cu, Ag, Au), fabricated onto the suitable dielectric like glass, exhibit the surface plasmons (SPs) phenomena [12-16]. SPs are the collective oscillations of the free electrons at the metal-dielectric interface and confined on the metallic surface which decays exponentially in the neighbouring media [14]. The resonant interaction between electrons near the surface of the metal and the electromagnetic field of the incident radiation results in a phenomenon called surface plasmon resonance (SPR) [17]. SPR form the root for near-field spectroscopy, surface enhanced Raman spectroscopy (SERS), enormously large data storage, sensors, solar cells etc. [14, 18-20]. Thus it can be utilized to fabricate fast plasmonics circuits, bio-sensors, plasmonic chips, photonic devices, waveguides, etc. [1, 2, 21-23]. The SPs has many applications in bio-sensing and healthcare [24, 25], optoelectronic and microelectronics [3, 26, 27], chemical and biological sensors [28-30], thermal therapy [31] etc. The response time of SPR is of the order of picosecond [32]. The SPR properties depend on the kind of metal nanoparticles and their size, shape, type of surrounding dielectric and interfacial layer between metal-dielectric interface [11, 33, 34]. The optical properties of nanostructured thin film, also depends on the type of surface

growth and related parameters e.g. roughness, correlation length, type of surface etc. [11, 33-36]. Noble metal nanoparticles such as gold (Au), silver (Ag), and copper (Cu) have been studied extensively because of their large plasmonic properties, nonlinear optical (NLO) response, photoluminescence (PL) and physicochemical properties etc. [1, 2, 12, 28, 37-52].

The nanostructured films also possess large optical nonlinearity. The optical nonlinearity plays an important role in making fast photonic and electronic devices [53]. The noble metal nanoparticles embedded in dielectric have been studied extensively because of their large third-order optical nonlinearity [50] and fast response time which leads to its potential application in all-optical switching devices [54]. The SPs has a significant role in enhancing the optical nonlinearity of the nanostructured thin films [49]. The nonlinearity of the noble metals is basically due to the contribution of intraband transition, interband transition and hot electron formation [55].

Among various noble metals, Cu is one of the most suitable and extensively used material because of its high thermal and electrical conductivity and low electro-migration rate [56, 57]. Cu has a large number of interband energy levels in the range of 1.2 – 5.6 eV [58-61]. These interband transitions are responsible for SPs, PL etc. in the Cu nanoparticles [52, 62-65]. The nanostructured Cu thin film can exhibit saturation absorption (SA) and reverse saturation absorption (RSA) behaviour [12, 49, 66], thereby it can be used as optical limiters [67]. Cu also finds application in the area of medicine, electronics, optics, manufacturing of lubrication nanofluids, filler, conductive films, antimicrobial, antiseptic material, metallic inks, wound dressing and biocidal properties, gas sensors, catalytic process, high-temperature superconductors, high-speed devices, solar cells [68-74] etc. It is an excellent candidate for making interconnects in the integrated circuit on the dielectric substrate [75].

1.1. Surface Plasmon Resonance

The surface plasmons (SPs) are the collective oscillations of the free electrons associated with metal at metal-dielectric interface [17]. SPs are confined on the metallic surface with an exponentially decaying field in the neighbouring media [14] as shown in *figure 1. Figure 1.1 (a)* illustrate the formation of SPs at the metal-dielectric interface. *Figure 1.1 (b)* represents pictorially the exponentially the local electric field near the surface with distance in a direction normal to the interface along with the penetration depth of SPs wave, δ_d and δ_m into the dielectric and metal, respectively.

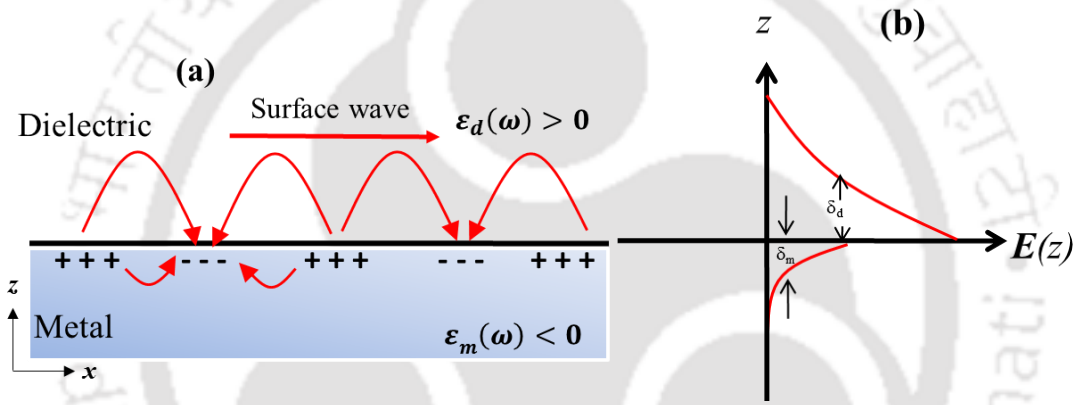

Figure 1.1 *(a) Schematic illustration of electromagnetic wave and surface charges at the interface between the metal and dielectric material and (b) penetration depth of SPs field around the interface.*

There are two types of decaying field in the surface plasmon waves; radiative and non-radiative. The radiative decay of SP is dominant in the films having rough surface due to the scattering of incident light while the non-radiative decay of SP is due to the absorption of radiation and is more pronounced in the films having smooth surface [76]. The resonant interaction between the electrons near the surface of the metal and the electromagnetic field of the incident radiation results in a phenomenon called surface plasmon resonance (SPR) [77]. It has a typical response time of the order of a picosecond [32]. In the nanostructured thin film, the generation of SPs is the accumulative effect of the

scattering and absorption of light on the surface [78]. The peak position, bandwidth and the intensity of the SPR spectra depend on the nanoparticles size, shape and the surrounding medium [33, 34]. According to the classical Mie theory, the peak position of the SPR shifts toward red/blue with increase/decrease in the size of the spherical shaped nanoparticles [79]. However, this theory fails to explain the shift of the SPR peak towards red with the decrease in the nanoparticles size below 20 nm [16]. As the size of the nanoparticles decreases below 20 nm, the scattering rate of the free electrons increases resulting in a decrease in the SPR frequency (red-shift) [80]. Aggregation and wide size distribution of nanoparticles are also responsible for red shift in the SPR peak position [81]. For the non-spherical shaped particles, the shift in the SPR peaks; transverse and longitudinal modes, for depend on the aspect ratio of the particles [33]. It has been reported that for prolate geometry, as the aspect ratio increases, the transverse mode (TM) is blue-shifted (higher energy) whereas longitudinal mode (LM) is red-shifted (lower energy). But the shift in TM is quite small as compared to that of the LM and vice-versa for oblate geometry [16, 33]. The bandwidth of SPR plays a significant role in deciding the specific application of the nanostructured metallic thin film. For example; larger bandwidth is favourable for plasmonic solar cells as it enhances the absorption efficiency whereas narrow bandwidth is good for plasmonic sensing application [82, 83]. Broadening in the bandwidth is associated with the damping of coherent motion of free electrons [43]. This damping occurs due to the electron-electron, electron-phonon and electron-defect scattering processes. The defects arise due to grain boundaries, impurities and dislocations [84]. The broadening of SPR band as well as its asymmetric nature are also due to wide size distribution of nanoparticles and irregularity in the shapes within the given film [15]. It increases linearly with the density of nanoparticles and surface roughness of the film [15, 85]. It is also inversely proportional to the size of the nanoparticles, d, because of the dominance of the collisional interaction

of the conduction band electrons with the particle surface which reduces the effective mean free path [16]. The relation between bandwidth of SPR and particle size is giving by following *equation* [84].

$$\Gamma\,(d) = \Gamma_0 + \frac{Av_f}{d} \qquad (1.1)$$

where A is the scattering process, Γ_o is the damping constant and v_f is the velocity of conduction band electrons at the Fermi energy [16]. The excitation of SPR in the metal nanoparticles is of great importance because it induces a strong enhancement of the electric field in the near-field region leading to SERS [86], enhancement in NLO signals [49], fluorescence enhancement [87], superlens [88], plasmonic lens [89], plasmonic circuit [1], plasmonic chip [2], waveguide [90, 91], refractive index measurement [92], biomolecular interaction detection [5], single molecule spectroscopy [93], nanoscale lasing [94], quantum computing [95], plasmon assisted photolithography [96], photocatalysis light harvesting [97], biochemical sensor [25, 28] and possible conversion of solar to chemical energy [98]. The major advantage of plasmonic based devices is that their properties can be easily tuned by changing the size of the nanoparticles and the neighbouring dielectric medium.

1.2 Fabrication of nanostructured metallic thin film

Some of the technique for preparing the nanostructured metal thin films are summarized in *table 1.1* along with their salient feature and some of the shortcomings. Out of these technique, the pulsed laser deposition (PLD) technique is devoid of all the above limitations and can be implemented for the deposition of any kind of thin film with precision. PLD technique is used to fabricate variety of nanostructured ultra-thin film of metals [99-101], semiconductors [102-104], ceramic [105], composite [105] etc. This technique is very useful for the fabrication of the plasmonic thin films [12, 105-108]. The film thickness, size and shape of the nanoparticles, comanding the plasmonic properties,

can be controlled by deposition parameters easily [12, 33].

***Table 1.1**: Some common techniques for preparation of nanostructured metallic thin films*

S.No.	Technique	Advantages	Limitations	Reference
1	Thermal Evaporation	Simple and Common Technique	Poor control on quality of film	[109-111]
2	Molecular Beam Epitaxy (MBE)	Better control on quality of film	Expensive	[112, 113]
3	Sputtering	Large varieties can be fabricated	Stoichiometry of target not preserved	[114]
4	Chemical Vapour Deposition (CVD)	Popular and cheap technique for non-metallic films	Deposition of metallic films requires large substrate temperature (>700 C). Deposited films may have impurities and defects due to volatile decomposition of the molecules of the gases involved	[115-117]
5	Atomic Layer Deposition (ALD)	Very precise for few atoms layer deposition	Slow and expensive. There is risk of contamination from residues from precursors as it is chemical based technique	[118, 119]
6	Pulsed Laser Deposition (PLD)	Any kind of film can be deposited with precision with total control of physical and chemical properties. No chances of contamination.	Better suited for small area film deposition	[99-101]

The advantages of PLD over other fabrication techniques are (a) control over the physical and chemical properties of the thin film by proper choice of deposition parameters; laser wavelength, pulse duration, laser fluence, deposition temperature, background gas pressure, target to substrate distance, etc. (b) single-step process, free from any contamination as it does not require any additional chemicals in the entire process, (c)

stoichiometric growth of thin films, (d) growth of multicomponent and multilayer thin films [105, 108, 120-126] and (f) fabrication of thin films is possible even at room temperature (RT) because of the high kinetic energy of plasma species, evolving from laser induced plasma, getting deposited onto the substrate, compared to that of other techniques [105]. The one of the obvious limitation of the PLD technique for the deposition of large area film can be now overcome by rastering of the substrate or scanning the laser beam over the target or both [99, 127]. In the present thesis PLD technique is adopted for the deposition of nanostructured semi-transparent thin films of Cu and is detailed in *section 2.1, chapter 2*.

1.3 General characterization tools for metallic nanostructured thin films

The variety of characterization tools have been implemented to investigate the physical properties of the metallic nanostructured plasmonic thin films. The crystalline structure of the metallic thin films is studied via X-Ray Diffraction (XRD). SPR properties of the nanostructured metallic thin films can be directly investigated via UV-Vis-NIR spectrometer. Atomic Force Microscopy (AFM) is employed to determine the particle size distribution and to investigate the growth dynamic of the thin film. Field-Effect Scanning Electron Microscopy (FESEM) images can used to investigate the surface morphology of thin films. The atomic composition of the thin films can be determined using the Electron Diffraction X-Ray (EDX) spectroscopic technique. Spectroscopic Ellipsometry (SE) can be applied to determine refractive index, extinction coefficient, thickness, absorption coefficient, stoichiometry, interfacial layer thickness and its composition (percentage of oxide formation in case of the metallic thin film, a major source of contamination). Laser micro Raman spectrometer can be used to investigate the surface-enhanced Raman scattering (SERS) effect. Some of these tools used in the present thesis for the characterization of the PLD Cu thin films are detailed in *section 2.2, chapter 2*.

1.4 Optical nonlinearity in nanostructured metallic thin film

Metal nanoparticles embedded in dielectric medium exhibits large third order nonlinearity [12, 49, 128] which leads to the applications in all-optical switching devices, electronic and optical devices, mode locking in laser, optical limiting, optical data storage, chemical and biological sensors etc. [1, 53, 128-134]. The nonlinear optical properties of nanostructure metallic thin films depend on the average nanoparticle size, surface roughness and surrounding environment [36, 55, 135]. The optical nonlinearity present in the metallic nanostructured thin films could be due to three types of mechanisms; (1) intraband transition, (2) interband transition and (3) hot electron formation [55, 62].

There are several reports on NLO behaviour in the nanoparticles of noble metals (Ag, Au and Cu) and metal alloys embedded into various dielectric matrix. The Ag nanoparticles embedded in SiO_2 matrix showed the saturation absorption behaviour at wavelengths of 532 nm and 1064 nm, and exhibited negative value of nonlinear refractive index coefficient (n_2) [136]. The Au nanoparticles embedded in the three different dielectric; Al_2O_3, SiO_2 and ZnO respectively display SA behaviour. Nanoparticles in Al_2O_3 and SiO_2 matrix exhibit positive nonlinear refractive index (NLR) coefficient, whereas that of negative NLR in ZnO [137]. The Cu nanoparticles deposited on the glass substrate below the softening temperature exhibits saturation absorption (SA) behaviour whereas that of deposited above the softening temperature it shows reserve saturation absorption (RSA) [49]. The Cu film deposited above glass softening temperature behaves like optical limiters [49]. The linear and nonlinear optical properties of the nanostructured Cu thin film display distinct behaviour in the different dielectric matrix [128]. The noble metal alloy formed by the binary mixture of Ag and Au in different proportion, exhibits the saturation absorption while it changes the behaviour at higher laser intensity and possess negative nonlinear absorption (NLA) coefficient [138].

A variety of techniques have been developed to measure the NLO properties of materials. These techniques include nonlinear interferometry, degenerate four-wave mixing, ellipse rotation, *Z*-scan technique, beam distortion measurements etc. [139-143]. The first three techniques are sensitive but require relatively complex experimental setup whereas the beam distortion measurement is relatively less sensitive and requires detailed wave propagation analysis. *Z*-scan technique has comparatively simple experimental setup [144]. This technique proposed by Sheik-Bahae et al. in 1989, is a single beam scan method and based on the spatial beam distortion during beam propagation through the nonlinear medium [142]. It is based on the spatial broadening and narrowing of the Gaussian beam in far field because of optical nonlinearity present in the sample. The translation of the sample around the focus of the laser beam leads to a change in irradiance in the sample, resulting in change in the intensity-dependent optical properties. The intensity transmitted through the sample is recorded as a function of sample location (z) with respect to the focal plane. The plot of transmitted intensity as a function of z gives the information about the order of the nonlinearity as well as its sign and magnitude. The technique includes open aperture (OA) and closed aperture (CA) Z-scan measurements which determine nonlinear absorption (NLA) coefficient and nonlinear refractive index (NLR) coefficient, respectively. In the present thesis, the modified Z-scan set-up employed for the measurement of NLO properties of the thin film and is described in *section 2.2.5, chapter 2*.

The variation of SPR and NLO properties of the PLD Cu thin film as a function of surface growth parameters and volume fraction of the constituent species of the metal are not commonly reported in the literature. The properties of thin film are strongly influenced by the surface growth parameters, constituent species and its volume fraction which in turn can be controlled by annealing of the film along with the deposition parameter [145-152].

In the present thesis, it was explored that the annealing can change the constituent species as well as the Fermi energy level of the metal nanoparticle apart from the change in surface morphology, size and shape of the nanoparticles. It was also found that the film deposited near the softening temperature of the substrate, form an interfacial layer which also affected the SPR and NLO properties.

1.5 Organization of Present Thesis:

The present thesis work was aimed towards the fabrication and characterization of semi-transparent nanostructured Cu thin films via PLD technique. The SPR properties of the deposited Cu thin film depend on the average particle size, shape, surface morphology and volume fraction of the constituent species. These parameters can be tuned by varying the substrate temperature and deposition time. The Cu thin film deposited at RT did not show any plasmonic signal in visible region. So, the room temperature (RT**)** deposited films were annealed resulting into a change in the surface morphology, composition and size of nanoparticles which in turn enhanced the plasmonic properties in the visible region. The effect of the interfacial layer, thickness of the film and volume fraction of constituent species on the plasmonic properties of nanostructured Cu thin film have been investigated via SE. Roughness and other surface growth parameters play an important role in linear, SPR and nonlinear properties, and have been investigated via AFM using height-height correlation function (HHCF) and power spectral density function (PSDF) analysis. The effect of size of deposited Cu nanoparticle and film annealing temperature on the third order NLO properties under continuous wave (cw) laser irradiation has been investigated. The SERS properties of nanostructured Cu thin film via PLD is tested on metallic single-wall carbon nanotubes (M-SWCNT).

The overall organization of the thesis is listed below:

Chapter 1, "*Introduction*", presents the overview of the literature survey on the subject. Various characterization tools for analyzing structural, compositional and the linear as well as nonlinear optical properties of these thin films are also touched upon briefly.

Chapter 2, "*Experimental Details*", describes the PLD setup used for fabrication of semi-transparent nanostructured Cu thin films. The various commercial instruments used for the characterization of PLD films are documented in this chapter. The modified *Z*-scan setup developed in house to measure the NLO coefficients is also discussed.

Chapter 3, "*Effect of deposition time and annealing temperature on growth parameters and optical and SPR properties of PLD semi-transparent nanostructured Cu thin films deposited at RT*", includes the effect of deposition time and annealing temperature on the volume fraction of constituent species, fractal analysis, roughness and SPR properties and their correlation.

Chapter 4, "*Effect of deposition time on interfacial layer, optical and SPR properties and scaling behaviour of PLD semi-transparent nanostructured Cu thin films deposited at 400°C*", discusses the variation of SPs properties, thickness and composition of interfacial layer and surface growth parameters of Cu thin films with the deposition time.

Chapter 5, "*Third order nonlinear optical properties of the PLD semi-transparent nanostructured Cu thin films*", discusses the measurement of the non-linear absorption and nonlinear refractive index coefficient of Cu thin films and their dependence on the size of the nanoparticle.

Chapter 6, "*PLD Cu thin films as a viable SERS substrate for carbon nanotubes*", demonstrates the application of PLD Cu thin film as a viable SERS substrate for M-SWCNT.

The last chapter of the thesis, *Chapter 7*, is the *concluding* chapter, summaries the salient features of the present research work along with the possibilities of future expansion.

Bibliography

[1] E. Ozbay, Plasmonics: merging photonics and electronics at nanoscale dimensions, science, 311 (2006) 189-193.

[2] R. Zia, J.A. Schuller, A. Chandran, M.L. Brongersma, Plasmonics: the next chip-scale technology, Materials today, 9 (2006) 20-27.

[3] A.B. Kaul, Microelectronics to Nanoelectronics: Materials, Devices & Manufacturability, CRC Press, 2017.

[4] S.H. Wee, P.-S. Huang, J.-K. Lee, A. Goyal, Heteroepitaxial Cu 2 O thin film solar cell on metallic substrates, Scientific reports, 5 (2015) 16272.

[5] R.W. Nelson, J.R. Krone, O. Jansson, Surface Plasmon Resonance Biomolecular Interaction Analysis Mass Spectrometry. 1. Chip-Based Analysis, Analytical Chemistry, 69 (1997) 4363-4368.

[6] J. Jana, M. Ganguly, T. Pal, Enlightening surface plasmon resonance effect of metal nanoparticles for practical spectroscopic application, RSC Advances, 6 (2016) 86174-86211.

[7] A. Parretta, M.K. Jayaraj, A. Di Nocera, S. Loreti, L. Quercia, A. Agati, Electrical and optical properties of copper oxide films prepared by reactive RF magnetron sputtering, physica status solidi (a), 155 (1996) 399-404.

[8] S.-h. Guo, A.B. Sushkov, D.H. Park, H.D. Drew, P.W. Kolb, W.N. Herman, R.J. Phaneuf, Impact of interface roughness on the performance of broadband blackbody absorber based on dielectric-metal film multilayers, Optics express, 22 (2014) 1952-1962.

[9] H. Song, K. Xia, J. Xiao, Surface roughness modulated resistivity in copper thin films, SCIENCE CHINA Physics, Mechanics & Astronomy, 61 (2018) 107011.

[10] Y.-G. Bi, J. Feng, J.-H. Ji, F.-S. Yi, Y.-F. Li, Y.-F. Liu, X.-L. Zhang, H.-B. Sun, Nanostructures induced light harvesting enhancement in organic photovoltaics, Nanophotonics, 7 (2018) 371-391.

[11] J.P. Huang, L. Gao, Z.Y. Li, Temperature effect on nonlinear optical response of metal–dielectric composite with interfacial layers, Solid state communications, 115 (2000) 347-352.

[12] R. Kesarwani, A. Khare, Surface plasmon resonance and nonlinear optical behavior of pulsed laser-deposited semitransparent nanostructured copper thin films, Applied Physics B, 124 (2018) 116.

[13] S. Law, V. Podolskiy, D. Wasserman, Towards nano-scale photonics with micro-scale photons: the opportunities and challenges of mid-infrared plasmonics, Nanophotonics, 2 (2013) 103-130.

[14] J. Zhang, L. Zhang, W. Xu, Surface plasmon polaritons: physics and applications, Journal of Physics D: Applied Physics, 45 (2012) 113001.

[15] V.N. Rai, A.K. Srivastava, C. Mukherjee, S.K. Deb, Surface enhanced absorption and transmission from dye coated gold nanoparticles in thin films, Applied optics, 51 (2012) 2606-2615.

[16] S. Link, M.A. El-Sayed, Shape and size dependence of radiative, non-radiative and photothermal properties of gold nanocrystals, International reviews in physical chemistry, 19 (2000) 409-453.

[17] H. Raether, Surface plasmons on smooth and rough surfaces and on gratings, Springer-Verlag, 1988.

[18] R. Kesarwani, H. Chaturvedi, A. Khare, Plasmonic interaction between copper nanoparticles and metallic single walled carbon nanotubes, in: International Conference on Fibre Optics and Photonics, Optical Society of America, 2016, pp. P1A. 18.

[19] K.R. Catchpole, A. Polman, Design principles for particle plasmon enhanced solar cells, Applied Physics Letters, 93 (2008) 191113.

[20] N. Deka, M. Islam, P.K. Sarswat, G. Kumar, Enhancing solar cell efficiency with plasmonic behavior of double metal nanoparticle system, Vacuum, 152 (2018) 285-290.

[21] S.A. Maier, H.A. Atwater, Plasmonics: Localization and guiding of electromagnetic energy in metal/dielectric structures, Journal of applied physics, 98 (2005) 10.

[22] J.A. Dionne, L.A. Sweatlock, M.T. Sheldon, A.P. Alivisatos, H.A. Atwater, Silicon-based plasmonics for on-chip photonics, IEEE Journal of Selected Topics in Quantum Electronics, 16 (2010) 295-306.

[23] D.Y. Fedyanin, D.I. Yakubovsky, R.V. Kirtaev, V.S. Volkov, Ultralow-loss CMOS copper plasmonic waveguides, Nano letters, 16 (2015) 362-366.

[24] Y. Liu, Q. Liu, S. Chen, F. Cheng, H. Wang, W. Peng, Surface plasmon resonance biosensor based on smart phone platforms, Scientific reports, 5 (2015) 12864.

[25] J.-F. Masson, Surface Plasmon Resonance Clinical Biosensors for Medical Diagnostics, ACS Sensors, 2 (2017) 16-30.

[26] R.K. Vinnakota, D.A. Genov, Terahertz Optoelectronics with Surface Plasmon Polariton Diode, Scientific Reports, 4 (2014) 4899.

[27] M. Heo, H. Cho, J.W. Jung, J.R. Jeong, S. Park, J.Y. Kim, High-Performance Organic Optoelectronic Devices Enhanced by Surface Plasmon Resonance, Advanced Materials, 23 (2011) 5689-5693.

[28] M. Holzinger, A. Le Goff, S. Cosnier, Nanomaterials for biosensing applications: a review, Frontiers in Chemistry, 2 (2014) 63.

[29] G. Doria, J. Conde, B. Veigas, L. Giestas, C. Almeida, M. Assunção, J. Rosa, P.V. Baptista, Noble Metal Nanoparticles for Biosensing Applications, Sensors, 12 (2012) 1657.

[30] W. Deng, E.M. Goldys, Chemical sensing with nanoparticles as optical reporters: from noble metal nanoparticles to quantum dots and upconverting nanoparticles, Analyst, 139 (2014) 5321-5334.

[31] X. Liu, G. Shan, J. Yu, W. Yang, Z. Ren, X. Wang, X. Xie, H.-j. Chen, X. Chen, Laser heating of metallic nanoparticles for photothermal ablation applications, AIP Advances, 7 (2017) 025308.

[32] Y. Zhu, X. Hu, Y. Fu, H. Yang, Q. Gong, Ultralow-power and ultrafast all-optical tunable plasmon-induced transparency in metamaterials at optical communication range, Scientific reports, 3 (2013) 2338.

[33] C. Noguez, Surface plasmons on metal nanoparticles: the influence of shape and physical environment, The Journal of Physical Chemistry C, 111 (2007) 3806-3819.

[34] M.M. Miller, A.A. Lazarides, Sensitivity of metal nanoparticle surface plasmon resonance to the dielectric environment, The Journal of Physical Chemistry B, 109 (2005) 21556-21565.

[35] M. Nasehnejad, G. Nabiyouni, M.G. Shahraki, Dynamic scaling study of nanostructured silver films, Journal of Physics D: Applied Physics, 50 (2017) 375301.

[36] E.Y. Poliakov, V.A. Markel, V.M. Shalaev, R. Botet, Nonlinear optical phenomena on rough surfaces of metal thin films, Physical Review B, 57 (1998) 14901-14913.

[37] P.R. West, S. Ishii, G.V. Naik, N.K. Emani, V.M. Shalaev, A. Boltasseva, Searching for better plasmonic materials, Laser & Photonics Reviews, 4 (2010) 795-808.

[38] M. Hu, J. Chen, Z.-Y. Li, L. Au, G.V. Hartland, X. Li, M. Marquez, Y. Xia, Gold nanostructures: engineering their plasmonic properties for biomedical applications, Chemical Society Reviews, 35 (2006) 1084-1094.

[39] P.K. Jain, K.S. Lee, I.H. El-Sayed, M.A. El-Sayed, Calculated absorption and scattering properties of gold nanoparticles of different size, shape, and composition: applications in biological imaging and biomedicine, The journal of physical chemistry B, 110 (2006) 7238-7248.

[40] S. Mubeen, S. Zhang, N. Kim, S. Lee, S. Krämer, H. Xu, M. Moskovits, Plasmonic Properties of Gold Nanoparticles Separated from a Gold Mirror by an Ultrathin Oxide, Nano Letters, 12 (2012) 2088-2094.

[41] K.-S. Lee, M.A. El-Sayed, Gold and Silver Nanoparticles in Sensing and Imaging: Sensitivity of Plasmon Response to Size, Shape, and Metal Composition, The Journal of Physical Chemistry B, 110 (2006) 19220-19225.

[42] J. Zhao, A.O. Pinchuk, J.M. McMahon, S. Li, L.K. Ausman, A.L. Atkinson, G.C. Schatz, Methods for Describing the Electromagnetic Properties of Silver and Gold Nanoparticles, Accounts of Chemical Research, 41 (2008) 1710-1720.

[43] O.A. Yeshchenko, I.M. Dmitruk, A.A. Alexeenko, A.M. Dmytruk, Size-dependent melting of spherical copper nanoparticles embedded in a silica matrix, Physical Review B, 75 (2007) 085434.

[44] I. Tanahashi, Y. Manabe, T. Tohda, S. Sasaki, A. Nakamura, Optical nonlinearities of Au/SiO2 composite thin films prepared by a sputtering method, Journal of applied physics, 79 (1996) 1244-1249.

[45] N. Del Fatti, F. Vallée, Ultrafast optical nonlinear properties of metal nanoparticles, Applied Physics B, 73 (2001) 383-390.

[46] A.L. Stepanov, Chapter 7 - Nonlinear Optical Properties of Metal Nanoparticles in Silicate Glass, in: B. Karmakar, K. Rademann, A.L. Stepanov (Eds.) Glass Nanocomposites, William Andrew Publishing, Boston, 2016, pp. 165-179.

[47] A.M. Whelan, M.E. Brennan, W.J. Blau, J.M. Kellya, Enhanced Third-Order Optical Nonlinearity of Silver Nanoparticles with a Tunable Surface Plasmon Resonance, Journal of Nanoscience and Nanotechnology, 4 (2004) 66-68.

[48] N. Faraji, W.M.M. Yunus, A. Kharazmi, E. Saion, Third-order nonlinear optical properties of silver nanoparticles mediated by chitosan, Optik - International Journal for Light and Electron Optics, 125 (2014) 2809-2812.

[49] B. Karthikeyan, M. Anija, C.S.S. Sandeep, T.M.M. Nadeer, R. Philip, Optical and nonlinear optical properties of copper nanocomposite glasses annealed near the glass softening temperature, Optics Communications, 281 (2008) 2933-2937.

[50] T. Tokizaki, A. Nakamura, S. Kaneko, K. Uchida, S. Omi, H. Tanji, Y. Asahara, Subpicosecond time response of third-order optical nonlinearity of small copper particles in glass, Applied physics letters, 65 (1994) 941-943.

[51] M.A. Gatoo, S. Naseem, M.Y. Arfat, A. Mahmood Dar, K. Qasim, S. Zubair, Physicochemical properties of nanomaterials: implication in associated toxic manifestations, BioMed research international, 2014 (2014).

[52] A. Mooradian, Photoluminescence of metals, Physical Review Letters, 22 (1969) 185.

[53] M. Kauranen, A.V. Zayats, Nonlinear plasmonics, Nature Photonics, 6 (2012) 737.

[54] S. Dhara, C.-Y. Lu, P. Magudapathy, Y.-F. Huang, W.-S. Tu, K.-H. Chen, Surface plasmon polariton assisted optical switching in noble bimetallic nanoparticle system, Applied Physics Letters, 106 (2015) 023101.

[55] F. Hache, D. Ricard, C. Flytzanis, U. Kreibig, The optical Kerr effect in small metal particles and metal colloids: the case of gold, Applied Physics A, 47 (1988) 347-357.

[56] L. Lu, Y. Shen, X. Chen, L. Qian, K. Lu, Ultrahigh Strength and High Electrical Conductivity in Copper, Science, 304 (2004) 422-426.

[57] C.K. Hu, L. Gignac, R. Rosenberg, Electromigration of Cu/low dielectric constant interconnects, Microelectronics Reliability, 46 (2006) 213-231.

[58] P.E. Hopkins, J.C. Duda, R.N. Salaway, J.L. Smoyer, P.M. Norris, Effects of intra- and interband transitions on electron-phonon coupling and electron heat capacity after short-pulsed laser heating, Nanoscale and Microscale Thermophysical Engineering, 12 (2008) 320-333.

[59] K.C. Mishra, A. Piquette, P.C. Schmidt, K.H. Johnson, Electronic structures and optical properties of Al, Cu, and Ag in zero, two, and three dimensional structures, Journal of Applied Physics, 122 (2017) 063104.

[60] B. Segall, Fermi surface and energy bands of copper, Physical Review, 125 (1962) 109.

[61] J.P. Marton, B.D. Jordan, Optical properties of aggregated metal systems: Interband transitions, Physical Review B, 15 (1977) 1719-1727.

[62] U. Kreibig, M. Vollmer, Optical properties of metal clusters, Springer, 1995.

[63] A. Pinchuk, G. Von Plessen, U. Kreibig, Influence of interband electronic transitions on the optical absorption in metallic nanoparticles, Journal of Physics D: Applied Physics, 37 (2004) 3133.

[64] H. Wang, F. Tam, N.K. Grady, N.J. Halas, Cu nanoshells: effects of interband transitions on the nanoparticle plasmon resonance, The Journal of Physical Chemistry B, 109 (2005) 18218-18222.

[65] S.K. Ghosh, D.S. Rahman, A.L. Ali, A. Kalita, Surface plasmon tunability and emission sensitivity of ultrasmall fluorescent copper nanoclusters, Plasmonics, 8 (2013) 1457-1468.

[66] Y. Gao, D. Kong, Nonlinear Optical Response of Noble Metal Nanoparticles, in: Laser Technology and its Applications, IntechOpen, 2018.

[67] J.Z. Anvari, R. Karimzadeh, N. Mansour, Thermo-optic properties and nonlinear responses of copper nanoparticles in polysiloxane oil, Journal of Optics, 12 (2010) 035212.

[68] M.B. Gawande, A. Goswami, F.-X. Felpin, T. Asefa, X. Huang, R. Silva, X. Zou, R. Zboril, R.S. Varma, Cu and Cu-Based Nanoparticles: Synthesis and Applications in Catalysis, Chemical Reviews, 116 (2016) 3722-3811.

[69] A.M. Ealias, M.P. Saravanakumar, A review on the classification, characterisation, synthesis of nanoparticles and their application, IOP Conference Series: Materials Science and Engineering, 263 (2017) 032019.

[70] J. Niittynen, E. Sowade, H. Kang, R.R. Baumann, M. Mäntysalo, Comparison of laser and intense pulsed light sintering (IPL) for inkjet-printed copper nanoparticle layers, Scientific reports, 5 (2015) 8832.

[71] A.A. Rakhmetova, T.P. Alekseeva, O.A. Bogoslovskaya, I.O. Leipunskii, I.P. Ol'khovskaya, A.N. Zhigach, N.N. Glushchenko, Wound-healing properties of copper nanoparticles as a function of physicochemical parameters, Nanotechnologies in Russia, 5 (2010) 271-276.

[72] J. Bhattacharya, U. Choudhuri, O. Siwach, P. Sen, A.K. Dasgupta, Interaction of hemoglobin and copper nanoparticles: implications in hemoglobinopathy, Nanomedicine: Nanotechnology, Biology and Medicine, 2 (2006) 191-199.

[73] R.K. Sahu, S.H. Somashekhar, P.V. Manivannan, Investigation on Copper Nanofluid Obtained through Micro Electrical Discharge Machining for Dispersion Stability and Thermal Conductivity, Procedia Engineering, 64 (2013) 946-955.

[74] S. Dhara, Surface Plasmon Polariton Assisted Optical Switching in Noble Metal Nanoparticle Systems: A Sub-Band Gap Approach, in: Reviews in Plasmonics 2015, Springer, 2016, pp. 1-17.

[75] T. Gupta, Dielectric Materials, in: Copper Interconnect Technology, Springer Science & Business Media, 2010, pp. 67-110.

[76] E. Kretschmann, Decay of non radiative surface plasmons into light on rough silver films. Comparison of experimental and theoretical results, Optics Communications, 6 (1972) 185-187.

[77] S.A. Maier, Plasmonics: fundamentals and applications, Springer Science & Business Media, 2007.

[78] J. Olson, S. Dominguez-Medina, A. Hoggard, L.-Y. Wang, W.-S. Chang, S. Link, Optical characterization of single plasmonic nanoparticles, Chemical Society Reviews, 44 (2015) 40-57.

[79] W. Hergert, T. Wriedt, Mie Theory: A Review, in: The Mie Theory: basics and applications, Springer Series in Optical Science 2012.

[80] O.A. Yeshchenko, I.M. Dmitruk, A.A. Alexeenko, A.V. Kotko, J. Verdal, A.O. Pinchuk, Size and temperature effects on the surface plasmon resonance in silver nanoparticles, Plasmonics, 7 (2012) 685-694.

[81] V.V. Truong, G.D. Scott, Optical properties of aggregated noble metal films, Journal of optical society of America, 67 (1977) 502-510.

[82] K.M. Byun, S.J. Yoon, D. Kim, Effect of surface roughness on the extinction-based localized surface plasmon resonance biosensors, Applied optics, 47 (2008) 5886-5892.

[83] W. Ren, G. Zhang, Y. Wu, H. Ding, Q. Shen, K. Zhang, J. Li, N. Pan, X. Wang, Broadband absorption enhancement achieved by optical layer mediated plasmonic solar cell, Optics express, 19 (2011) 26536-26550.

[84] S. Link, M.A. El-Sayed, Size and temperature dependence of the plasmon absorption of colloidal gold nanoparticles, The Journal of Physical Chemistry B, 103 (1999) 4212-4217.

[85] N. Fang, Z. Liu, T.-J. Yen, X. Zhang, Experimental study of transmission enhancement of evanescent waves through silver films assisted by surface plasmon excitation, Applied Physics A, 80 (2005) 1315-1325.

[86] B. Sharma, R.R. Frontiera, A.-I. Henry, E. Ringe, R.P. Van Duyne, SERS: Materials, applications, and the future, Materials Today, 15 (2012) 16-25.

[87] S. Roy, J.-H. Kim, J.T. Kellis, A.J. Poulose, C.R. Robertson, A.P. Gast, Surface Plasmon Resonance/Surface Plasmon Enhanced Fluorescence: An Optical Technique for the Detection of Multicomponent Macromolecular Adsorption at the Solid/Liquid Interface, Langmuir, 18 (2002) 6319-6323.

[88] J.B. Pendry, Negative refraction makes a perfect lens, Physical review letters, 85 (2000) 3966.

[89] Y. Fu, X. Zhou, Plasmonic Lenses: A Review, Plasmonics, 5 (2010) 287-310.

[90] Z. Chai, X. Hu, Y. Zhu, F. Zhang, H. Yang, Q. Gong, Low-power and ultrafast all-optical tunable plasmon-induced transparency in plasmonic nanostructures, Applied Physics Letters, 102 (2013) 201119.

[91] N. Liu, L. Langguth, T. Weiss, J. Kästel, M. Fleischhauer, T. Pfau, H. Giessen, Plasmonic analogue of electromagnetically induced transparency at the Drude damping limit, Nature materials, 8 (2009) 758.

[92] J.-Y. Lee, H.-C. Shih, C.-T. Hong, T.K. Chou, Measurement of refractive index change by surface plasmon resonance and phase quadrature interferometry, Optics communications, 276 (2007) 283-287.

[93] A.B. Taylor, P. Zijlstra, Single-Molecule Plasmon Sensing: Current Status and Future Prospects, ACS Sensors, 2 (2017) 1103-1122.

[94] R.F. Oulton, Surface plasmon lasers: sources of nanoscopic light, Materials Today, 15 (2012) 26-34.

[95] M.S. Tame, K.R. McEnery, Ş.K. Özdemir, J. Lee, S.A. Maier, M.S. Kim, Quantum plasmonics, Nature Physics, 9 (2013) 329.

[96] D.B. Shao, S.C. Chen, Surface-plasmon-assisted nanoscale photolithography by polarized light, Applied physics letters, 86 (2005) 253107.

[97] X.-C. Ma, Y. Dai, L. Yu, B.-B. Huang, Energy transfer in plasmonic photocatalytic composites, Light: Science & Applications, 5 (2016) e16017.

[98] X. Meng, L. Liu, S. Ouyang, H. Xu, D. Wang, N. Zhao, J. Ye, Nanometals for Solar-to-Chemical Energy Conversion: From Semiconductor-Based Photocatalysis to Plasmon-Mediated Photocatalysis and Photo-Thermocatalysis, Advanced Materials, 28 (2016) 6781-6803.

[99] A.T.T. Mostako, A. Khare, Note: Large area deposition of Rh single and Rh/W/Cu multilayer thin films on stainless steel substrate by pulsed laser deposition technique, Review of Scientific Instruments, 85 (2014) 046101.

[100] A.T.T. Mostako, C.V.S. Rao, A. Khare, Pulsed laser deposition of thin film of molybdenum, in: Journal of Physics: Conference Series, IOP Publishing, 2010, pp. 012114.

[101] A.T.T. Mostako, C.V.S. Rao, A. Khare, Mirrorlike pulsed laser deposited tungsten thin film, Review of Scientific Instruments, 82 (2011) 013101.

[102] P.P. Dey, A. Khare, Effect of substrate temperature on structural and linear and nonlinear optical properties of nanostructured PLD a-SiC thin films, Materials Research Bulletin, 84 (2016) 105-117.

[103] P.P. Dey, A. Khare, Stoichiometry-dependent linear and nonlinear optical properties of PLD SiOx thin films, Journal of Alloys and Compounds, 706 (2017) 370-376.

[104] I. Kumar, A. Khare, Raman spectra of PLD deposited DLC thin films on Si substrate, in: AIP Conference Proceedings, AIP, 2014, pp. 1018-1020.

[105] D.B. Chrisey, G.K. Hubler, Pulsed laser deposition of thin films, John Wiley & Sons, Inc., 1994.

[106] R.P. Sugavaneshwar, S. Ishii, T.D. Dao, A. Ohi, T. Nabatame, T. Nagao, Fabrication of Highly Metallic TiN Films by Pulsed Laser Deposition Method for Plasmonic Applications, ACS Photonics, 5 (2018) 814-819.

[107] R. McCann, C. Hughes, K. Bagga, A. Stalcup, M. Vázquez, D. Brabazon, Pulsed laser deposition of plasmonic nanostructured gold on flexible transparent polymers at atmospheric pressure, Journal of Physics D: Applied Physics, 50 (2017) 245303.

[108] L.M. Kukreja, S. Verma, D.A. Pathrose, B.T. Rao, Pulsed laser deposition of plasmonic-metal nanostructures, Journal of Physics D: Applied Physics, 47 (2013) 034015.

[109] S. Basavaiah, S.R. Pollack, Superconductivity in evaporated tungsten films, Applied Physics Letters, 12 (1968) 259-260.

[110] M.M. Alam, M.N.H. Mia, R. Hasan, M. Shahinuzzaman, M.K. Islam, K.M.N. Uddin, Study of structural and morphological properties of vacuum coated copper (Cu) metal thin film, Materials Sciences and Applications, 6 (2015) 753.

[111] R.C. Jaeger, Film Deposition, Introduction to Microelectronic Fabrication, Upper Saddle Rivers: Prentice Hall, 83 (2002).

[112] E.H. Parker, The technology and physics of molecular beam epitaxy, Plenum Press New York, 1985.

[113] J.L. Vossen, W. Kern, W. Kern, Thin film processes II, Gulf Professional Publishing, 1991.

[114] J. Su, Y. Liu, M. Jiang, X. Zhu, Oxidation of copper during physical sputtering deposition: mechanism, avoidance and utilization, arXiv preprint arXiv:1412.2031, (2014).

[115] R. Becker, A. Devi, J. Weiß, U. Weckenmann, M. Winter, C. Kiener, H.-W. Becker, R.A. Fischer, A Study on the Metal Organic CVD of Pure Copper Films from Low Cost Copper(II) Dialkylamino-2-propoxides: Tuning the Thermal Properties of the Precursor by Small Variations of the Ligand, Chemical Vapor Deposition, 9 (2003) 149-156.

[116] J. Creighton, P. Ho, Introduction to chemical vapor deposition (CVD), Chemical vapor deposition, 2 (2001) 1-22.

[117] T.F. Deutsch, D.D. Rathman, Comparison of laser-initiated and thermal chemical vapor deposition of tungsten films, Applied Physics Letters, 45 (1984) 623-625.

[118] Z. Li, A. Rahtu, R.G. Gordon, Atomic layer deposition of ultrathin copper metal films from a liquid copper (I) amidinate precursor, Journal of The Electrochemical Society, 153 (2006) C787-C794.

[119] M. Leskelä, M. Ritala, Atomic layer deposition chemistry: recent developments and future challenges, Angewandte Chemie International Edition, 42 (2003) 5548-5554.

[120] R.K. Singh, J. Narayan, Pulsed-laser evaporation technique for deposition of thin films: Physics and theoretical model, Physical review B, 41 (1990) 8843.

[121] Y. Oshikane, Fabrication of Plasmonic Crystalline Thin Film of Titanium Nitride (TiN) by Pulsed Laser Deposition with Third Harmonic of Nd: YAG Laser and Its Spectroscopic Analyses, in: Nanoplasmonics-Fundamentals and Applications, InTech, 2017.

[122] H.-U. Krebs, M. Weisheit, J. Faupel, E. Süske, T. Scharf, C. Fuhse, M. Störmer, K. Sturm, M. Seibt, H. Kijewski, D. Nelke, E. Panchenko, M. Buback, Pulsed Laser Deposition (PLD)--A Versatile Thin Film Technique, in: Advances in Solid State Physics, Springer, 2003, pp. 505-518.

[123] H.U. Krebs, O. Bremert, Pulsed laser deposition of thin metallic alloys, Applied physics letters, 62 (1993) 2341-2343.

[124] J. Bohandy, B.F. Kim, F.J. Adrian, Metal deposition from a supported metal film using an excimer laser, Journal of Applied Physics, 60 (1986) 1538-1539.

[125] G.V. Naik, J. Kim, A. Boltasseva, Oxides and nitrides as alternative plasmonic materials in the optical range [Invited], Opt. Mater. Express, 1 (2011) 1090-1099.

[126] J. Shen, Z. Gai, J. Kirschner, Growth and magnetism of metallic thin films and multilayers by pulsed-laser deposition, Surface science reports, 52 (2004) 163-218.

[127] J.A. Greer, M.D. Tabat, Large-area pulsed laser deposition: Techniques and applications, Journal of Vacuum Science & Technology A: Vacuum, Surfaces, and Films, 13 (1995) 1175-1181.

[128] Y.-x. Zhang, Y.-h. Wang, Nonlinear optical properties of metal nanoparticles: a review, RSC Advances, 7 (2017) 45129-45144.

[129] C. Min, P. Wang, C. Chen, Y. Deng, Y. Lu, H. Ming, T. Ning, Y. Zhou, G. Yang, All-optical switching in subwavelength metallic grating structure containing nonlinear optical materials, Optics letters, 33 (2008) 869-871.

[130] X. Hu, P. Jiang, C. Ding, H. Yang, Q. Gong, Picosecond and low-power all-optical switching based on an organic photonic-bandgap microcavity, Nature Photonics, 2 (2008) 185.

[131] Y. Wang, C.-Y. Lin, A. Nikolaenko, V. Raghunathan, E.O. Potma, Four-wave mixing microscopy of nanostructures, Advances in optics and photonics, 3 (2011) 1-52.

[132] T. Jiang, Z. Kang, G. Qin, J. Zhou, W. Qin, Low mode-locking threshold induced by surface plasmon field enhancement of gold nanoparticles, Optics Express, 21 (2013) 27992-28000.

[133] N.C. Panoiu, W.E.I. Sha, D.Y. Lei, G.C. Li, Nonlinear optics in plasmonic nanostructures, Journal of Optics, 20 (2018) 083001.

[134] S. Porel, N. Venkatram, D.N. Rao, T.P. Radhakrishnan, Optical power limiting in the femtosecond regime by silver nanoparticle–embedded polymer film, Journal of Applied Physics, 102 (2007) 033107.

[135] F. Balzer, H.-G. Rubahn, Influence of surface roughness on frequency shift and third-order nonlinear susceptibility of adsorbed particles, in: Laser Techniques for Surface Science II, International Society for Optics and Photonics, 1995, pp. 40-52.

[136] Y.H. Wang, S.J. Peng, J.D. Lu, R.W. Wang, Y.G. Cheng, Y.L. Mao, Nonlinear optical properties of Ag nanocluster composite fabricated by 200 keV negative ion implantation, Vacuum, 83 (2008) 412-415.

[137] A.I. Ryasnyanskiy, B. Palpant, S. Debrus, U. Pal, A. Stepanov, Third-order nonlinear-optical parameters of gold nanoparticles in different matrices, Journal of luminescence, 127 (2007) 181-185.

[138] I. Papagiannouli, P. Aloukos, D. Rioux, M. Meunier, S. Couris, Effect of the Composition on the Nonlinear Optical Response of Au x Ag1–x Nano-Alloys, The Journal of Physical Chemistry C, 119 (2015) 6861-6872.

[139] S.R. Friberg, P.W. Smith, Nonlinear optical glasses for ultrafast optical switches, IEEE Journal of Quantum Electronics, 23 (1987) 2089-2094.

[140] M.J. Moran, S. Chiao-Yao, R.L. Carman, Interferometric measurements of the nonlinear refractive-index coefficient relative to CS_2 laser-system-related materials, IEEE Journal of Quantum Electronics, 11 (1975) 259-263.

[141] A. Owyoung, Ellipse rotation studies in laser host materials, IEEE Journal of Quantum Electronics, 9 (1973) 1064-1069.

[142] M. Sheik-Bahae, A.A. Said, T.-H. Wei, D.J. Hagan, E.W.V. Stryland, Sensitive measurement of optical nonlinearities using a single beam, IEEE Journal of Quantum Electronics, 26 (1990) 760-769.

[143] W.E. Williams, M.J. Soileau, E.W. Van Stryland, Optical switching and n2 measurements in CS2, Optics Communications, 50 (1984) 256-260.

[144] I. Kumar, A. Khare, Modified Z-scan set-up using CCD for measurement of optical nonlinearity in PLD carbon thin film, Optics & Laser Technology, 77 (2016) 51-54.

[145] S. El Whibi, L. Derbali, P. Tristant, C. Jaoul, M. Colas, R. Mayet, J. Cornette, H. Ezzaouia, Optimized nc-Si:H thin films with enhanced optoelectronic properties prepared by micro-waves PECVD used as an effective silicon surface passivation layer, Journal of Materials Science: Materials in Electronics, 30 (2019) 2351-2359.

[146] R. Dreyfus, Cu0, Cu+, and Cu2 from excimer-ablated copper, Journal of applied physics, 69 (1991) 1721-1729.

[147] V. Drobny, L. Pulfrey, Properties of reactively-sputtered copper oxide thin films, Thin solid films, 61 (1979) 89-98.

[148] D. Popov, P. Docheva, Deposition of copper oxide, titanium oxide and indium tin oxide films by reactive magnetron sputtering, Vacuum, 42 (1991) 53-55.

[149] H. Nishikawa, R. Yoshikawa, Controlling the chemical composition of hydroxyapatite thin films using pulsed laser deposition, Transactions of the Materials Research Society of Japan, 40 (2015) 111-114.

[150] A. Radziszewska, S. Kac, M. Feuerbacher, Nanostructured thin films β-Al-Mg obtained using PLD technique, Acta Physica Polonica-Series A General Physics, 117 (2010) 799.

[151] A. Serrano, O. Rodriguez De La Fuente, M. García, Extended and localized surface plasmons in annealed Au films on glass substrates, Journal of Applied Physics, 108 (2010) 074303.

[152] M. Syed, C. Glaser, C. Hynes, M. Syed, Thermal Annealing of Gold Thin Films on the Structure and Surface Morphology Using RF Magnetron Sputtering.

Chapter 2
Experimental Details

There are various techniques documented in literature for the deposition of metallic thin films [1-4]. Among them, the pulsed laser deposition (PLD) technique is quite flexible for fabrication of plasmonic thin films of the noble metals having very high melting point. PLD is a single step process, free from any contamination and it does not required any hazardous gas and hence environment friendly [5-8]. In the present thesis, PLD technique was used to deposit the nanostructured copper (Cu) thin films at room temperature (RT) as well as at 400ºC as a function of deposition time. In order to study the effect of annealing on the plasmonic and other properties of the Cu thin film, RT films were gradually annealed up to a temperature of 400°C. These plasmonic films via PLD were characterized by UV visible-Near Infrared (UV-Vis-NIR) spectroscopy, Atomic force microscopy (AFM), Spectroscopic ellipsometer (SE) and X-ray diffraction (XRD). The nonlinear absorption (NLA) and nonlinear refractive index (NLR) coefficients of the thin films were measured by modified Z-scan setup developed in house. The surface enhanced Raman spectroscopy (SERS) capability of thin films was tested on carbon nanotube.

In this chapter, the experimental details of PLD setup, SE setup, modified Z-scan setup and all the other characterization tools employed for PLD films are presented.

2.1 Pulsed laser deposition (PLD) setup

The schematic and the photograph of the experimental PLD setup used for deposition of the plasmonic Cu nanostructure thin films is shown in *figure 2.1* and *2.2* respectively. It consists of a 18″ diameter ultra-high vacuum compatible multiport stain

steel ablation chamber. The Cu target was mounted on the motorized controlled-carrousel stage and was inserted inside the ablation chamber through one of its 150 CF port. The target was continuously rastered in a programmable manner to maintain the reproducibility on shot-to-shot basis of laser pulses. The substrate was mounded on the substrate holder assembly, having provision for resistive heating to control the substrate temperature in a programmable manner, through another 150 CF port opposite to the target carrousel port.

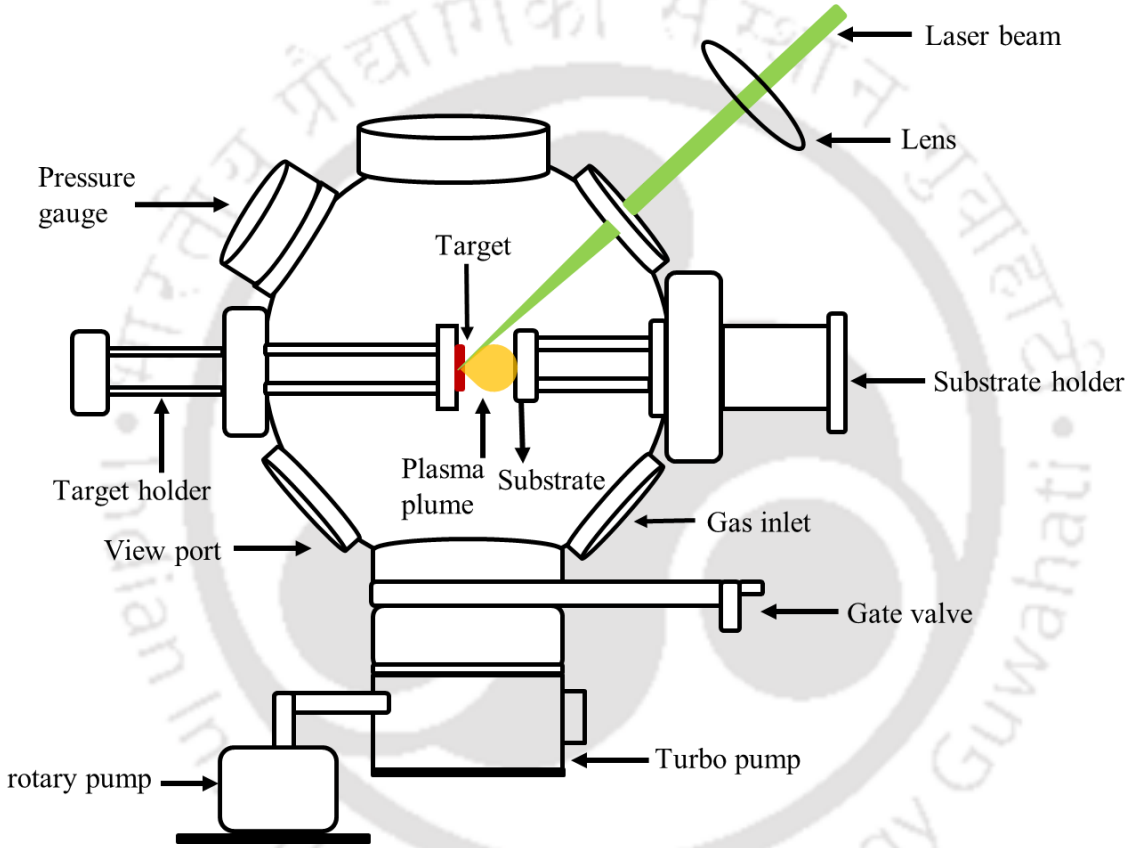

***Figure 2.1**: Schematic of PLD setup.*

Prior to the deposition, chamber was evaluated to a base pressure of ~ 10^{-6} mbar via turbo molecular pump (*Pfeiffer, Hi Pace 700*) connected to the bottom 100 CF port of the ablation chamber, as shown in figure *2.1*. The turbo molecular pump was backed by a rotatory pump (*GE Motors, F 144*). The pressure inside the ablation chamber was monitored using the compact full range gauge (*Pfeiffer, D 35614*). A Q-switched Nd:YAG laser was steered by

a high damage threshold right angled prism (omitted in the figure) and focused using the plano-convex lens (f= 35 cm) on to the Cu target as shown in *figure 2.1*.

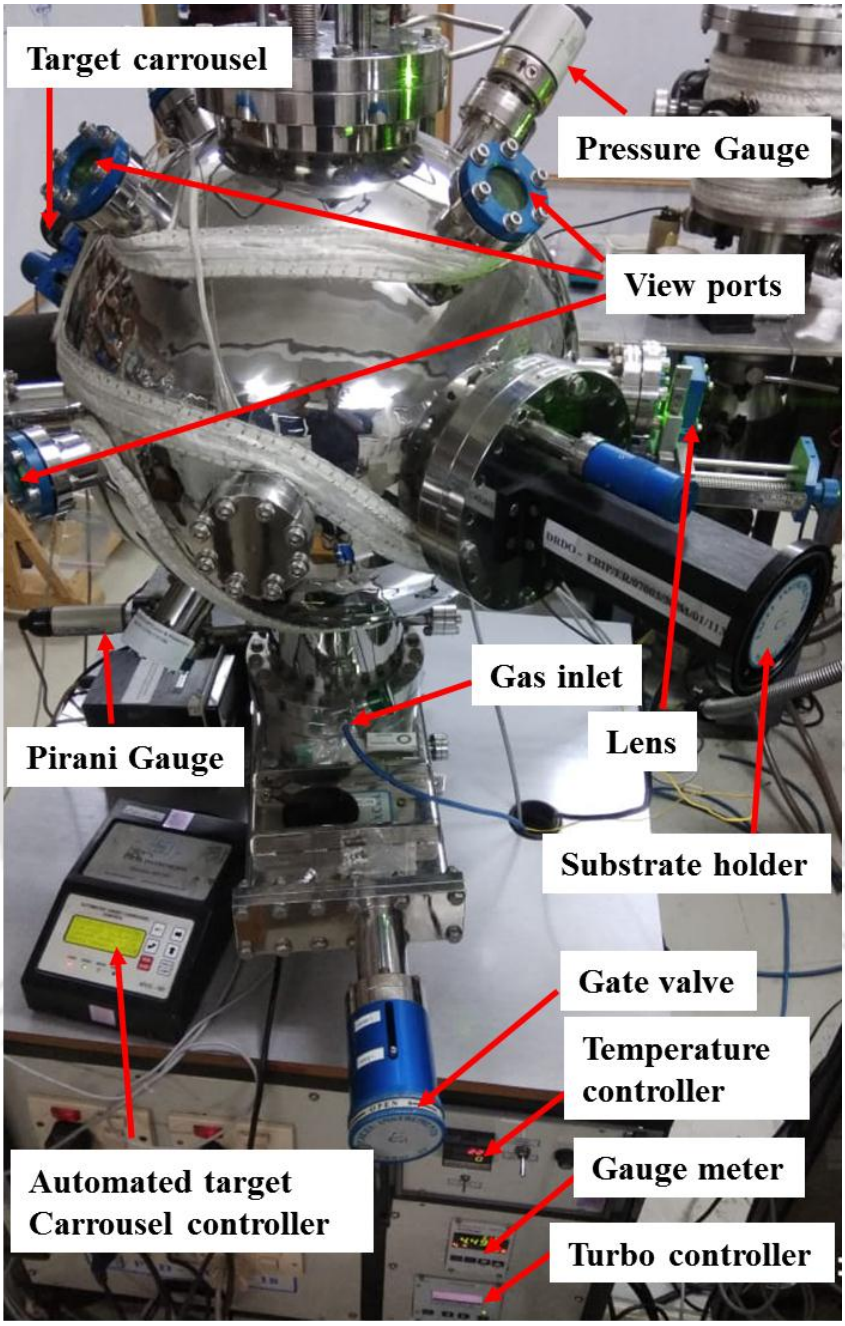

Figure 2.2: *Photograph of PLD setup.*

The laser ablated material from the target was deposited on to the glass (coverslip) substrate placed at a distance in between 5 - 6.5 cm from the target and parallel to it. The RT films were fabricated via PLD under vacuum (~ 10^{-6} mbar) by third harmonic (~ 355 nm) of a Q-

switched neodymium-doped yttrium aluminum garnet (Nd:YAG) laser (Model No.- *Quanta-Ray*, *INDI-HG*) for the deposition time of 4, 6 and 8 minutes at a laser fluence of ~ 3.5 J/cm^2. For each and every deposition time, five films were fabricated. All these fifteen films were divided into five sets, each set containing three films, one each deposited at 4, 6 and 8 minutes as listed in *table 2.1*.

Table 2.1*: Deposition parameters for the fabrication of Cu thin films.*

Sample	Deposition duration (minutes)	Ambient pressure (mbar)	Gradual annealed up temperature	Substrate
Set 1	4, 6 and 8 (deposited at RT via third harmonic Nd:YAG laser)	~ 10^{-6}	As-deposited	Coverslip (glass)
Set 2			100°C	
Set 3			200°C	
Set 4			300°C	
Set 5			400°C	

Set 1 was kept for the characterization of as-deposited films. Set 2 was annealed at 100°C. The sets 3 to 5 were gradually annealed in the temperature range of 200°C to 400°C respectively in a step of 100°C. At each temperature, film was maintained for four hours and then cooled down to RT and after couple of hours the temperature was raised to next higher level (100°C – 200°C, 200°C – 300°C etc.). The temperature was raised in a programmable way at the rate of 5°C per minutes from RT to required temperature (100°C, 200°C, 300°C and 400°C). Thereafter, the temperature was maintained for 4 hours and finally it was cool down at the rate of 1.7°C per minutes till RT. The entire annealing process for each and every film was performed under vacuum (~10^{-6} mbar). In this way the effect of both, the deposition time and annealing temperature (post deposition) were studied.

The best SPR properties were observed for the film finally annealed at a temperature of 400ºC. Therefore another set of films was fabricated at a substrate temperature of 400ºC

directly for the deposition time of 6, 7, 8, 9, 10, 20, 30 and 45 minutes in order to study the affect of longer duration of deposition on the properties of nanostructured Cu PLD films. After the deposition, films were maintained at 400ºC under vacuum for 120 minutes in order to remove the any strain developed during deposition. This set of films was fabricated by second harmonic of Nd:YAG (Model No.- *Quanta System, HYL-101*) laser at 532 nm and rest of the deposition conditions were maintained same as that of the films deposited at RT.

2.2 Characterization of PLD thin films

All the samples fabricated via PLD in the present thesis were subjected to several characterizations as briefed below:

2.2.1 Atomic force microscopy (AFM)

To relate the dependence of optical properties of the films with their surface morphology, size and shape of the nanoparticles and surface growth parameters (micro-roughness, fractal analysis, correlation length, activation energy etc.) all the films were subjected to atomic force microscopy (AFM) (Model No. - *Agilent, 550 series*). The AFM was used in non-contact mode using silicon cantilever to image the surface morphology. The growth dynamics and other growth parameters from the AFM images were assessed via open source Gwyddion software and WXSM software [9, 10].

2.2.2 X-Ray Diffraction (XRD)

X-ray diffraction technique was employed to investigate the crystal structure of the PLD thin films. The XRD pattern was recorded in the thin film mode by commercial *Rigaku TTRX III X-ray diffractometer* employing Cu K_α (1.5418 Å) radiation at a grazing angle of incidence of $\omega = 1°$.

2.2.3 UV visible-Near Infrared (UV-Vis-NIR) spectroscopy

To study the SPR properties of all the PLD semitransparent films of Cu, absorption spectra of these films deposited on glass substrate were recorded using a dual beam UV visible-Near Infrared spectrometer (Model no.- *Shimadzu- UV 3101 PC*). From these spectra the plasmonic (surface plasmon resonance (SPR)) peaks were identified. The peak position and bandwidth of the SPR and peak due to the interband transitions are identified via multiple fitting of the absorption spectra of these PLD films with skew-symmetric bi-Gaussian and Gaussian analytical equation respectively.

2.2.4 Spectroscopy Ellipsometry (SE)

The optical properties, interfacial layer thickness and its composition of all the PLD film Cu thin films were examined by variable angle spectroscopy ellipsometer equipped with goniometer (Model no.: *Semilab GES5-E*). *Figure 2.3 and 2.4* show the schematic of working principle of a spectroscopic ellipsometer and the photograph of the model employed respectively. In this, a linearly polarized light beam falls on a sample under investigation and the amplitude ratio ($tan\psi$) and phase shift (Δ) between parallel (p) and perpendicular (s) components of the light reflected from the surface are recorded as a function of wavelength and the angle of incidence, where ψ and Δ are the ellipsometer angles related to the complex reflectance ratio of the two polarization components of light given by *equation 2.1* below [11].

$$\rho = \frac{r_p}{r_s} = tan(\psi)\, e^{(i\Delta)} \qquad (2.1)$$

where r_p and r_s are the Fresnel reflection coefficients of p and s polarized light respectively.

The pseudo dielectric constants of the sample are calculated using the simple ambient substrate optical model and expressed as [11, 12]

$$\varepsilon = \varepsilon_1 + i\varepsilon_2 = sin^2(\varphi)\left[1 + \left(\frac{1-\rho}{1+\rho}\right)^2 tan^2(\phi)\right] \quad (2.2)$$

$$\varepsilon_1 = \varepsilon_\infty + \sum_i \varepsilon_{1,i} \;\&\; \varepsilon_2 = \sum_i \varepsilon_{2,i} \quad (2.3)$$

where $\varepsilon_{1,i}$ & $\varepsilon_{2,i}$ are real and imaginary part of dielectric function of i^{th} oscillator, ϕ is the angle of incidence and the quantity ε_∞ (usually $1 \leq \varepsilon_\infty \leq 10$) is the contribution from the residual polarization due to the positive charged background of the ionic cores [13]. The real and imaginary parts of the dielectric constant (pseudo) are obtained using *equation* (*2.2*) & (*2.3*) and consequently the refractive index (*n*) and extinction coefficient (k') are calculated by using the following relations [11].

$$n = \left[\left(\varepsilon_1 + (\varepsilon_1^2 + \varepsilon_2^2)^{1/2}\right)/2\right]^{1/2} \quad (2.4)$$

$$k' = \left[\left(-\varepsilon_1 + (\varepsilon_1^2 + \varepsilon_2^2)^{1/2}\right)/2\right]^{1/2} \quad (2.5)$$

The SE measurement for the PLD Cu thin films were carried out over the spectral range from 1 to 4 eV (in the wavelength range of 300 to 1200 nm) for incident angle, ϕ, ranging from 50° to 77°. The analysis of the SE data was performed via spectroscopy ellipsometry analyzer (SEA) software. In SEA, accuracy of the result depends on the Root Mean Square Error (RMSE) which should be least for the best fitting. The Levenberg-Marquardt regression algorithm was used for minimizing the value of RMSE [11], defined as

$$RMSE = \sqrt{\frac{1}{2N-m}\sum_{i=1}^{N}\left[\left(\frac{f_{1,meas}^i - f_{1,calc}^i}{\sigma_{1,meas}^i}\right)^2 w_1 + \left(\frac{f_{2,meas}^i - f_{2,calc}^i}{\sigma_{2,meas}^i}\right)^2 w_2\right]} \quad (2.6)$$

where *N* is the number of measured data points, *m* is the number of fitted model parameters, f_{meas}^i and f_{calc}^i are the i^{th} measured and calculated ellipsometric quantities, 1 for $tan\psi$ and 2 for cosΔ, σ_{meas}^i and σ_{calc}^i are the point-wise experimental errors belonging to the i^{th} f [1]

and f^2 measurements respectively, w_1 and w_2 are user defined weight factors.

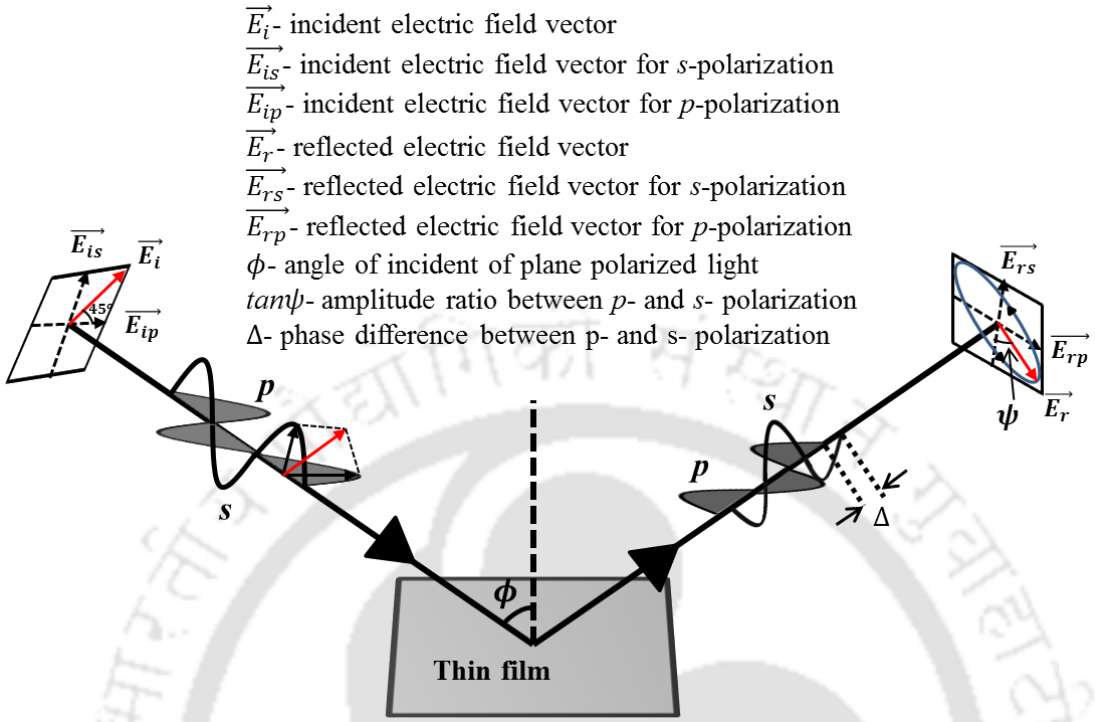

Figure 2.3: *Reflection of polarized light on film surface and geometrical interpretation of SE parameters (ψ, Δ).*

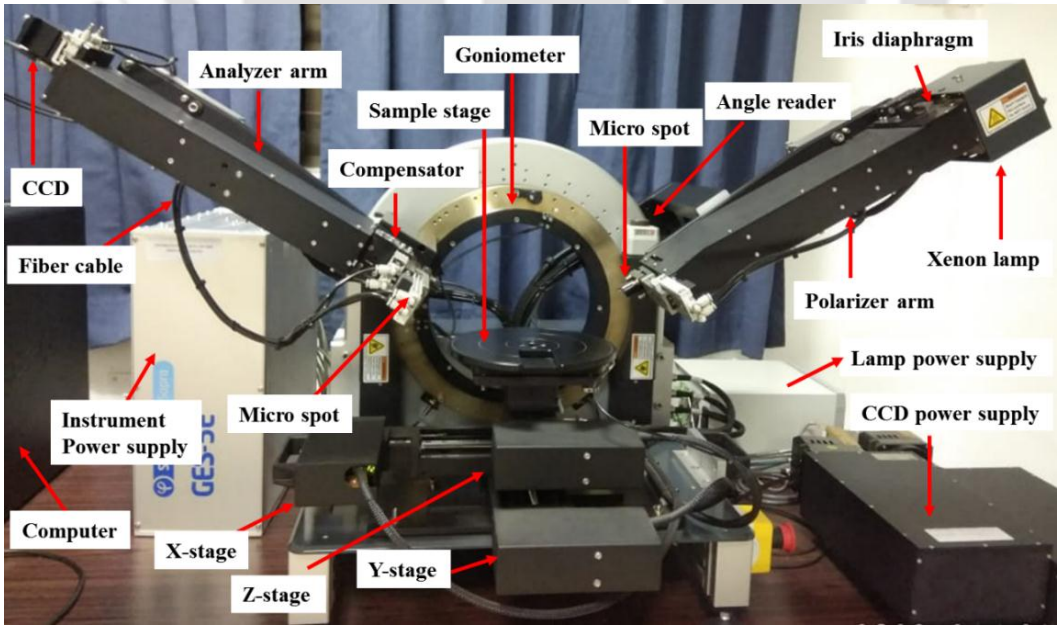

Figure 2.4: *Photograph of SE (model no.: Semilab GES5-E).*

The analysis was carried out by screening several realistic physical models and appropriate layer structure so as to obtain the best fit, having minimum value of RMSE. The best fitted model are described in *section 3.4.2, chapter 3* and *section 4.5.2, chapter 4*.

2.2.5 Modified *Z*-scan setup

To study the NLO properties of PLD thin films of Cu, the modified Z-scan technique was employed [14, 15]. Figure *2.5* and *2.6* show the schematic of the modified Z-scan setup assembled in house and its photograph, respectively.

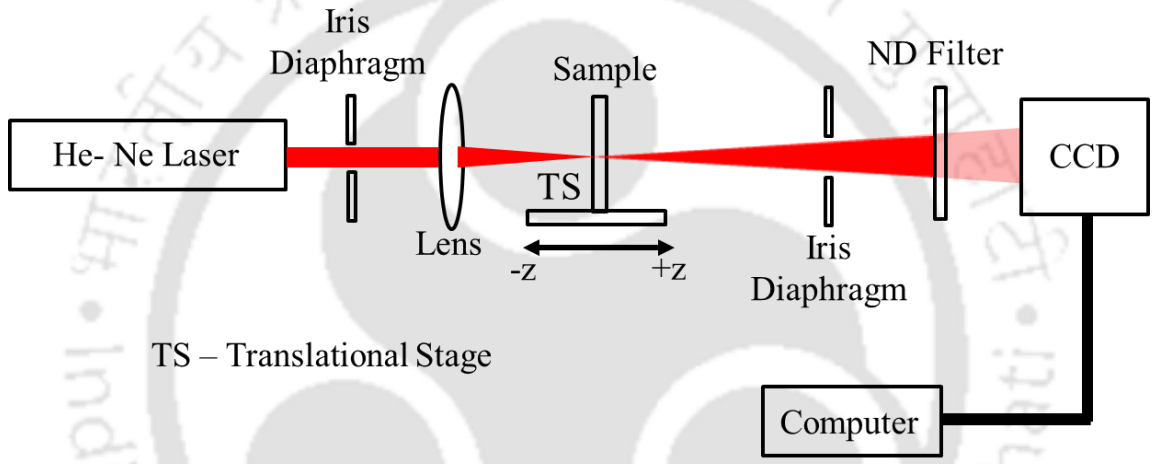

Figure 2.5: *Schematic of modified Z-scan setup.*

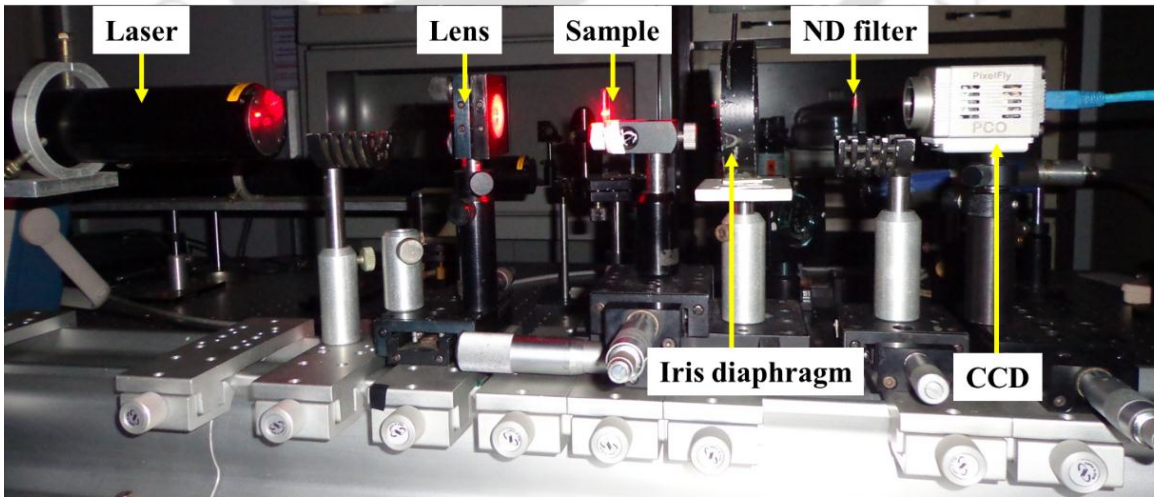

Figure 2.6: *Photograph of modified Z-scan setup.*

A cw He–Ne laser (*Melles Griot, 05-LHP-927*, 632.8 nm), power 35 *mW*, was focused using a plano-convex lens (f = 5 cm) onto the Cu film. The intensity of the laser beam at the focal point was estimated to be 1.46×10^3 W/cm^2. The transmitted beam through the sample as a function of sample position with respect to the focus was imaged on a charge-coupled device (CCD), model *PCO PixelFly*, interfaced to a computer. An iris diaphragm of diameter 1.8 mm was placed in front of the laser to suppress the back-reflected light from the surface of the lens entering into the laser. Another iris diaphragm of 8 mm diameter was placed after the lens to avoid any unwanted scattered light entering into CCD. Neutral density filters were placed in front of CCD to prevent its saturation. The images of the transmitted beam were recorded by scanning the sample up to 15 mm on either side of the focal position of the lens. In this set-up, information about the open as well as closed aperture (CA) Z-scan can be deduced simultaneously from only one set of scanned images. The open aperture (OA) transmission, obtained by integrated intensity over the entire image as a function of distance with respect to focal point, gives the information about the absorptive nonlinearity present in the sample and hence nonlinear absorption coefficient can be determined [15]. The information about the CA Z-scan was obtained by implementing a suitable synthetic aperture through a MATLAB programme in the central region of the images of OA Z-scan. The integrated intensity of these partially masked images was the measure of the nonlinear refractive index coefficient [15]. The measurement details on NLA and NLR coefficients using this modified Z-scan setup are mentioned in *Chapter 5*.

2.3 PLD nanostructured semitransparent Cu thin film as a viable SERS template

The viability of surface enhanced Raman spectroscopy of PLD nanostructured Cu thin film was tested on the metallic single wall carbon nanotube (M-SWCNT). Overall five

samples were prepared to test the efficacy of Cu thin films for SERS as displayed in *figure 2.7*. The sample no. 1-3 were prepared on the glass substrate. In order to compare the effect of substrate, two more samples, 4 and 5 were prepared on silicon (Si) substrate.

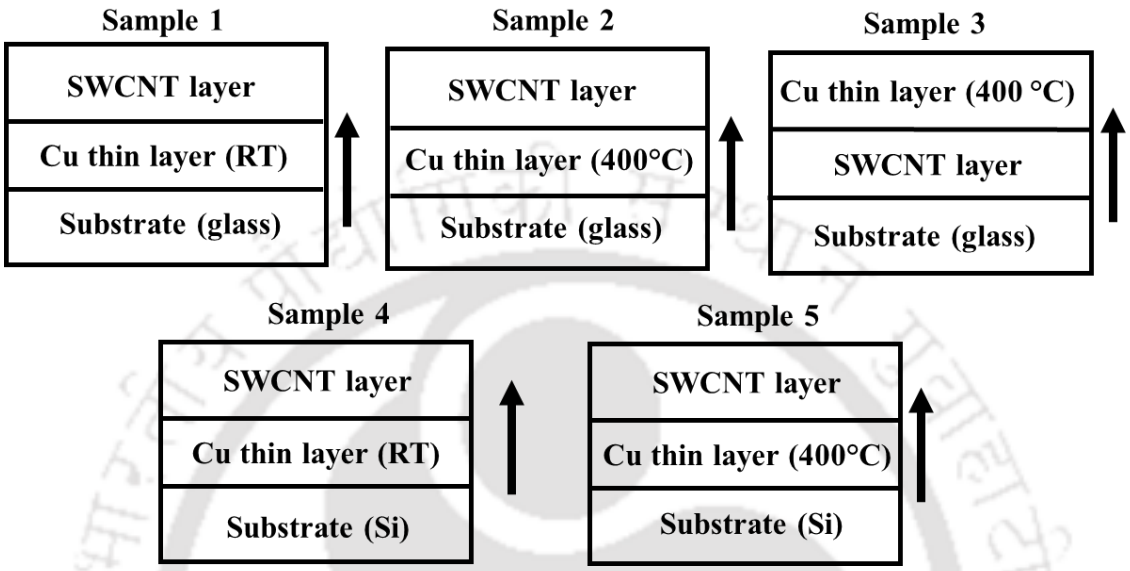

Figure 2.7: *Schematic of SERS samples on glass and Si substrate.*

For the sample 1 and 2, PLD Cu thin film was deposited on glass substrate at RT and at 400°C respectively for one minute duration via 3rd harmonic (355 nm) of Nd:YAG laser keeping rest of the parameters same as described in *section 2.1*. The well dispersed solution of M-SWCNT was prepared in Dimethylformamide (DMF) and drop casted on the top of the Cu films and dried. For the sample 3, the M-SWCNT was drop casted on the bare glass substrate first and then Cu thin film was deposited on it at 400°C exactly in the same manner as described above. Sample 4 and 5 were exactly similar to those of sample 1 and 2 respectively except that these were prepared on the Si substrate. Raman spectra of all these five samples were recorded using micro-laser Raman spectrometer (Model No. *Horiba Jobin Yvon, LabRam HR800*) operating at a wavelength of 514 nm of Ar ion laser. The laser beam was focused on the sample, using 100X microscopic objective, to a spot of ~1μm diameter on the film surface. Each and every sample was probed at four different

locations. For the comparison of the enhancement factor, the Raman spectra of M-SWCNT drop casted onto the bare glass/Si substrate were also recorded.

2.4 Conclusions

In this chapter, the PLD system for fabrication of semitransparent nanostructured Cu thin film on the glass substrate at RT and at glass softening temperature (~ 400°C) have been detailed. The various characterization instrument used to study the structural and linear and nonlinear optical properties of PLD films are stated briefly along with the preparation of the samples for SERS.

Bibliography

[1] J. Su, Y. Liu, M. Jiang, X. Zhu, Oxidation of copper during physical sputtering deposition: mechanism, avoidance and utilization, arXiv preprint arXiv:1412.2031, (2014).

[2] Y.H. Wang, Y.M. Wang, J.D. Lu, L.L. Ji, R.G. Zang, R.W. Wang, Nonlinear optical properties of Cu nanoclusters by ion implantation in silicate glass, Optics Communications, 283 (2010) 486-489.

[3] R. Becker, A. Devi, J. Weiß, U. Weckenmann, M. Winter, C. Kiener, H.-W. Becker, R.A. Fischer, A Study on the Metal Organic CVD of Pure Copper Films from Low Cost Copper(II) Dialkylamino-2-propoxides: Tuning the Thermal Properties of the Precursor by Small Variations of the Ligand, Chemical Vapor Deposition, 9 (2003) 149-156.

[4] Z. Li, A. Rahtu, R.G. Gordon, Atomic layer deposition of ultrathin copper metal films from a liquid copper (I) amidinate precursor, Journal of The Electrochemical Society, 153 (2006) C787-C794.

[5] D.B. Chrisey, G.K. Hubler, Pulsed laser deposition of thin films, John Wiley & Sons, Inc., 1994.

[6] L.M. Kukreja, S. Verma, D.A. Pathrose, B.T. Rao, Pulsed laser deposition of plasmonic-metal nanostructures, Journal of Physics D: Applied Physics, 47 (2013) 034015.

[7] R.K. Singh, J. Narayan, Pulsed-laser evaporation technique for deposition of thin films: Physics and theoretical model, Physical review B, 41 (1990) 8843.

[8] H.-U. Krebs, M. Weisheit, J. Faupel, E. Süske, T. Scharf, C. Fuhse, M. Störmer, K. Sturm, M. Seibt, H. Kijewski, Pulsed Laser Deposition (PLD)--A Versatile Thin Film Technique, in: Advances in Solid State Physics, Springer, 2003, pp. 505-518.

[9] D. Nečas, P. Klapetek, Gwyddion: an open-source software for SPM data analysis, Open Physics, 10 (2012) 181-188.

[10] I. Horcas, R. Fernández, J. Gomez-Rodriguez, J. Colchero, J. Gómez-Herrero, A. Baro, WSXM: a software for scanning probe microscopy and a tool for nanotechnology, Review of scientific instruments, 78 (2007) 013705.

[11] H. Fujiwara, Spectroscopic ellipsometry: principles and applications, John Wiley & Sons, 2007.

[12] H. Tompkins, E.A. Irene, Handbook of ellipsometry, William Andrew, 2005.

[13] S.A. Maier, Plasmonics: fundamentals and applications, Springer Science & Business Media, 2007.

[14] M. Sheik-Bahae, A.A. Said, T.-H. Wei, D.J. Hagan, E.W.V. Stryland, Sensitive measurement of optical nonlinearities using a single beam, IEEE Journal of Quantum Electronics, 26 (1990) 760-769.

[15] I. Kumar, A. Khare, Modified Z-scan set-up using CCD for measurement of optical nonlinearity in PLD carbon thin film, Optics & Laser Technology, 77 (2016) 51-54.

Chapter 3

Effect of deposition time and annealing temperature on growth parameters and optical and SPR properties of PLD nanostructured Cu thin films deposited at RT

The surface plasmon resonance (SPR), linear and nonlinear optical (NLO) properties etc. of thin film are effected by the growth process [1-4] , hence it is important to have a proper insight onto growth mechanism. The vast variety of thin films are fabricated via physical vapour deposition process (e.g. Pulsed laser deposition (PLD), evaporation, sputtering etc.) [5-7]. Normally, growth of the films at room temperature (RT) via physical vapour deposition can be described as a three-stage process. The first stage involves nucleation process forming an initial distribution of stable clusters/nuclei from deposited ad-atoms. In the next stage, the clusters grow by capturing atoms from the supersaturated ad-atom phase forming the islands till it form the continuous network. Finally, when the adatoms concentration achieves its equilibrium value, the growth of the film continues and thereby increasing the thickness [8, 9]. The RT deposited thin films are of limited use due to weak adhesion to the substrate surface and presence of substantial void area which significantly affects the growth and the performance of unmatured metal nanoparticles [10, 11]. To overcome these shortcomings, either the film is deposited at suitable elevated temperature or the as-deposited RT films are gradually annealed to boost surface diffusion and adhesion to the substrate along with improving the uniformity of the film. During annealing, the surface modification of the nanostructured thin film can be very

complicated and difficult to explain in straightforward manner [11]. The annealing results in increase in the surface energy of the nanoparticles causing enhancement of the diffusion, adsorption and desorption process of the adatoms on the surface of the thin film [8, 9, 12]. The initiation of diffusion process toward interface (lower concentration side of the deposited material) increases the probability of making a bonding with the substrate. This is a desirable process particularly for the metal film deposited on the glass/dielectric surface for the plasmonic application. There is also the possibility to the change in the percentage of the constituent species or phase of the deposited material. Lastly the modification of the Fermi energy levels of the metal nanoparticles in case of films made up of bare metal and subsequently affecting the SPs signal generated at the metal/dielectric interface, linear and NLO properties of the film [3, 13]. Consequently, it can influence the efficiency of the thin film based devices particularly involving the metallic thin film such as plasmonic and photonic devices [14, 15], plasmonic chip [16], microprocessors [17], sensors [18], solar cells [19] etc.

In this chapter, effect of deposition time and annealing temperature on the optical and SPR properties and their correlation with the growth parameters of semi-transparent nanostructured PLD Cu thin films are presented.

3.1 Experimental details

Nanostructure metallic Cu thin films were grown onto glass (coverslip) substrate using PLD technique at RT as detailed in *Section 2.1, Chapter 2*. The films were deposited for the duration of 4, 6 and 8 minutes. For each and every duration five films were deposited in order to study the effect of annealing temperature as listed in *table 2.1* (*section 2.1,* chapter 2). All these samples (a total of 15) were characterized by atomic force microscopy (AFM) for studying the size and shape of nanoparticles, surface morphology and to assess

the surface growth parameters (micro-roughness, correlation length, fractal dimension, activation energy etc.) via power spectral density function (PSDF). The absorbance of the films was measured directly using UV-vis-NIR spectrometers to identify the plasmonic peak. The optical properties of the Cu nanoparticles, the constituent species of the film, interfacial layer thickness and film thickness have been studied by spectroscopic ellipsometry (SE).

3.2 Surface morphology and growth dynamics of the PLD Cu thin films as a function of annealing temperature and deposition time

The effect of deposition time and annealing temperature on the surface morphology and growth dynamics of PLD Cu thin films were gauged from AFM images.

3.2.1 Surface morphology of the PLD Cu thin film via AFM images

The 2D and 3D-AFM images (scan area 2μm × 2 μm) of as-deposited as well as post annealed PLD deposited Cu thin films are shown in *figure 3.1 and 3.2* respectively. The shape of the nanoparticles for the as-deposited film was columnar and changed to conical with broad base after annealing as shown in *figure 3.2*. It was observed that the films deposited of 4 and 6 minutes duration, the root mean square (RMS) roughness (w) increases with the annealing temperature from 0.29 to 12.22 nm and 1.35 to 9.59 nm respectively films. It is due to an increase in the mobility of adatoms after getting surface energy at elevated temperature during the annealing of the film. Thus, the increase of the mobility, causes the surface diffusion [20] and agglomeration of smaller sized particles forming the bigger sized particles which in turn leads to an increased in the roughness of the films [21]. However, for the film deposited for 8 minutes duration, there is hardly any effect of annealing on the surface roughness (from 1.18 to 1.20 nm) and this is due to the fact that the larger deposition duration results in closely packed nanoparticles distributed uniformly

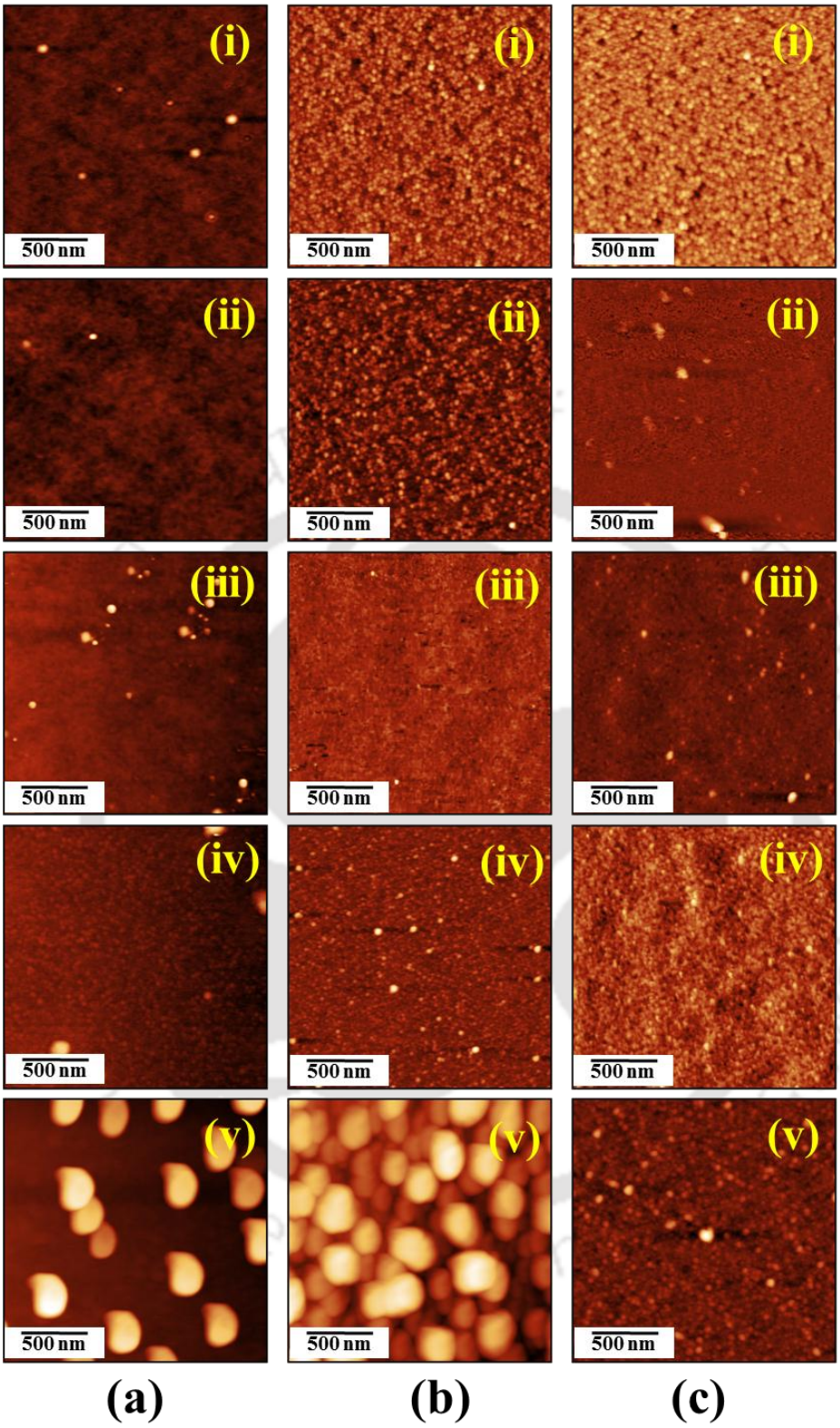

***Figure 3.1**: 2D- AFM images of PLD Cu thin film deposited for (a) 4 minutes, (b) 6 minutes and (c) 8 minutes; (i) as-deposited and post annealed at (ii) 100°C, (iii) 200°C, (iv) 300°C and (v) 400°C.*

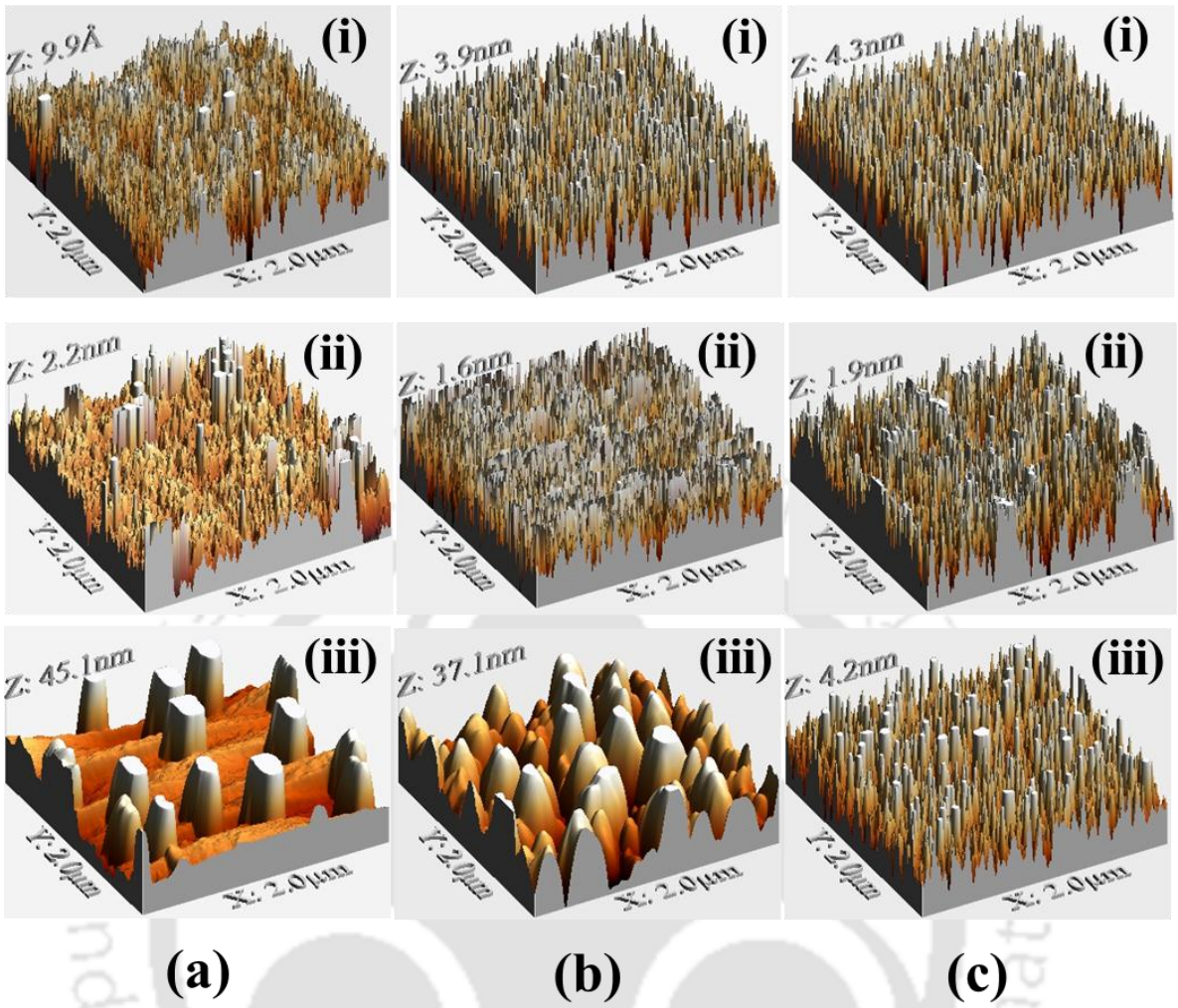

***Figure 3.2**: 3D- AFM images of PLD Cu thin film deposited for (a) 4 minutes, (b) 6 minutes and (c) 8 minutes; (i) as-deposited and post annealed at (ii) 200°C and (iii) 400°C.*

over the surface (*figure 3.1 (c) and 3.2 (c)*). The cluster formation and diffusion (both lateral and vertical) on the surface of thin film are dependent on the surface area of the substrate, density of the nanoparticles, material properties, and annealing temperature [8, 9, 12]. The rate of heating as well as cooling during annealing process and temperature play a major role in the formation of the nanoparticles cluster on the film surface. The slow heating and cooling rate result in the uniform distribution of size and shape of the nanoparticle and better surface morphology on the thin film. The rapid heating/cooling rate near glass

softening temperature may develop the nano range cracks on the surface and formation of the clusters with arbitrary shape and size due to random diffusion of nanoparticles on the film surface. These defects influence the optical and electrical properties of the thin film [22, 23]. Annealing of the film provides the thermal energy to the nanoparticles resulting surface diffusion. The diffusion on the surface of the film, explained by classical mean-field theory, is defined as, $N \propto (1/D)^{1/3}$, where N is the surface density of nanoparticles and D is the surface diffusion coefficient [12]. Thus the high density of nanoparticles on film surface reduces the diffusion and vice versa. This was exactly observed in the present case as displayed in the AFM images of *figure 3.1*. The particles are thinly distributed in the as-deposited films for 4 and 6 minutes and with the increase in annealing temperature up to 200°C, the film surface modified to relatively uniform distribution of the particles indicating the large diffusion. Whereas for the as-deposited film for 8 minutes, the nanoparticles are uniformly distributed and didn't display any significant changes after annealing. Same is reflected into the void distribution in all the three films as shown in *figure 3.3*.

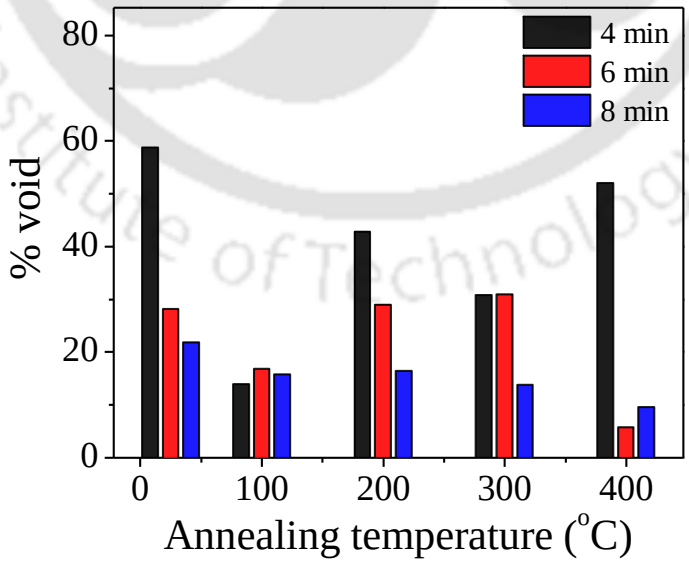

***Figure 3.3**: Variation of percentage of void area on the film surface as a function of annealing temperature.*

The percentage of void for the as-deposited RT films of 4, 6 and 8 minutes duration was ~ 52%, 28% and 22% respectively. Except for the film deposited at 4 minutes, the percentage of void was reduced drastically after annealed the film to finally 400°C as compared to that of the as-deposited film. It was due to the diffusion process on the surface which fills the void area. The 4 minutes as-deposited RT film had more percentage of void area on the substrate surface, so during diffusion process, the smaller clusters experienced less obstacle to diffuse forming the bigger cluster consequently leaving more void space in this film even after final by annealed to 400°C.

The particle size distribution was estimated from 2D AFM images using open excess image J software. The estimated particle size (or lateral size) was averaged over three different locations on the surface of each film and is shown in *figure 3.4 (a-c).*

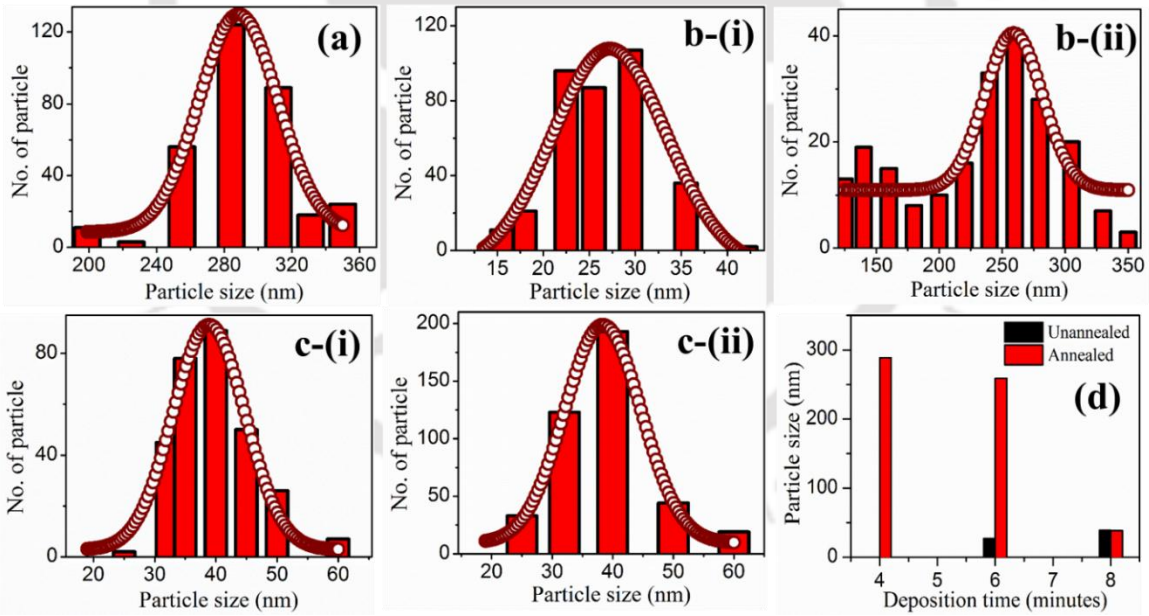

Figure 3.4*: Particle size distribution of PLD nanostructured Cu thin films deposited for (a) 4 minutes at 400 °C, (b) 6 minutes (i) RT and (ii) 400 °C, (c) 8 minutes (i) RT and (ii) 400 °C and (d) Comparison of average particle size as a function of deposition time for as-deposited and post annealed film at 400ºC.*

The comparison of the average particle size as a function of deposition time for as-deposited (at RT) and post annealed films to a final temperature of 400°C is shown in *figure 3.4 (d)*. It was observed that the average size of the nanoparticles of the as-deposited film for 4 minutes duration was less than 10 nm whereas that of the 6 and 8 minutes duration film was 27 and 38 nm respectively. After gradual annealing to a final temperature of 400°C, the average particle size of 4 and 6 minutes films has grown to 288 and 259 nm respectively whereas that of for 8 minutes film remained unchanged. The increase in the size of the nanoparticles was again due to the surface diffusion phenomena which was larger for the film deposited for 4 and 6 minutes duration (annealed films) than that of the 8 minutes duration film. Due to the diffusion, the smaller particles coalesces to form the bigger particles. However, for 8 minutes duration film, the density of the nanoparticles was large (~ 22% void) which hardly left any space for the redistribution during annealing, hence the size distribution remained unchanged.

3.2.2 Growth dynamics of the PLD nanostructure Cu thin film via PSDF

The growth dynamics of the films was unveiled from AFM images only. The micro-roughness (MR), correlation length (CL), growth exponent, fractal dimensions (FD), diffusion coefficient (D) and activation energy (E_a) for PLD grown films were obtained from PSDF of the corresponding AFM images [24-26]. The behaviour of surface height, $h(\boldsymbol{r}', t)$, at a point r' (shown in *figure 3.5 (a)*) is related to correlation length (ξ) which represents the short-range lateral behaviour of the surface as shown in *figure 3.5 (b)* for one dimension. Beyond the correlation length, the surface height is not correlated. To measure the long-range behaviour, the PSDF, also known as the structure function, is used. The PSD is related to a Fourier transform of the surface heights, defined in reciprocal space as [27]

$$P(\boldsymbol{k},t) \equiv \frac{1}{(2\pi)^{d'}} \left|\langle h(\boldsymbol{r}',t)e^{-i\boldsymbol{k}.\boldsymbol{r}'}\rangle\right|^2 \quad (3.1)$$

The advantage of the PSDF spectrum is that it directly gives information about the type of surface growth (self-affine or mounded). It shows the characteristics peak, $k_m = 2\pi/\lambda$ (λ= wavelength, *figure 3.5 (b)*) for mounded surface only and for self-affine surface such peak is missing [28].

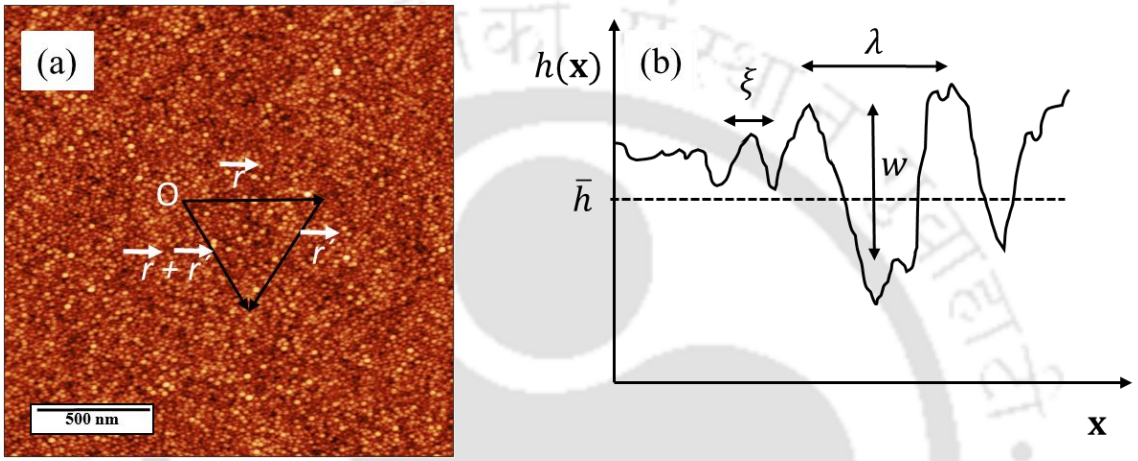

***Figure 3.5**: (a) 2D-AFM images of PLD Cu films and (b) definitions of various scaling parameters; mean height h, interface width w, lateral correlation length ξ, and wavelength λ.*

In the present works, the measurement has been performed at three distinct positions within the scan area of 2 μm × 2 μm. The PSDF spectra have been recorded separately for each scan using open source Gwyddion software [29]. To calculate the surface characteristic parameters (fractal dimension, micro-roughness etc.) using PSDF spectra, an appropriate analytical model was applied [27]. As an example, the recorded PSDF spectra of PLD Cu film, deposited for 8 minutes duration and final by annealed to 400°C, is shown in *figure 3.6*, from the AFM image of Cu thin film, as a function of spatial frequency. This spectrum can be divided into two distinct regions; (1) the higher frequency region providing information about roughness exponent, FD, surface diffusion etc. and (2) The lower

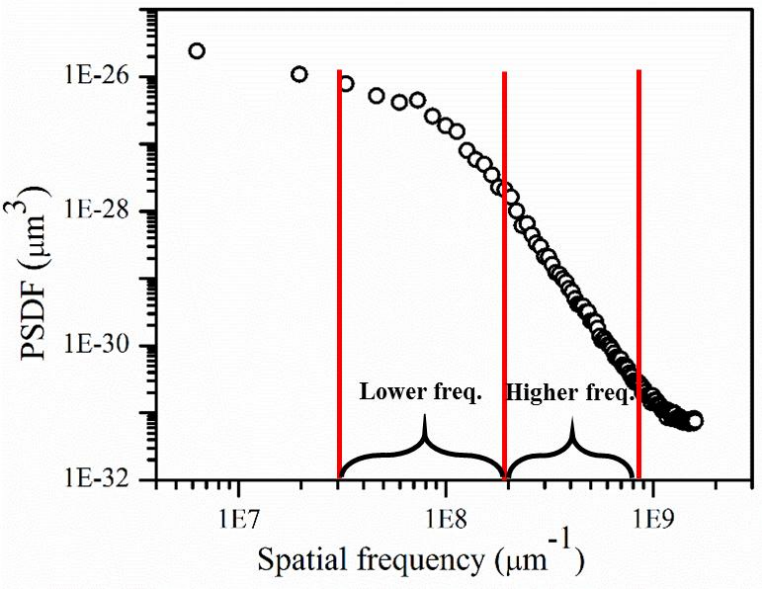

***Figure 3.6**: PSDF spectrum extracted from AFM image of 8 minutes duration nanostructure PLD Cu thin film.*

frequency region giving information about MR, CL, activation energy (E_a) etc. The higher frequency region of the PSDF graph was fitted with fractal model, which obeys the inverse power law [30]

$$PSD_{fractal}(k; K', \nu) = \frac{K'}{k^{\nu+1}} \qquad (3.2)$$

where K' is the spectral strength, k is the spatial frequency, $\nu = d' + 2\alpha'$; is the spectral indices of the fractal surface, d' is the dimension of the system (d'=2), and $\alpha'$is the roughness exponent. The fractal PSD model is valid only for the self-affine surface. The fractal dimension, D_f, is related to the slope ν in a log-log plot as [31, 32]

$$D_f = \frac{7-\nu}{2} \qquad (3.3)$$

Depending in the range of D_f, fractals can be classified into three categories; marginal fractals $0 < D_f < 1$, Brownian fractal $1 < D_f < 2$ and extreme fractal $2 < D_f < 3$ [26, 33]. Fractal provides the complete quantitative information about the surface morphology and

surface diffusion in the thin films. Additionally, the Hurst exponent (*HE*), defined as $HE = 3\text{-}D_f$, describes the raggedness of the film surface after the surface diffusion [33]. The higher value of Hurst parameter corresponds to smooth diffusion of the nanoparticles on the surface of the film.

The lower frequency region, (above knee), *figure 3.6* of the PSDF graph was fitted with Gaussian function to extract the information about the nanoparticles on the surface [26, 34]

$$PSD_{knee}(k; \sigma_{sh}\tau_{sh}k_{sh}) = \pi\tau_{sh}\sigma_{sh}^2 exp[-\pi^2\tau_{sh}^2(k - k_{sh})^2] \quad (3.4)$$

where, σ_{sh} , $\tau_{sh}$and f_{sh}correspond to micro roughness, correlation length and shift in the PSD maximum respectively.

The PSDF spectra for all the PLD deposited nanostructured Cu thin films, at various annealing temperature and deposition time, have been fitted with the analytical model described by *equation 3.2* and *3.4* in higher and lower frequency region respectively are shown in *figure 3.7*. The growth/surface characteristic parameters extracted from the fractal and Gaussian models are listed in *table 3.1*. The micro roughness (MR), σ_{sh}, of the film describes the roughness of island or nanoparticles. It was observed that MR of the PLD Cu thin film initially increases from as-deposited RT to 100°C and thereafter it decreases at 200°C of annealing temperature. With the further increase in the annealing temperature from 300°C to 400°C, the MR of the film increases drastically for all the three deposition durations. This indicates that there are different diffusion rates for below and above 200ºC of annealing temperature. This is further confirmed by the activation energy analysis describe towards the end of this section. The rate of the surface diffusion during annealing can be measured by Hurst exponent (*HE*). The higher Hurst value corresponds to a smooth diffusion (listed in table 3.1).

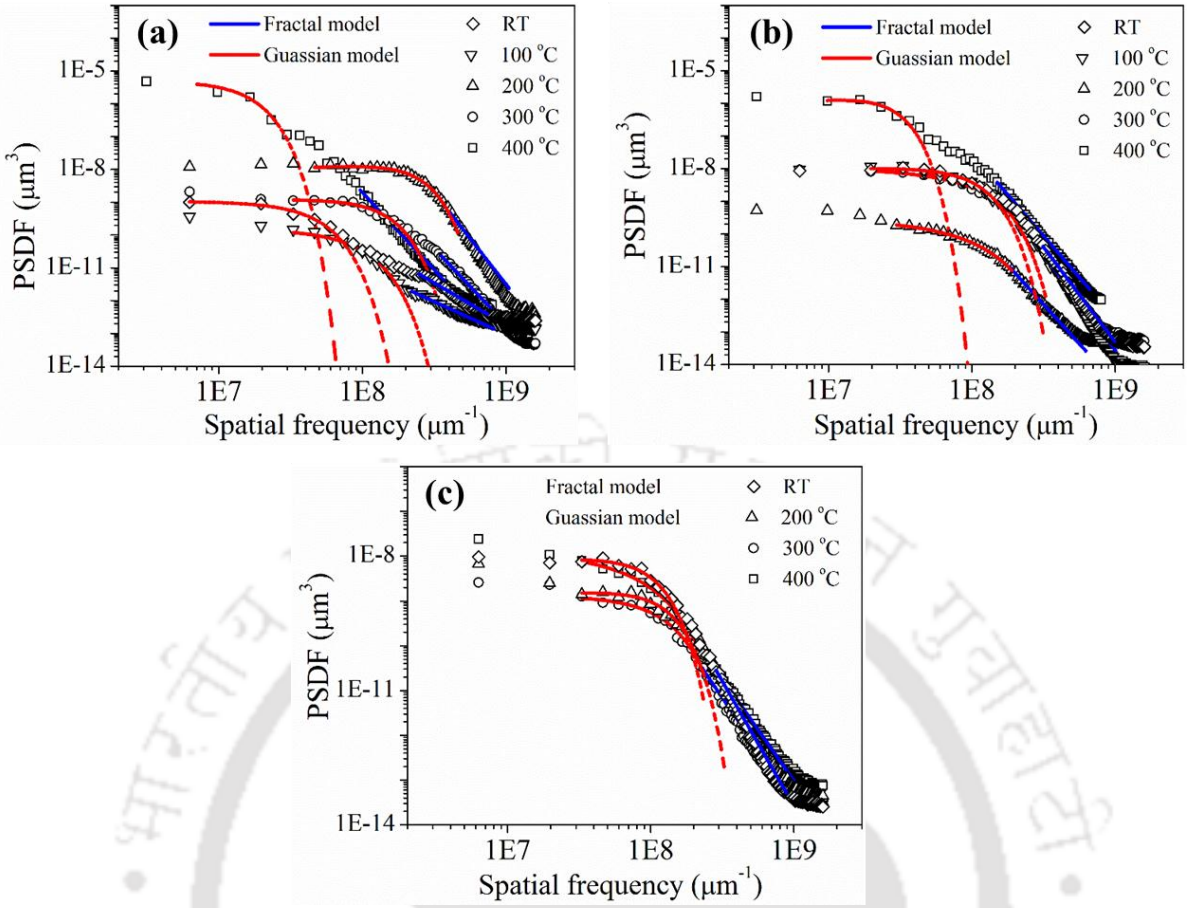

***Figure 3.7**: PSDF spectra of PLD Cu thin film for (a) 4 minutes, (b) 6 minutes and (c) 8 minutes, as a function of spatial frequency.*

***Table 3.1**: Growth parameters extracted from PSDF as a function of annealing temperature and deposition time.*

T (°C)	4 minutes			6 minutes			8 minutes		
	σ_{sh} (nm)	D_f	*HE*	σ_{sh} (nm)	D_f	*HE*	σ_{sh} (nm)	D_f	*HE*
As-deposited	0.27	2.71	0.28	0.95	1.09	1.90	0.89	1.22	1.77
100	0.44	2.5	0.46	1.50	1.07	1.92	--	--	--
200	0.34	1.60	1.39	0.64	1.10	1.90	0.38	1.19	1.81
300	0.72	1.69	1.30	2.42	1.58	1.89	0.75	1.65	1.34
400	8.57	1.64	1.35	5.44	1.42	1.57	3.79	1.72	1.28

The value of fractal dimension, D_f, value for the as-deposited film of 4 minutes duration is 2.71 indicating the extreme fractals whereas that of deposited for 6 and 8 minutes indicate the Marginal fractal nature. However, after gradual annealing to a final temperature of 400°C, the nature of fractal changed to Brownian fractal having D_f values of 1.64, 1.42 and 1.72 irrespective of the deposition time. Since for higher deposition duration (8 minutes), the density of the nanoparticles increases which slows down the surface diffusion and so the excessive surface energy is likely to modify the Fermi energy level of the nanoparticles [12, 35].

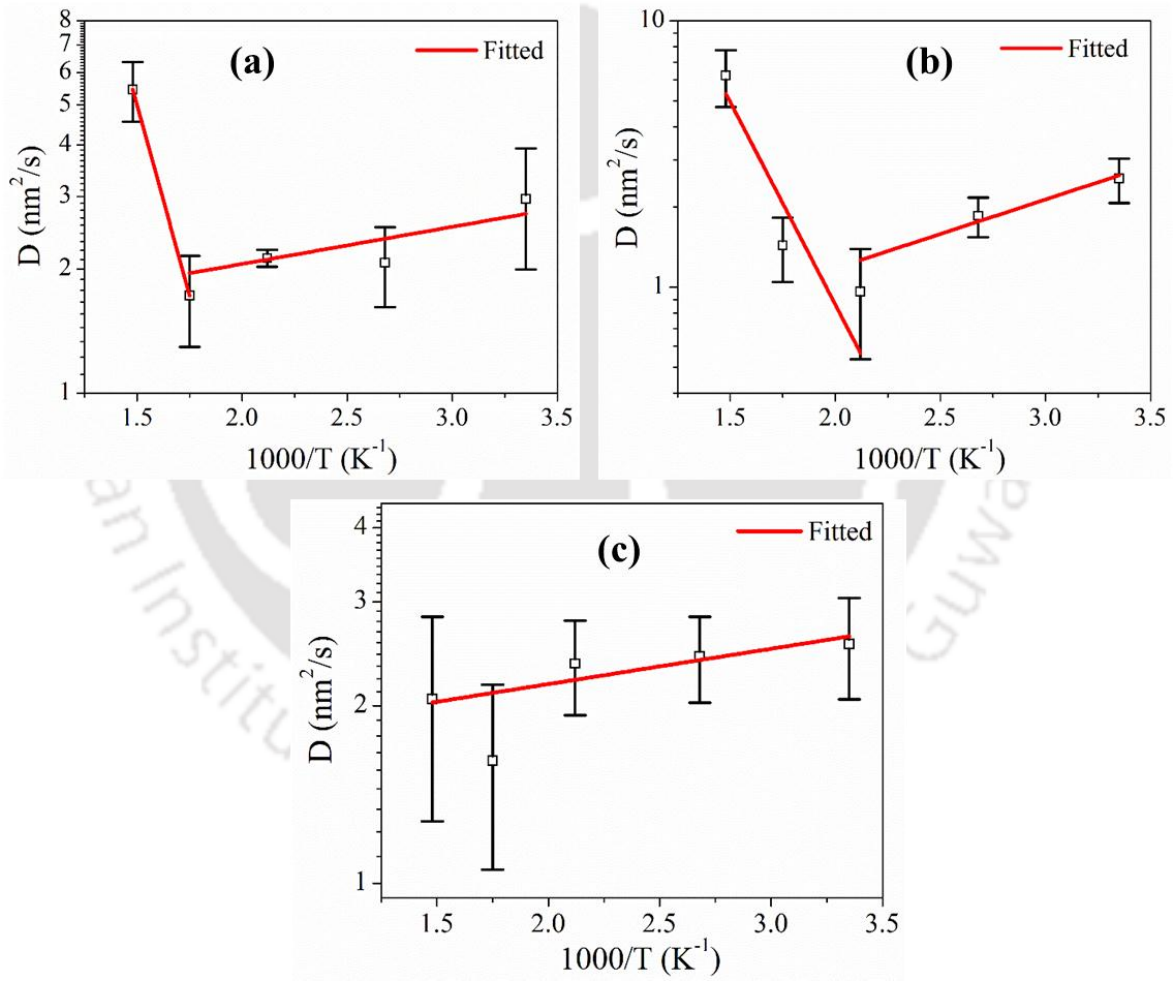

***Figure 3.8**: Diffusion coefficient (D) of the PLD Cu thin film for (a) 4 minutes, (b) 6 minutes and (c) 8 minutes, as a function of 1/T (K^{-1}).*

The coefficient of surface diffusion is proportional to the square of the correlation length or diffusion length. The activation energy of the thin film has been assessed from the surface diffusion coefficient which is defined as [12, 24]

$$D = D_o exp\left(-\frac{E_a}{k_B T}\right) \quad (3.5)$$

where D_o is the temperature-independent pre-exponential, E_a is the activation energy, k_B is the Boltzmann constant and T is the annealing temperature. The activation energy of the film provides the quantitative information on the amount of the thermal energy (during annealing) is used to modify the Fermi energy level of the nanoparticles and diffusion on the surface [12, 36]. The variation of the diffusion coefficient with the annealing temperature for all the samples is shown in the *figure 3.8*, and fit to *equation 3.5*. In order to estimate calculate the activation energy of the film. A negative activation energy, E_a, of ~ -0.091 and -0.258 eV was observed up to annealing temperature of 200°C for 4 and 6 minutes films respectively, and then it became positive having values of ~ 1.850 and 1.521 eV for annealing temperature of 400°C. The as-deposited 8 minutes duration film showed negative activation energy, E_a ~ -0.060 eV and there was hardly any effect of annealing for this film. The negative value of activation energy signifies the surface diffusion process whereas that of the positive value indicates that the change in chemical potential (Fermi energy) of the nanoparticles is dominant [37].

3.3 Surface plasmon resonance properties of semi-transparent nanostructured Cu thin films

The absorption spectra of the PLD deposited Cu thin films in the spectral range of 1 eV to 4 eV for the 4, 6 and 8 minutes deposition duration of the as-deposited (RT) and gradual annealed films are shown in *figure 3.9 (a-c)*. The position of SPR peaks as a function of deposition time is shown in *figure 3.9 (d)*. None of the as-deposited films

displayed any prominent absorption peak, indicating the absence of SPR. The Cu thin film deposited for 4 minutes duration displayed longitudinal mode (LM) as well as transverse mode (TM) SPR peaks, only after final annealing temperature of 400°C, around 1.77 eV (700 nm) and 2.39 eV (518 nm) respectively. The film deposited for 6 minutes duration at RT and post annealed to 100°C, 200°C, 300°C were showing the weak signature of SPR peak at 2.35 eV (528 nm), 1.84 eV (673 nm) and 1.81 eV (685 nm) respectively. This sample after finally annealed to 400°C film, exhibited the LM and TM SPR peaks around 1.68 eV (734 nm) and 2.39 eV (521 nm) respectively.

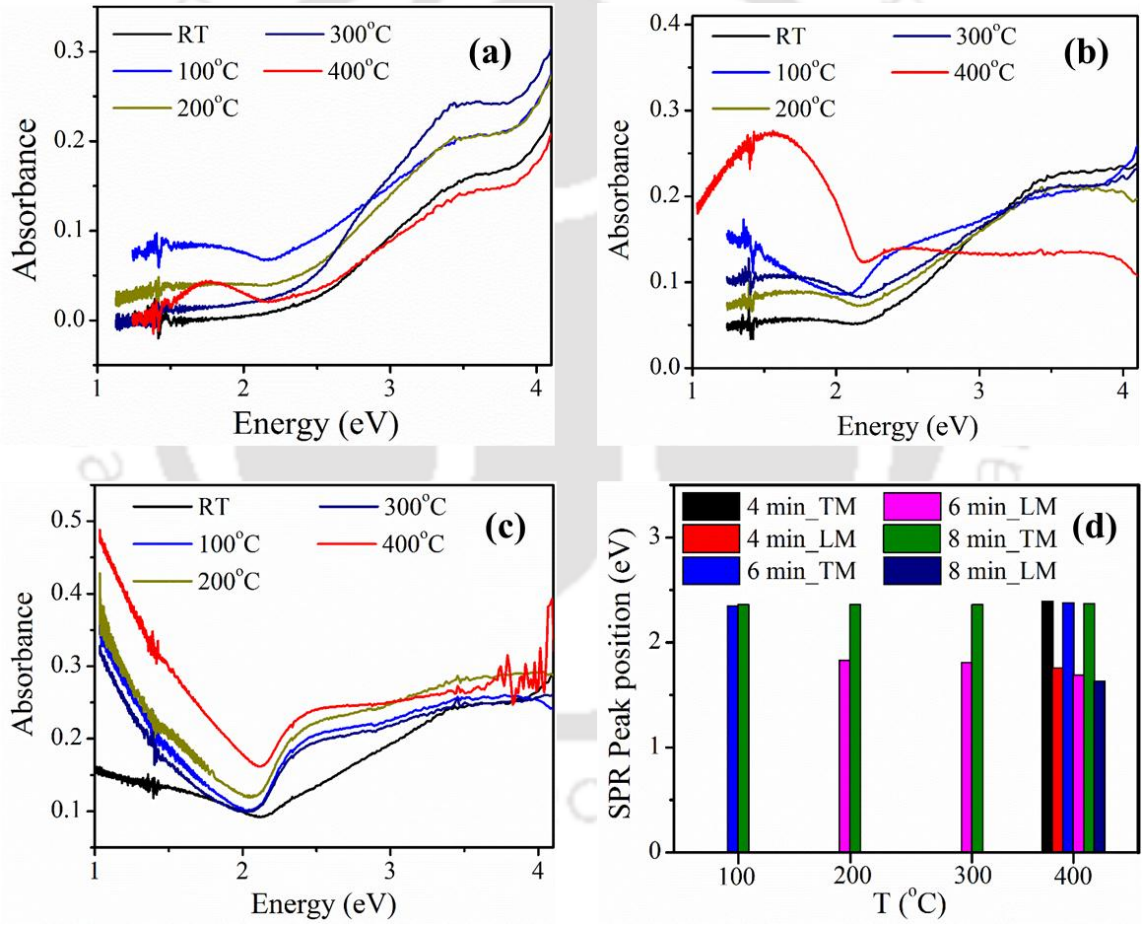

***Figure 3.9**: Absorption spectra of PLD nanostructured as-deposited at RT and gradually annealed to 400°C Cu thin film for deposition time of (a) 4 minutes, (b) 6 minutes, (c) 8 minutes and (d) Variation of SPR peak position as a function of the annealing temperature.*

The Cu thin film deposited for 8 minutes duration exhibited small signature of SPR after post annealing from 100°C to 300°C. However, the SPR peak did not shift much within the temperature range of 100°C-300°C, exhibited peak around ~2.37 eV (523 nm). This sample after finally annealed to 400°C, exhibited the LM and TM SPR peaks around 1.63 eV (760 nm) and 2.37 eV (523 nm) respectively. From above, it is concluded that the films annealed at 400°C exhibited strong plasmonic properties.

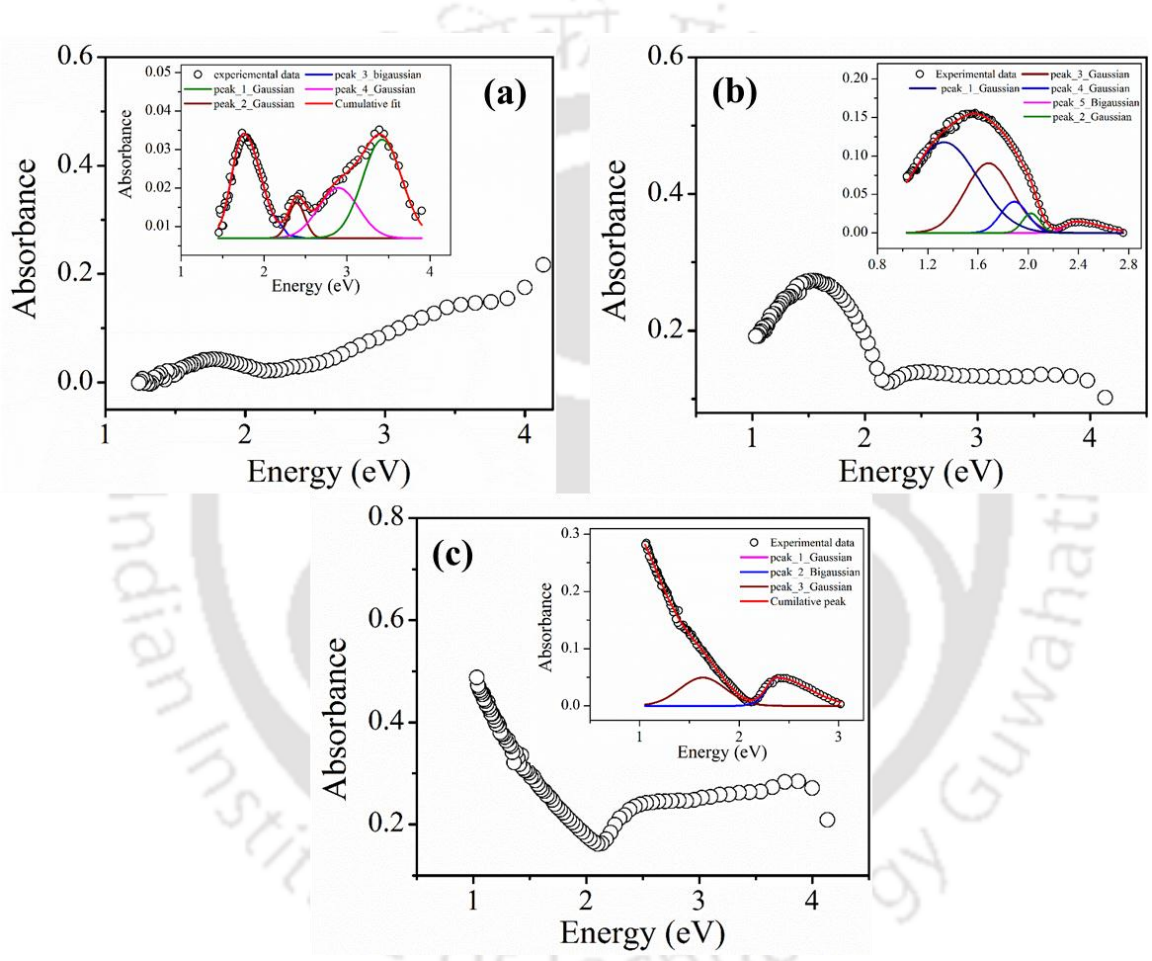

Figure 3.10*: Absorption spectra of semi-transparent PLD nanostructured Cu thin film gradually annealed to a final temperature of 400°C for the deposition time of (a) 4 minutes, (b) 6 minutes and (c) 8 minutes.*

The recorded absorption spectra of the all the samples, exhibited the broad peak between the energy range of 3 - 4 eV and is due to the interband transition. This is further confirmed

by the SE analysis. The absorption spectra of PLD deposited nanostructured Cu films, after gradual annealing to a final temperature of 400°C, show the multiple peaks apart from prominent SPR peak and so de-convoluted with skew-symmetric bi-Gaussian and Gaussian analytical equation [38, 39] and is shown in this inset of *figure 3.10*. The additional peaks correspond to the interband transition of the Cu nanoparticles. The various peaks obtained after de-convolution of the absorption spectra are listed in the *table 3.2*.

***Table 3.2**: De-convoluted peaks of the absorbance spectra of annealed films up to 400°C with deposition time.*

Deposition time (minutes)	Aspect ratio	Peak_1 E_{01} (eV)	Peak_2 E_{02} (eV) (TM)	Peak_3 E_{03} (eV) (LM)	Peak_4 E_{04} (eV)	Peak_5 E_{05} (eV)
4	6.38	3.42±0.019	2.39±0.004	1.76±0.002	---	2.89±0.037
6	6.90	1.33±0.060	2.38±0.014	1.69±0.036	1.89±0.030	2.02±0.010
8	9.04	0.80±0.073	2.37±0.005	1.63±0.026	---	---

The first peak (E_{01}) is due to the interband transition energy of the Cu nanoparticles for all the samples [40, 41]. The second (E_{02}) and third (E_{03}) peaks are due to the TM and LM of SPR of the Cu nanostructured thin films as mentioned earlier. The forth peak (E_{04}), observed only in 6 minutes deposited film, corresponds to another SPR peak which could be due to the shape of the nanoparticles (*figure 3.2 (b-(v))*) [42]. However, the fifth peak (E_{05}) is due to the presence of the different copper species formed during annealing of the films (such as the diatomic Cu, copper oxides etc.) discussed in the next *section 3.4*. For the nanoparticles having shape other than spherical, the position of the SPR peaks (transverse and longitudinal) depend on its aspect ratio [43]. It has been reported that for prolate geometry, as the aspect ratio increases, the TM is blue-shifted (higher energy) whereas LM is red-shifted (lower energy) [42]. The shift in the TM is small (negligible) for prolate geometry as compared to that of LM [42]. In the present case, the shape of the

nanoparticles was nearly columnar, similar to the prolates geometry (*figure 3.2*). Therefore, as the aspect ratio increases with the deposition time, *table 3.2*, the shift in E_{02} peak, (TM of SPR), is not significant whereas the E_{03} peak (LM of the SPR), moved toward lower energy. It is concluded that the SPR peak position is dependent more on the shape of the nanoparticles compared to that of the size. Relatively distinct appearance of SPR peaks for finally annealed film at 400°C indicates that the film is of self-affine in nature as also concluded in *section 3.2* [44, 45].

3.4 Optical properties of as-deposited and gradually annealed PLD nanostructure Cu thin film via spectroscopy ellipsometer

The annealing of films near the glass softening temperature (~ 400°C) diffuses the particles from the film towards the substrate or vice versa forming an interfacial layer of oxide in the present case and may influencing the plasmonic properties of these films strongly. Therefore in order to access the plasmonic properties, it is necessary to have an idea of the interfacial layer thickness and its stoichiometry. Therefore the as-deposited RT and post gradually annealed to a final temperature of 400°C of 4, 6 and 8 minutes films were subjected to SE analysis in order to study the influence of deposition time and annealing temperature on the interfacial layer thickness and its composition along with other optical properties (e.g. SPR, other oscillators etc.).

3.4.1 Layer structure considered for ellipsometric analysis via BEMA

The analysis of SE data requires an appropriate layer structure and model for the sample. In the present system of PLD Cu thin film, the assumed layer structure using Bruggman effective medium approximation (BEMA) model [46, 47] for the estimation of the volume fraction and the type of the constituent species of the semi-transparent PLD Cu thin film is shown in *figure 3.11 (a) and (b)* for the as-deposited film at RT and that of the

post annealed (at 400ºC) films respectively. The enlarge view of main PLD Cu layer consisting of nanoparticle of Cu (NP Cu), void for as-deposited film and NP Cu, diatomic Cu (Cu (II)), Cu_2O and void for annealed film with in the probe area is also shown below the respective layer structure in *figure 3.11*.

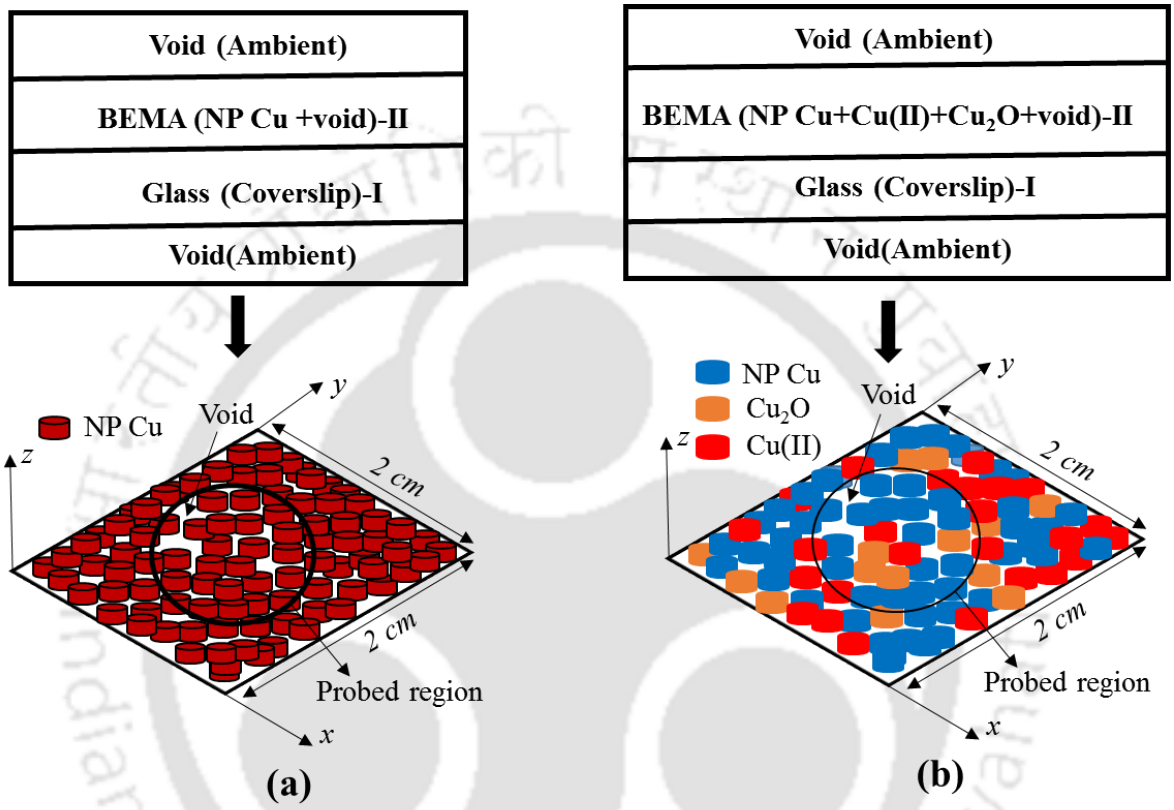

***Figure 3.11**: Schematic of the assumed layer structure of PLD Cu thin film (a) as-deposited RT and (b) post annealed film at 400ºC.*

The first bottom most dielectric layer in both the sets (unannealed and annealed) is of glass substrate (coverslip) having a thickness of 10^5 nm, which is much larger compared to that of the film thickness. The second layer in the as-deposited case, *figure 3.11 (a)*, above the substrate comprised of the main layer of PLD Cu nanostructured thin film which is a combination of the plasmonic NP Cu and void. However, in case of post annealed film, the second layer is a combination of the plasmonic NP Cu, Cu (II) and copper oxide (Cu_2O) along with the voids (empty space) in between these species. The space above the top layer

and below the substrate is void in both the cases as shown in *figure 3.11*.

3.4.2 Bruggeman Effective medium approximation for PLD Cu thin film

To determine the type of the constituent species in the thin film, the numerical simulation of the ellipsometer spectra were performed using BEMA assuming a two layered structure as shown in *figure 3.11*. In BEMA, the effective complex dielectric function, ε, of the thin film composed of *n* number of species, can be written as [47]

$$\sum_i^n f_i' \frac{\varepsilon_i - \varepsilon}{\varepsilon_i + 2\varepsilon} = 0 \qquad (3.6)$$

where ε_i and f_i' are the dielectric function and volume function of i^{th} species (or phase) *i* respectively, contained in the entire probed volume. For as-deposited film, *i* = 1 and 2 corresponding to NP Cu (plasmonic_I) and voids only. For post annealed film *i* = 1 to 4 corresponding to Cu_2O (cuprous oxide), Cu (II), void and NP Cu (plasmonic_II) respectively. The values of ε_i ; ε_{Cu_2O}, $\varepsilon_{Cu\,(II)}$ and ε_{void} were taken directly from the system generated file (from SEA software) [48] whereas for $\varepsilon_{Plasmonic\_I}$ *and* $\varepsilon_{Plasmonic\_II}$ for as-deposited and annealed film, respectively, were determined using the suitable dispersion law formed with a combination of Lorentz [47] and Gauss [49] oscillators (L-G). This multi-oscillator model for as-deposited RT film can be expressed as [38, 50]

$$\varepsilon_{plasmonic\_I} = \varepsilon_{Lorentz} + \varepsilon_{Guass} + \varepsilon_{\infty} \qquad (3.7)$$

It consists of combination of one Lorentz oscillator ($\varepsilon_{Lorentz}$) and one Gauss oscillators (ε_{Gauss}) describing the interband transition and transverse mode of the SPR (near UV region) respectively whereas the quantity ε_{∞} (usually $1 \leq \varepsilon_{\infty} \leq 10$) corresponds to contribution of the residual polarization due to the positive charged background of the ionic cores [51]. For the post annealed PLD nanostructured Cu thin film, dielectric function, $\varepsilon_{plasmonic\_II}$, was determined using a dispersion law formed by the combination of one

Lorentz and three Gauss oscillators (L-G). The multi-oscillator model for gradually annealed film can be expressed as [38, 50]

$$\varepsilon_{plasmonic\_II} = \varepsilon_{Lorentz} + \sum_{j=1}^{3} \varepsilon_{j\ Gauss} + \varepsilon_{\infty} \qquad (3.8)$$

The contribution of interband transition in $\varepsilon_{plasmonic\_II}$ was modeled using one Lorentz oscillator $\varepsilon_{Lorentz}$ while two Gauss oscillators $\varepsilon_{j\ Gauss}(j = 1, 2)$ describing the TM and LM of SPR and contribution due to oxide was modeled using the third Gauss oscillator which takes into account its effect on the plasmonic nanoparticles of Cu.

Figure 3.12 (a) and *(b)* illustrate the experimental data and the fitted curve via BEMA model of ellipsometric functions; *tan ψ* and *cos Δ* as a function of energy respectively for the physical models described by *equation 3.6, 3.7 and 3.8* discussed in *section 3.4.1* for which the RMSE value was least. The values of RMSE with deposition time and annealing temperature are listed in *table 3.3*.

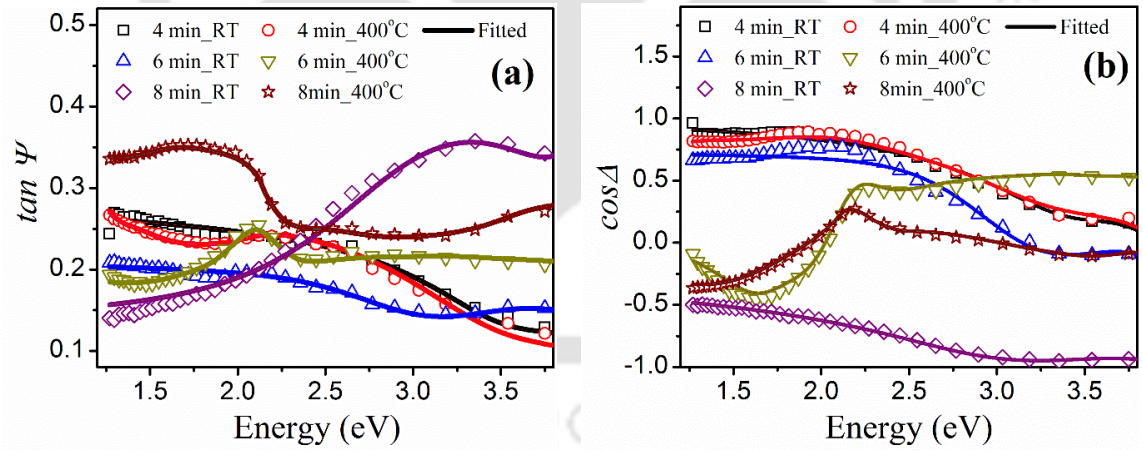

***Figure 3.12**: The experimental and fitted graph of PLD nanostructured Cu thin film as the function of energy (a) tanψ and (b) cosΔ.*

The estimated values of percentage of the constituent species with deposition time for as-deposited and post annealed films (finally to 400°C) from BEMA are listed in *table 3.4* and

***Table 3.3**: RMSE values with the deposition time.*

S.No.	Deposition time (minutes)	Unannealed/ Annealed	RMSE
1	4	Unannealed	0.0052
		Annealed	0.0050
2	6	Unannealed	0.0081
		Annealed	0.0031
3	8	Unannealed	0.0069
		Annealed	0.0026

***Table 3.4**: Thickness and percentage of the constituent species for as-deposited films with the deposition time.*

Deposition Time (minutes)	Thickness (nm)	% NP Cu	% void	% void via AFM
4	11.50±0.001	42.00	58.00	58.00
6	17.70±0.003	66.00	34.00	28.00
8	30.60±0.001	73.18	26.82	22.00

***Table 3.5:** Thickness and percentage of the constituent species for post annealed films (up to 400°C) with the deposition time.*

Deposition Time (minutes)	Thickness (nm)	% NP Cu	% Cu(II)	% Cu_2O	% void	% void via AFM
4	11.45±0.002	38.90	0.75	---	60.35	52.00
6	18.80±0.001	74.28	14.70	11.01	---	5.00
8	32.40±0.002	48.44	34.16	17.39	---	9.00

3.5 respectively. The as-deposited (RT), unannealed, Cu thin films have large void percentage compared to that of the annealed films (except 4 minutes film). The percentage of void estimated from SE in the as-deposited film was 58 %, 34 % and 26% for 4, 6 and 8

minutes deposited film respectively. The presence of substantial void space in between the nearby nanoparticles suppressed the plasmonic signal of the 4 minutes deposited film as compared to that of 6, 8 minutes annealed films (*figure 3.9*). It was observed that the void percentage of the as-deposited film decreases with an increase in the deposition time whereas the thickness of the film increases, *table 3.4*. There is a reasonable agreement in the measured percentage of void area using ellipsometer with those of AFM (*figure 3.3*). In the process of annealing, the sufficient amount of surface energy has been absorbed by Cu film which modifies the nucleation site, energy level and the phase of the species [12, 52-54]. Therefore, in these films there is a change in the percentage of composition of various species along with the percentage of voids (*table 3.5*).

The 4 minutes deposited post annealed film has least density of metallic nanoparticles compared to that of the other films deposited for 6 and 8 minutes. In this film, ~60% void, ~0.75% copper species ($\varepsilon_{Cu(II)}$) and ~ 38% plasmonic nanoparticle of Cu ($\varepsilon_{plasmonic\_II}$) were found to be present. While the post annealed film deposited for 6 minutes has ~14% copper species ($\varepsilon_{Cu(II)}$), ~11% cupric oxide (ε_{Cu_2O}) and ~74% plasmonic nanoparticle of Cu ($\varepsilon_{plasmonic\_II}$). However, the film deposited for 8 minutes duration, the percentage of the plasmonic NP Cu was reduced to ~49% while $\varepsilon_{Cu(II)}$ and ε_{Cu_2O} were found to be ~34.50% and ~17.50% respectively. The voids in both these films were absent, whereas AFM data predicated a low percentage of voids 5 % and 9 % respectively. Both these techniques, AFM and SE confirm the drastic reduction of voids due to annealing. The measured thickness of the Cu thin film for as-deposited and annealed films are also listed in *table 3.4 and 3.5*. The film thickness increased with deposition time and there is hardly any effect of annealing on it. The value of oscillator energies for all the oscillators are listed in the *table 3.6 and 3.7*, for as-deposited and final post annealed film at 400°C respectively as a function of deposition time.

Table 3.6: *Oscillator energies for as-deposited films with deposition time.*

Deposition time (minutes)	E_{01} (eV)	E_{02} (eV)
4	4.82±0.08	3.44±0.03
6	5.12±0.35	3.56±0.04
8	4.80±0.18	3.52±0.01

Table 3.7*: Oscillator energies for post annealed films up to 400°C with deposition time.*

Deposition time (minutes)	E_{01} (eV)	E_{02} (eV)	E_{03} (eV)	E_{04} (eV)
4	5.69±1.09	1.85±0.12	1.32±0.02	3.43±0.11
6	2.89±0.29	1.70±0.01	2.28±0.08	1.98±0.01
8	0.80±0.40	1.63±0.01	2.32±0.02	1.98±0.01

The first oscillator energy (E_{o1}, Lorentz oscillator) for the as-deposited films for 4, 6 and 8 minutes duration is 4.82 eV, 5.12 eV and 4.80 eV respectively, corresponds to the interband transition peak [55, 56]. The second oscillator energy (E_{o2}, Gauss oscillator) of all these samples is within the range of 3.44 eV- 3.56 eV, corresponding to the SPR peak near UV region [57]. It was observed that the values of both the oscillator energies (E_{o1}, E_{o2}) was nearly constant (within error) with deposition time. The absorption spectra (*figure 3.9*) of the corresponding film also confirmed the existence of these oscillator peaks.

The annealing of the nanostructured Cu thin film could be responsible for coalescence and aggregation of the nanoparticles of Cu which result into a shift in the Fermi energy and splits it into the new energy levels [57-59]. This is confirmed by SE analysis for the annealed films. The first oscillator energy (E_{o1}, Lorentz oscillator) of the post annealed films for 4, 6 and 8 minutes duration, *table 3.7*, is in the range of 5.68 ± 1.09 eV - 0.80 ± 0.40 eV, corresponds to the interband transition peak. It showed the subtle shift towards the lower energy with an increase in the deposition time. The modification of the

interband energy level was due to the change in the size and shape of nanoparticles, agglomeration of Cu atom and formation of new Cu species (e.g. Cu (II)) [40, 57]. The second oscillator (E_{o2}, Gauss model) corresponds to the longitudinal mode of the SPR [60]. It is found to be in the range of 1.63 eV – 1.85 eV, shifted towards lower energy with an increase in the aspect ratio of the Cu nanoparticles, *table 3.2* [42]. The third oscillator (E_{o3}, Gauss model) of the post annealed film corresponds to another SPR peak (transverse mode) within the range of 1.32 to 2.32 eV which arises due to the non-spherical shape of the nanoparticles [60]. The forth oscillator energy (E_{o4}) for the 4 minutes deposited annealed film was 3.43 eV and that of for 6 and 8 minutes deposited film was 1.98 eV. The E_{04} peak energy (~3.43 eV) of the 4 minutes duration gradually annealed film signifies the second interband transition peak energy [41]. However, the E_{o4}, peak energy of the 6 and 8 minutes duration films are attributed to the oxide formation (11% in 6 minutes and 17% in 8 minutes, *table 3.5*) and is closed proximity of the band gap energy of Cu_2O which is reported to be around 2.1 – 2.4 eV [61]. On comparison with *table 3.2* and *table 3.7*, it can be concluded that some of the oscillator energies estimated from ellipsometer analysis is nearly matched with the absorption peak obtained from UV visible analysis.

Figure 3.13 shows the evolution of linear refractive index and excitation coefficient of the plasmonic copper thin film obtained from SE in the energy range of 1.2 eV to 4.0 eV. The copper nanostructured thin film exhibits higher refractive index compared to that of the bulk copper [62]. It was also observed that the refractive index of the gradually annealed nanostructured Cu thin films is more than that of the as-deposited films. It is due to the agglomeration, increase in the surface roughness which increases the scattering on the surface resulting in the higher refractive index. The spectra of the excitation coefficient extracted from the BEMA for as-deposited and gradually annealed films were nearly similar to that of the UV visible spectra (*figure 3.8*) further confirming that the applied

layer structured and BEMA is best for these type of PLD Cu nanostructured thin films.

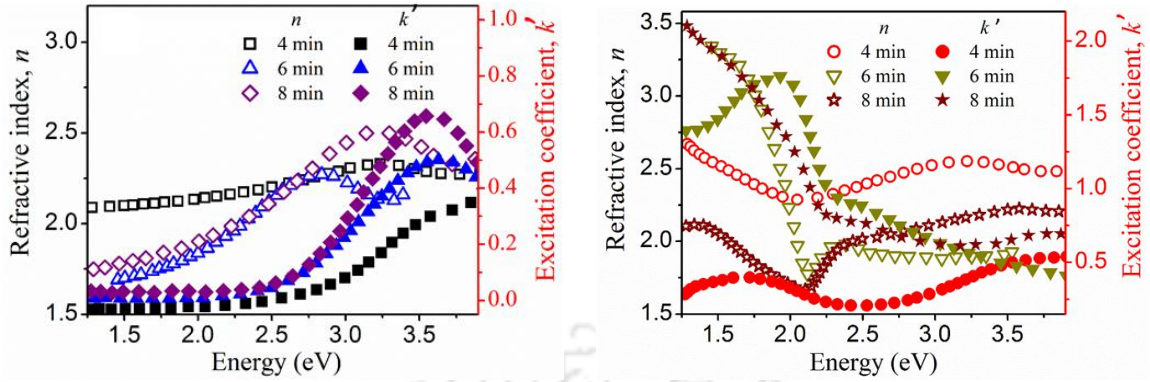

***Figure 3.13**: Refractive index and excitation coefficient of the PLD nanostructured Cu thin films as a function of photon energy (eV) for different deposition time (a) as-deposited and (b) post annealed.*

3.4.3 Estimation of the thickness of the top oxide layer and interfacial layer on the post annealed films of Cu

The formation of oxide layer on the top surface of the film and interface between glass and Cu NPs layer have been reported in the literature [63-65]. In this section the thickness of top oxide layer and interfacial layer is estimated from the SE data by applying the appropriate dispersion law along with the proper layer structure for the post annealed (finally at 400ºC) Cu thin films.

3.4.3.1 Layer structure considered for ellipsometric analysis using dispersion law

The five layers structure incorporated for semitransparent Cu thin film of the gradual annealed to a final temperature of 400 °C is shown in *figure 3.14*. The first dielectric layer is of glass substrate (coverslip) having a thickness of ~10^5 nm, which is very large compared to that of the Cu film under investigation. The second layer above the substrate comprises of Cu_2O interface which is formed due to the formation of bonds between free copper ions (deposited by laser) and oxygen molecule residing at the interface

of the glass substrate (except 4 minutes). The third layer is the main copper nanoparticles (Cu NPs) layer on which an appropriate dispersion law is to be applied. The fourth layer is of the Cu (II) which is diatomic Cu atom formed due to the annealing of the Cu nanoparticles. Finally, the top fifth layer is of the oxide (CuO/ Cu_2O) which is formed due to the contamination of copper surface in the presence of open atmosphere. The space above the top layer and below the substrate (first layer) is void.

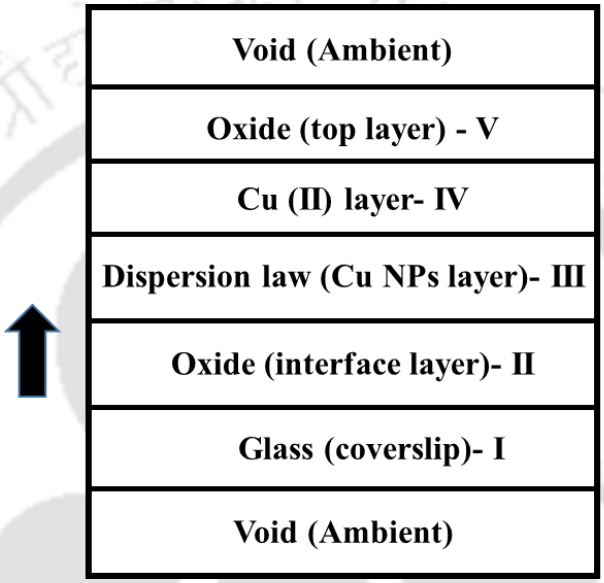

***Figure 3.14**: Schematic of the assumed layer structure for ellipsometric analysis using dispersion law.*

3.4.4.2 Effect of deposition time on the top oxide layer and interfacial layer of the post annealed nanostructured PLD Cu thin film

The dispersion law applied here is also a combination of one Lorentz and three Gauss (L-G) model, *equation 3.8*, *section 3.4*. It is observed that the single Drude model or single Lorentz model or combination of the Drude-Lorentz- Gauss model for the present Cu thin film is not appropriate because after regression these gave large RMSE values. On the other hand, the L-G dispersion model is found to be more appropriate (minimum RMSE) for present Cu thin film. *Figure 3.15* shows the experimentally estimated values of

ellipsometric parameters; $tan\psi$ and $cos\Delta$ and those of fitted ones, using L-G oscillator dispersion law, *equation 3.*8 for the layer structure of *figure 3.14*. The thickness of each layer with the deposition time estimated from these analyses is listed in *table 3.8*. It is observed that overall the thickness of the film and that of the Cu NP layer and Cu (II) layer increases with the deposition time.

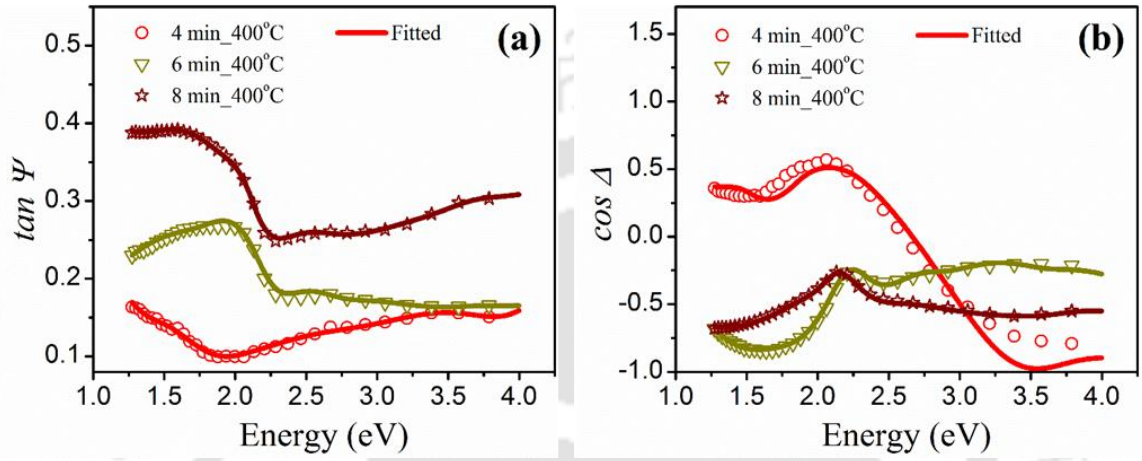

Figure 3.15*: The experimental and fitted of PLD nanostructured post annealed Cu thin film as the function of energy for the layer structure illustrated in figure 3.14 (a) tanψ and (b) cosΔ.*

For 4 minutes duration film, the interfacial layer is missing while for 6 and 8 minutes duration film, the thickness of interfacial layer is ~1.7 and 5.0 nm respectively indicating the diffusion of the particles towards the substrate. This is agreement by fractal analysis (*section 3.2.2*). For 4 minutes duration film, a Cu (II) layer mixed with the void is observed while in the remaining two samples the void is absent. The similar observation was also found in the BEMA analysis of the respective films (*section 3.4.2*) as well as that of the AFM result (*section 3.2.1*). The energy of all the four oscillators (*equation 3.8*) obtained in this case is listed in *table 3.9*. The constituent species of the Cu and its oscillator energies, estimated from the BEMA analysis, *table 3.7*, nearly matches with the dispersion model coupled to five layer structure.

***Table 3.8**: Top oxide, Cu species and interfacial layer thicknesses of post annealed films with deposition time measured via ellipsometry.*

Deposition time (min.)	Overall thickness of film (nm)	Cu NPs layer thickness (nm)	Cu (II) layer thickness (nm)	Top oxide layer thickness (nm)	Interface thickness (nm)
4	12.60±0.002	6.67±0.03	1.36±0.03 (mix. with void)	4.59±0.03 (CuO)	---
6	18.70±0.001	13.0±0.10	2.7±0.03	1.3±0.03 (Cu_2O)	1.7±0.01
8	29.09±0.032	14.7±0.10	5.7±0.01	3.6±0.03 (Cu_2O)	5.0±0.01

***Table 3.9**: Fitting parameter of all the four oscillator energies of post annealed films to a final temperature of 400°C with deposition time using dispersion model.*

Deposition time (minutes)	E_{01} (eV)	E_{02} (eV)	E_{03} (eV)	E_{04} (eV)
4	6.67 ±1.83	1.86 ±1.20	1.32 ±0.80	3.59 ±0.07
6	2.90 ±0.29	2.48 ±0.01	1.58 ±0.06	1.96 ±0.01
8	0.647 ±0.11	2.51 ±0.03	1.49 ±0.06	1.99 ±0.01

However, the recorded ellipsometer parameters (*tan ψ* and *cos Δ*) fit well for earlier assumed layer structure (*figure 3.12*), compared to that of present layer structure of five layers (*figure 3.15*). Hence, for the study of plasmonic properties and stoichiometry of the as-deposited and post gradual annealed films, the BEMA model is more appropriate but one has to apply the metallic layer structure in order to assess the interfacial layer which influence the plasmonic properties.

3.5 Conclusions

It was observed that the none of the as-deposited (at RT) films exhibited SPR peak while finally post annealed to 400°C, showed both LM and TM SPR peaks. From the PSDF analysis, it was found that after annealing, the film surface (fractal nature) and Fermi level of the Cu nanoparticles have undergone a change apart from the size and shape of the nanoparticles. The SE analysis further confirmed the changes in the properties of deposited Cu nanoparticles and stoichiometry after annealing. It was observed that the as-deposited RT films fit well with the two oscillators (one Lorentz and one Gauss) model whereas the annealed films followed the four oscillators dispersion (one Lorentz and three Gauss) model. In the present case, the properties of the films were best described by only BEMA model. In the BEMA analysis, it was found that for as-deposited film, the percentage of void was large and was decreased with increasing the deposition time. In the case of annealed film, the percentage of void was negligible (expect 4 minutes film) but the other new copper species (Cu (II) and oxides) were evolved which influence the SPR properties of plasmonic Cu film.

Bibliography

[1] N. Kaiser, Review of the fundamentals of thin-film growth, Applied optics, 41 (2002) 3053-3060.

[2] Ș. Țălu, R.P. Yadav, A.K. Mittal, A. Achour, C. Luna, M. Mardani, S. Solaymani, A. Arman, F. Hafezi, A. Ahmadpourian, Application of Mie theory and fractal models to determine the optical and surface roughness of Ag–Cu thin films, Optical and Quantum Electronics, 49 (2017) 256.

[3] E.Y. Poliakov, V.A. Markel, V.M. Shalaev, R. Botet, Nonlinear optical phenomena on rough surfaces of metal thin films, Physical Review B, 57 (1998) 14901-14913.

[4] V.M. Shalaev, V.A. Markel, E.Y. Poliakov, R.L. Armstrong, V.P. Safonov, A.K. Sarychev, Nonlinear optical phenomena in nanostructured fractal materials, Journal of Nonlinear Optical Physics & Materials, 7 (1998) 131-152.

[5] S. Basavaiah, S.R. Pollack, Superconductivity in evaporated tungsten films, Applied Physics Letters, 12 (1968) 259-260.

[6] J. Su, Y. Liu, M. Jiang, X. Zhu, Oxidation of copper during physical sputtering deposition: mechanism, avoidance and utilization, arXiv preprint arXiv:1412.2031, (2014).

[7] A.T.T. Mostako, A. Khare, Note: Large area deposition of Rh single and Rh/W/Cu multilayer thin films on stainless steel substrate by pulsed laser deposition technique, Review of Scientific Instruments, 85 (2014) 046101.

[8] M. Zinke-Allmang, L.C. Feldman, M.H. Grabow, Clustering on surfaces, Surface Science Reports, 16 (1992) 377-463.

[9] K. Reichelt, Nucleation and growth of thin films, Vacuum, 38 (1988) 1083-1099.

[10] R. Vook, F. Witt, Structure and annealing behavior of metal films deposited on substrates near 80 K: I. copper films on glass, Journal of Vacuum Science and Technology, 2 (1965) 49-57.

[11] T. Karakouz, A.B. Tesler, T. Sannomiya, Y. Feldman, A. Vaskevich, I. Rubinstein, Mechanism of morphology transformation during annealing of nanostructured gold films on glass, Physical Chemistry Chemical Physics, 15 (2013) 4656-4665.

[12] J. Quan, J. Zhang, X. Qi, J. Li, N. Wang, Y. Zhu, A study on the correlation between the dewetting temperature of Ag film and SERS intensity, Scientific reports, 7 (2017) 14771.

[13] C. Guillon, P. Langot, N. Del Fatti, F. Vallée, Nonequilibrium electron energy-loss kinetics in metal clusters, New Journal of Physics, 5 (2003) 13.

[14] E. Ozbay, Plasmonics: merging photonics and electronics at nanoscale dimensions, science, 311 (2006) 189-193.

[15] R. Zia, J.A. Schuller, A. Chandran, M.L. Brongersma, Plasmonics: the next chip-scale technology, Materials today, 9 (2006) 20-27.

[16] C. Zhao, J. Zhang, Binary plasmonics: launching surface plasmon polaritons to a desired pattern, Optics letters, 34 (2009) 2417-2419.

[17] A.B. Kaul, Microelectronics to Nanoelectronics: Materials, Devices & Manufacturability, CRC Press, 2017.

[18] V. Passaro, C.d. Tullio, B. Troia, M.L. Notte, G. Giannoccaro, F.D. Leonardis, Recent advances in integrated photonic sensors, Sensors, 12 (2012) 15558-15598.

[19] V.E. Ferry, L.A. Sweatlock, D. Pacifici, H.A. Atwater, Plasmonic nanostructure design for efficient light coupling into solar cells, Nano letters, 8 (2008) 4391-4397.

[20] C. Chang, C. Wei, S. Chen, Self-diffusion of small clusters on fcc metal (111) surfaces, Physical review letters, 85 (2000) 1044.

[21] S. Du, Y. Li, Effect of annealing on microstructure and mechanical properties of magnetron sputtered Cu thin films, Advances in Materials Science and Engineering, 2015 (2015).

[22] H.S. Hilal, R.M. Ismail, A. El-Hamouz, A. Zyoud, I. Saadeddin, Effect of cooling rate of pre-annealed CdS thin film electrodes prepared by chemical bath deposition: Enhancement of photoelectrochemical characteristics, Electrochimica Acta, 54 (2009) 3433-3440.

[23] M. Gao, J. Liu, H. Sun, X. Wu, D. Xue, Influence of cooling rate on optical properties and electrical properties of nanorod ZnO films, Journal of Alloys and Compounds, 500 (2010) 181-184.

[24] S. Karan, B. Mallik, Power spectral density analysis and photoconducting behavior in copper (ii) phthalocyanine nanostructured thin films, Physical Chemistry Chemical Physics, 10 (2008) 6751-6761.

[25] D. Aurongzeb, Growth instability and surface phase transition of Ti thin film on Si (1 1 1): An atomic force microscopy study, Applied surface science, 252 (2006) 6135-6140.

[26] M. Senthilkumar, N. Sahoo, S. Thakur, R. Tokas, Characterization of microroughness parameters in gadolinium oxide thin films: A study based on extended power spectral density analyses, Applied Surface Science, 252 (2005) 1608-1619.

[27] M. Pelliccione, T.-M. Lu, Evolution of thin film morphology, Springer, 2008.

[28] S.M. Obaidulla, P. Giri, Surface roughening and scaling behavior of vacuum-deposited SnCl2Pc organic thin films on different substrates, Applied Physics Letters, 107 (2015) 221910.

[29] D. Nečas, P. Klapetek, Gwyddion: an open-source software for SPM data analysis, Open Physics, 10 (2012) 181-188.

[30] E.L. Church, Fractal surface finish, Applied Optics, 27 (1988) 1518-1526.

[31] T. Yoshinobu, A. Iwamoto, H. Iwasaki, Scaling analysis of SiO2/Si interface roughness by atomic force microscopy, Japanese journal of applied physics, 33 (1994) 383.

[32] M. Berry, J. Hannay, Topography of random surfaces, Nature, 273 (1978) 573.

[33] T. Xu, I.D. Moore, J.C. Gallant, Fractals, fractal dimensions and landscapes—a review, Geomorphology, 8 (1993) 245-262.

[34] G. Rasigni, F. Varnier, M. Rasigni, J. Palmari, A. Llebaria, Roughness spectrum and surface plasmons for surfaces of silver, copper, gold, and magnesium deposits, Physical Review B, 27 (1983) 819.

[35] M. Nasehnejad, G. Nabiyouni, M.G. Shahraki, Thin film growth by 3D multi-particle diffusion limited aggregation model: Anomalous roughening and fractal analysis, Physica A: Statistical Mechanics and its Applications, 493 (2018) 135-147.

[36] Y. Mo, J. Kleiner, M. Webb, M. Lagally, Activation energy for surface diffusion of Si on Si (001): A scanning-tunneling-microscopy study, Physical review letters, 66 (1991) 1998.

[37] L.E. Revell, B.E. Williamson, Why are some reactions slower at higher temperatures?, Journal of chemical education, 90 (2013) 1024-1027.

[38] J. Orosco, C. Coimbra, On a causal dispersion model for the optical properties of metals, Applied Optics, 57 (2018) 5333-5347.

[39] T. Buys, K. De Clerk, Bi-Gaussian fitting of skewed peaks, Analytical Chemistry, 44 (1972) 1273-1275.

[40] K.C. Mishra, A. Piquette, P.C. Schmidt, K.H. Johnson, Electronic structures and optical properties of Al, Cu, and Ag in zero, two, and three dimensional structures, Journal of Applied Physics, 122 (2017) 063104.

[41] R. Rosei, D.W. Lynch, Thermomodulation spectra of al, au, and cu, Physical Review B, 5 (1972) 3883.

[42] C. Noguez, Surface plasmons on metal nanoparticles: the influence of shape and physical environment, The Journal of Physical Chemistry C, 111 (2007) 3806-3819.

[43] C. Lucena-Serrano, R. Contreras-Caceres, M. Sánchez-Molina, M.A. Casado-Rodriguez, J.M. Cloarec, E. Mainetti, M. Lopez-Romero, Preparation and Application of Non-spherical Metal Nanoparticles: Reality and Perspective, Current Organic Chemistry, 21 (2017) 2338-2359.

[44] V.M. Shalaev, R. Botet, J. Mercer, E.B. Stechel, Optical properties of self-affine thin films, Physical Review B, 54 (1996) 8235.

[45] D. Garoli, E. Calandrini, A. Bozzola, A. Toma, S. Cattarin, M. Ortolani, F. De Angelis, Fractal-like plasmonic self-similar material with a tailorable plasma frequency in the near-infrared, arXiv preprint arXiv:1803.08074, (2018).

[46] G.A. Niklasson, C. Granqvist, O. Hunderi, Effective medium models for the optical properties of inhomogeneous materials, Applied Optics, 20 (1981) 26-30.

[47] H. Fujiwara, Spectroscopic ellipsometry: principles and applications, John Wiley & Sons, 2007.

[48] E.D. Palik, Handbook of optical constants of solids II, Academic press, (1985).

[49] D.D.S. Meneses, M. Malki, P. Echegut, Structure and lattice dynamics of binary lead silicate glasses investigated by infrared spectroscopy, Journal of non-crystalline solids, 352 (2006) 769-776.

[50] H. Bakkali, E. Blanco, M. Dominguez, M. de la Mora, C. Sánchez-Aké, M. Villagrán-Muniz, Optical properties of Au–TiO 2 and Au–SiO 2 granular metal thin films studied by Spectroscopic Ellipsometry, Applied Surface Science, 405 (2017) 240-246.

[51] S.A. Maier, Plasmonics: fundamentals and applications, Springer Science & Business Media, 2007.

[52] A. Serrano, O. Rodriguez De La Fuente, M. García, Extended and localized surface plasmons in annealed Au films on glass substrates, Journal of Applied Physics, 108 (2010) 074303.

[53] W. He, J. Cai, X. Jiang, J. Yin, Q. Meng, Generation of Reactive Oxygen Species and Charge Carriers in Plasmonic Photocatalytic Au@ TiO2 Nanostructures with Enhanced Activity, Physical Chemistry Chemical Physics, (2018).

[54] I. Doron-Mor, Z. Barkay, N. Filip-Granit, A. Vaskevich, I. Rubinstein, Ultrathin gold island films on silanized glass. Morphology and optical properties, Chemistry of Materials, 16 (2004) 3476-3483.

[55] P.B. Johnson, R.-W. Christy, Optical constants of the noble metals, Physical review B, 6 (1972) 4370.

[56] K. Chee, F.E. Girouard, V.-V. Truong, Interband transitions in aggregated copper films, Applied optics, 20 (1981) 404-406.

[57] B. Balamurugan, T. Maruyama, Size-modified d bands and associated interband absorption of Ag nanoparticles, Journal of applied physics, 102 (2007) 034306.

[58] P.E. Hopkins, J.C. Duda, R.N. Salaway, J.L. Smoyer, P.M. Norris, Effects of intra- and interband transitions on electron-phonon coupling and electron heat capacity after short-pulsed laser heating, Nanoscale and Microscale Thermophysical Engineering, 12 (2008) 320-333.

[59] P. Peljo, J.A. Manzanares, H.H. Girault, Contact potentials, fermi level equilibration, and surface charging, Langmuir, 32 (2016) 5765-5775.

[60] S. Link, M.A. El-Sayed, Shape and size dependence of radiative, non-radiative and photothermal properties of gold nanocrystals, International reviews in physical chemistry, 19 (2000) 409-453.

[61] B. Meyer, A. Polity, D. Reppin, M. Becker, P. Hering, P. Klar, T. Sander, C. Reindl, J. Benz, M. Eickhoff, Binary copper oxide semiconductors: From materials towards devices, physica status solidi (b), 249 (2012) 1487-1509.

[62] H. Savaloni, F. Babaei, S. Song, F. Placido, Influence of substrate rotation speed on the nanostructure of sculptured Cu thin films, Vacuum, 85 (2011) 776-781.

[63] M. He, T.-M. Lu, Metal-dielectric interfaces in gigascale electronics: thermal and electrical stability, Springer Science & Business Media, 2012.

[64] I. Platzman, R. Brener, H. Haick, R. Tannenbaum, Oxidation of Polycrystalline Copper Thin Films at Ambient Conditions, The Journal of Physical Chemistry C, 112 (2008) 1101-1108.

[65] M. Rauh, P. Wiβmann, M. Wölfel, Ellipsometric studies on the oxidation of thin copper films, Thin solid films, 233 (1993) 289-292.

Chapter 4

Effect of deposition time on interfacial layer, optical and SPR properties and scaling behaviour of PLD semi-transparent nanostructured Cu thin films deposited at 400°C

In the previous chapter 3, it was observed that room temperature (RT) films annealed finally at the glass softening temperature of 400°C exhibited the improved plasmonic properties. Therefore a natural next step is to test the properties of pulsed laser deposition (PLD) Cu film directly deposited at 400°C.

In the present chapter, the nanostructured semi-transparent Cu thin films grown onto glass substrate via PLD technique directly at a substrate temperature of 400°C, as a function of deposition time are presented. The particle size distribution and growth dynamics of these films via height-height correlation function (HHCF) and power spectral density function (PSDF) were obtained from AFM images. The absorption spectra were recorded for detecting the surface plasmon resonance (SPR) signal. The films were subjected to spectroscopy ellipsometer (SE) for the assessment of refractive index, excitation coefficient, thickness of film, interfacial layer and top oxide layer and their structure.

4.1 Experimental details

Semi-transparent metallic Cu thin films were grown onto glass (coverslip) substrate using PLD technique detailed in *Section 2.1, Chapter 2*. The second harmonic of a Q-switched Nd:YAG laser (pulse duration - 10 ns and repetition rate - 10 Hz), at a laser

fluence of ~ 4 J/cm^2 was focused onto the Cu target under vacuum (~ 10^{-6} mbar). The films were deposited for 6, 7, 8, 9, 10, 20, 30 and 45 minutes duration at a substrate temperature of 400 ºC. After the deposition, all the films were annealed at 400 °C under vacuum for 120 minutes in order to remove any strain developed during deposition. These annealed thin films were subjected to X-ray diffractometer operated at a wavelength of 1.5407 Å of Cu K_α line for measurement at a glancing incidence angle, $\omega = 1°$ and the scanning range (2θ) was 20° - 70° with an angular step of 0.02°. In order to study the surface morphology, size and shape of nanoparticles, the dynamic scaling behaviour and growth mechanism of Cu films fabricated via PLD technique**,** all the films were subjected to AFM measurement. The absorbance of the films was measured directly from UV-visible spectrometer for identifying the plasmonic peak and correlated with the scaling parameters. The optical properties, interfacial layer thickness and its oxide phase, were examined via variable angle SE.

4.2 Structural properties of PLD nanostructured Cu thin films

The XRD spectra of PLD nanostructured Cu thin films deposited on the glass substrate at a temperature of 400°C for various deposition time from 6 to 45 minutes are shown in *figure 4.1*. The XRD peaks observed at 43.33° and 50.29° correspond to the Cu (111) and Cu (220) planes, respectively with former being more intense [1]. *Figure 4.1* clearly shows the increase in the intensity of both these peaks with the deposition time which is due to the increase in thickness thus facilitating the participation of larger number of diffracting planes. The crystallite size was estimated from the full width half maxima (FWHM) of the most intense peak of (111) plane by Debye Scherrer's formula [2]. The *figure 4.2* shows the nearly linear increase in the size of Cu crystallites from 3.2 nm to 30.3 nm with increasing deposition time from 6 to 45 minutes respectively.

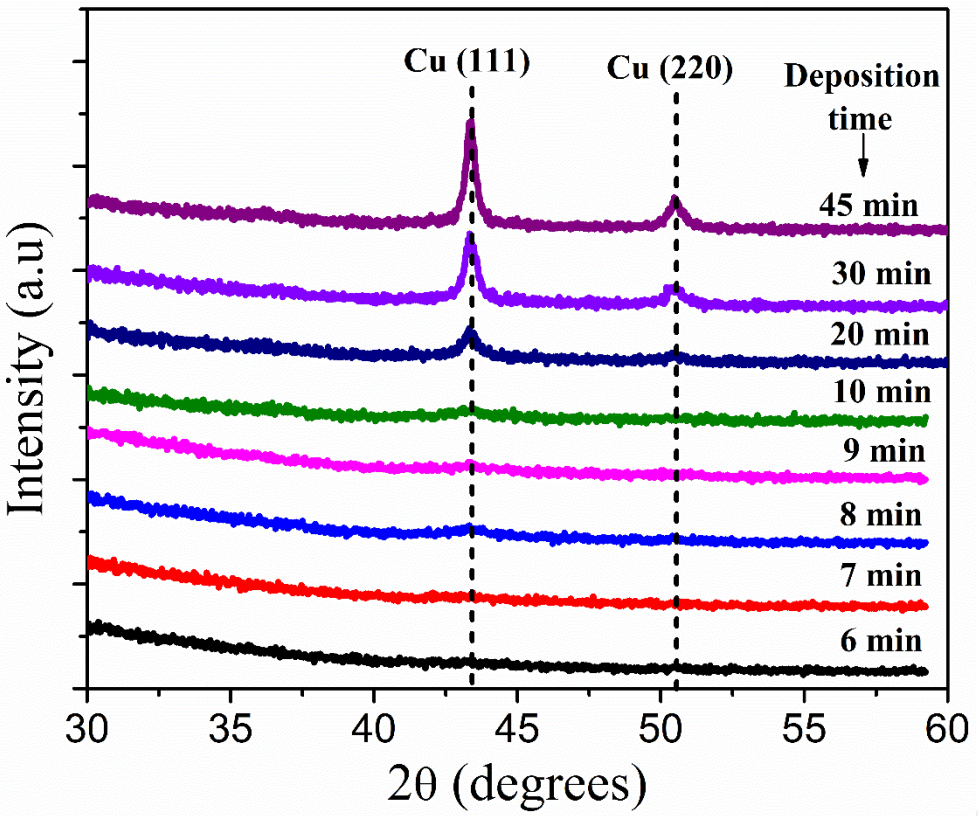

***Figure 4.1**: XRD spectra of PLD Cu thin films deposited on glass substrate for deposition time, 6 -45 minutes.*

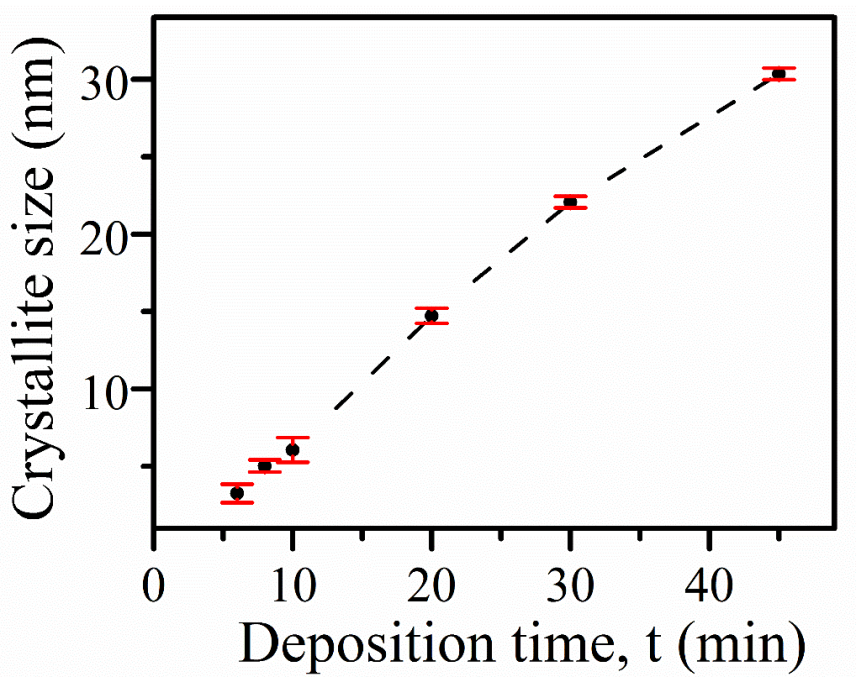

***Figure 4.2**: The variation of crystallite size with deposition time.*

4.3 Surface morphology and dynamics scaling behaviour of PLD Cu thin films from AFM images

The surface morphology of the films was characterized by AFM to unveil the surface microstructures and its growth dynamics [3]. *Figure 4.3 (a-h)* shows the AFM images (scan area 2μm × 2 μm) of all the films for the deposition time of 6 - 45 minutes, respectively. The initial visualization of AFM images indicates the uniform distribution of grains over the film surface. Initially, for the lower deposition time, the grains were observed to be of spherical in shape. With increasing deposition time or growth time, the repeated impinging of particle flux from incoming laser induced plasma towards the substrate, the nucleation sites increased followed by coalescence of smaller size grains to form bigger particles along with the formation of columnar structure shown in *figure 4.3 (i)* for the film deposited for 45 minutes duration. Eventually, at 30 and 45 minutes duration, relatively large sized and densely packed grains were formed as is evident from *figure 4.3 (g) and 4.3 (h)* respectively. The estimated size of the nanoparticles was ranging from ~14 to ~123 nm for the deposition time of 6 to 45 minutes respectively. The particle size distribution was estimated from 2D AFM images using open excess image J software. The estimated particle size (or lateral size) was averaged over three different locations on the surface of each film and is shown in *figure 4.4 (a - h)*. The variation of the average particle size as a function of deposition time of PLD Cu film is shown in *figure 4.4 (i).* To unveil the growth process and the dynamic scaling behaviour, the scaling exponents**;** root mean square (RMS) roughness or interface width (w) and local slope (m) of the islands were calculated from AFM images. These quantities were obtained from HHCF, $H(\boldsymbol{r}, t)$. It is defined by the statistical average of the mean square of height difference between the pair of points, separated by $\boldsymbol{r}$ and is written as [3]:

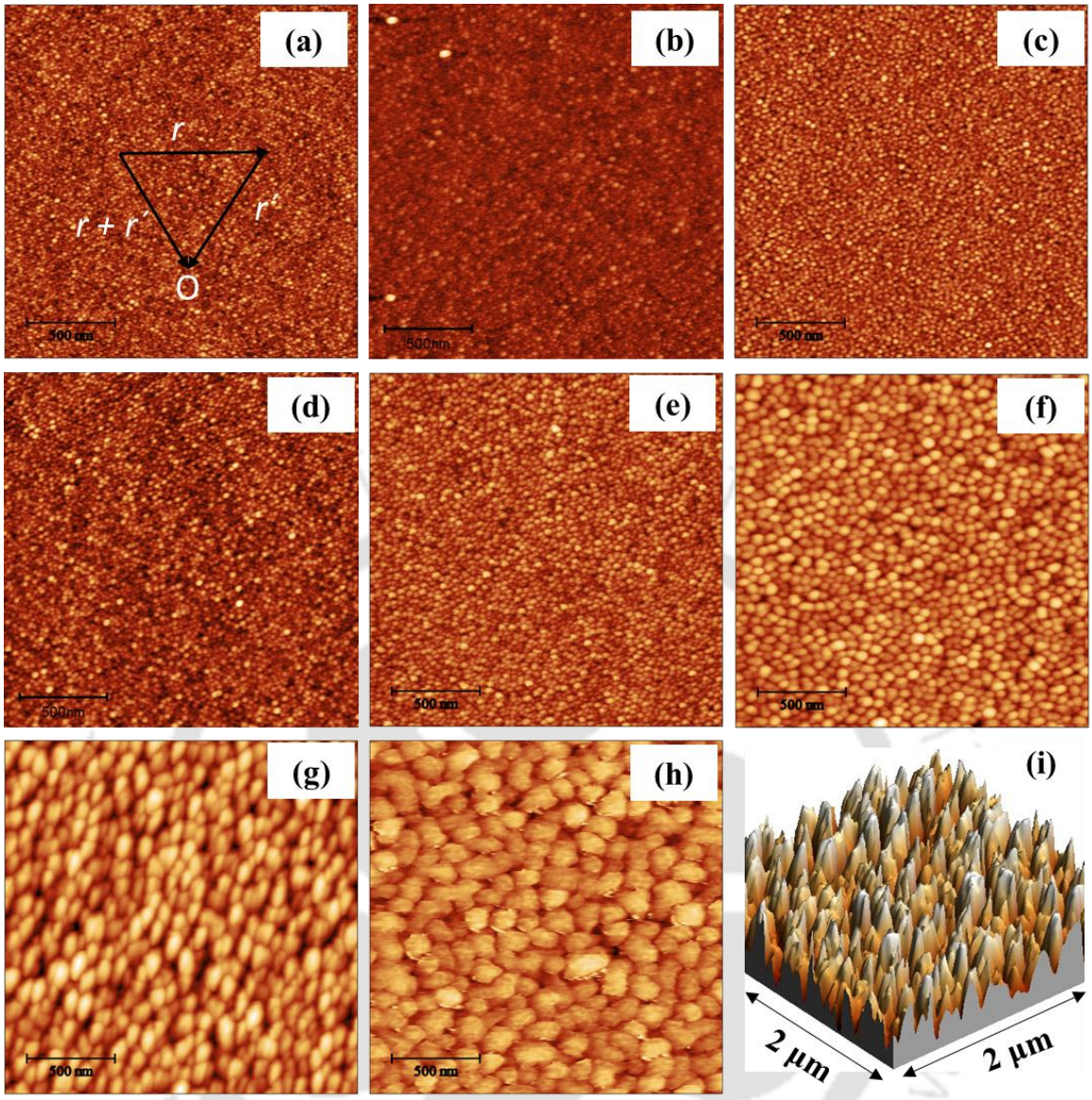

***Figure 4.3**: AFM images of PLD Cu films for the deposition time of (a) 6 minutes, (b) 7 minutes, (c) 8 minutes, (d) 9 minutes, (e) 10 minutes, (f) 20 minutes, (g) 30 minutes, (h) 45 minutes and (i) 3-D image of Cu thin film deposited for a duration of 45 minutes.*

$$H(\boldsymbol{r},t) = \langle |h(\boldsymbol{r}+\boldsymbol{r}',t) - h(\boldsymbol{r}',t)|^2 \rangle \qquad (4.1)$$

where $h(\boldsymbol{r}',t)$ is the surface height at a point $\boldsymbol{r}'$ and that of $h(\boldsymbol{r}+\boldsymbol{r}')$ at $(\boldsymbol{r}+\boldsymbol{r}')$, as marked in *figure 4.3 (a)* as an example. From the AFM images HHCF was directly evaluated by averaging over three distinct regions of large extent, much larger than r in order to avoid edge effects.

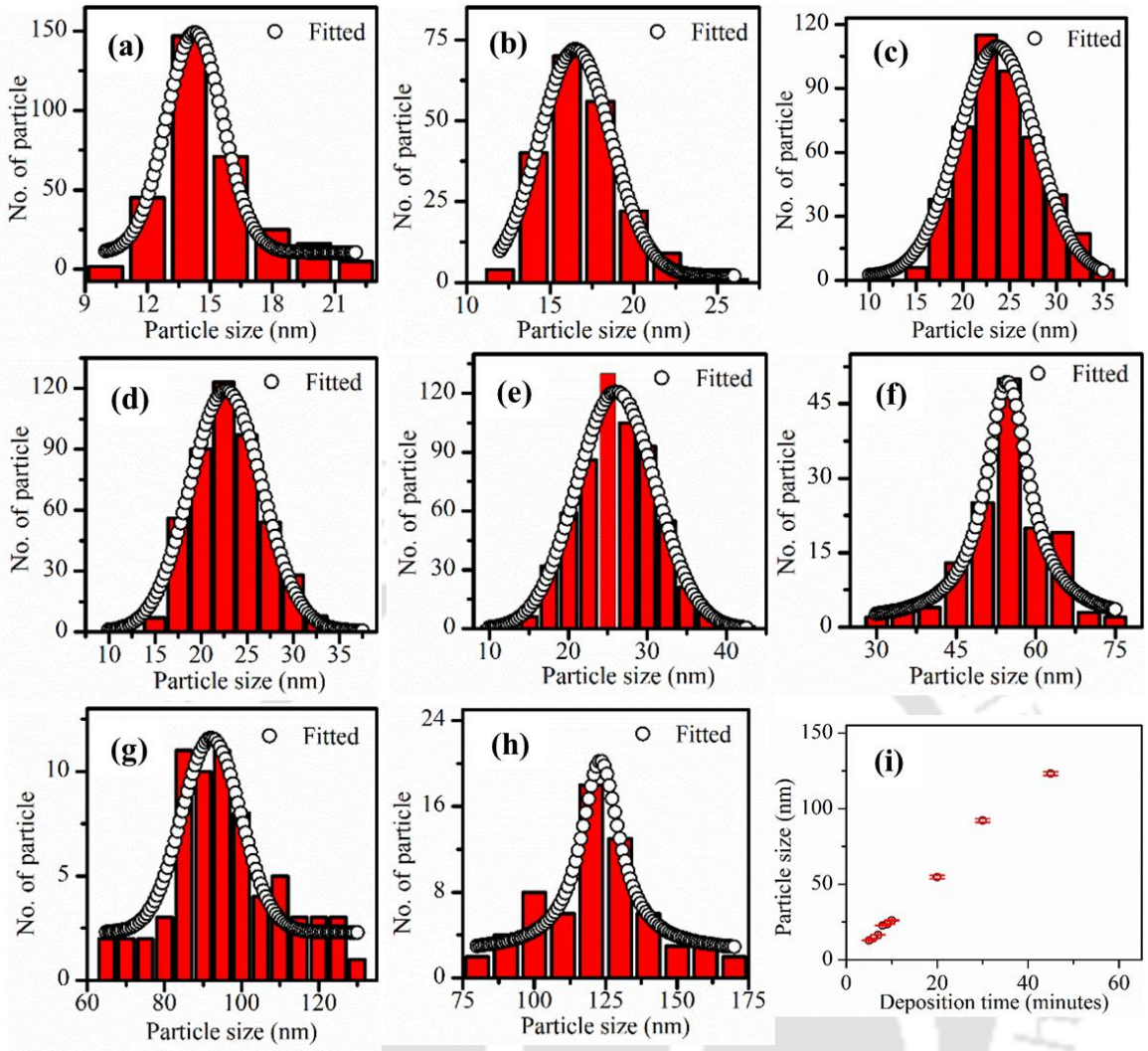

***Figure 4.4**: Particle size distribution of PLD nanostructured Cu thin films deposited at 400 °C for (a) 6 minutes, (b) 7 minutes, (c) 8 minutes, (d) 9 minutes, (e) 10 minutes, (f) 20 minutes, (g) 30 minutes, (h) 45 minutes and (i) variation of average particle size as a function of deposition time.*

The HHCF, can also be defined by exponential correlation model, which satisfies the requirement for self-affine surface and manifests anisotropic scale invariance, given by [4]

$$H(r) = 2w^2\left[1 - exp\left[-\left(\frac{r}{\xi}\right)^{2\alpha'}\right]\right] \qquad (4.2)$$

For r << ξ, from equation (*4.1*)

$$H\ (r < \xi) = 2w^2 \left(\frac{r}{\xi}\right)^{2\alpha'} \tag{4.3}$$

and for r >> ξ,

$$H\ (r \gg \xi) = 2w^2 \tag{4.4}$$

where w is the interface width, α' is the local roughness scaling exponent, and ξ is the lateral correlation length.

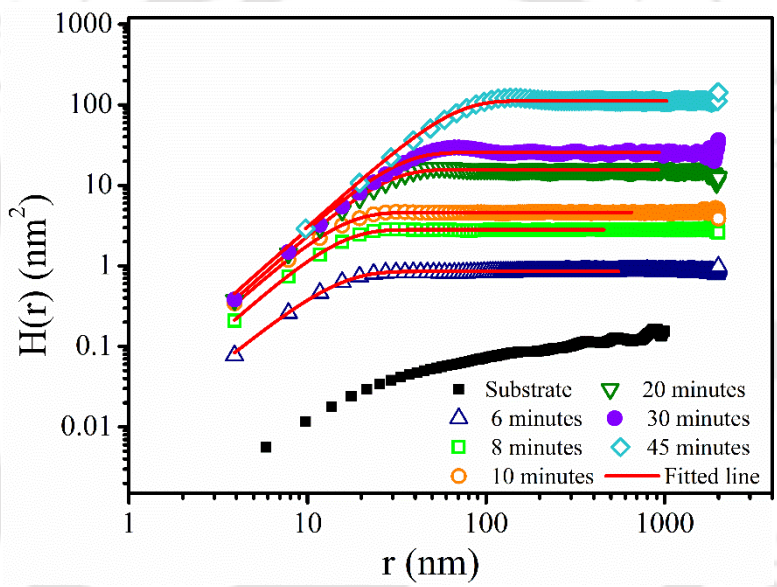

Figure 4.5*: Log-Log plot of HHCF, H(r, t) as a function of distance* ***r*** *fitted to eq. (4.2) for Cu thin films on glass substrate for deposition times of 6-45 minutes along with bare substrate.*

The Log-Log plot of $H(\boldsymbol{r}, t)$, obtained from AFM images, as a function of distance '***r***' along with curve fitted to *equation (4.2)* for all the films deposited for various interval of time (t) is shown in *figure 4.5*. The measured value fits well to *equation (4.2)* ($R^2 > 0.97$). The HHCF can be clearly divided into two distinct regions of $r << \xi$ and $r >> \xi$. For longer deposition time of 20, 30 and 45 minutes, an oscillatory behavior was observed for $r > > \xi$

indicating the formation of the mounded surface [4]. It is clear from *figure 4.5* that the value of $H(\boldsymbol{r}, t)$increases as Cu film thickness increases (with increasing growth time), indicating the increase in the RMS roughness. From the best fitting of experimental HHCF curves using *equations (4.2)*, w, ξ as well as α' were determined for each film. The variation of w, ξ and α' as a function of deposition time on the log-log scale is shown in *figure 4.6 (a), (b)* and *(c)* respectively. *Figure 4.6 (a)* shows the increase in the value of w from 0.65 to 7.48 nm for the films grown from 6 to 45 minutes respectively further confirming the increase in roughness of the film with the increasing growth time '*t*'. The increasing nature of ξ with *t*, as shown in *figure 4.6 (b)*, indicates the lateral growth of the islands. The lateral growth could be attributed to the increased in crystallite size (*figure. 4.2*) with increasing deposition time. The parameters w and ξ showed power law dependence as $w \sim t^{\beta'}$ and $\xi \sim t^{1/z'}$ respectively having values of β' = 1.07±0.11and z' =1.42±0.21. *Figure 4.6 (c)* predicts that there is a slight decrease in the value of α' from 0.88 for 6 minutes deposited film to 0.86 for that of 10 minutes and beyond this it increases to 0.95 for 20 minutes and thereafter the changes are insignificant. This affirms that the local roughness decreases while the RMS roughness/interface width (defined by *w*) increases with increasing deposition time (film thickness). In order to quantify the dynamics of the roughness, ξ versus *w* for all the samples were plotted (on log-log scale) and shown in *figure 4.7 (a)*. The relation between *w* and ξ can be worked out as $w \sim \xi^{\gamma}$, where the value of exponent, γ, was found to be 1.50 ± 0.54 comparable to that obtained from the values of β' and $1/z'$ ($\gamma = z'\beta'$). The value of γ can predict the competition between lateral and vertical growth. The observed value of $\gamma > 1$ indicates the faster vertical growth compared to lateral growth and is also related to the roughness of the film surface. In order to identify the mode of the growth, local slope $\left(m \sim \frac{w^{1/\alpha'}}{\xi}\right)$ as a function of deposition time was plotted and is

shown in *figure 4.7 (b)*. The dependence of *m* on time indicates the non-stationary growth in the present case. The upward shift of the $H(r)$with deposition time, *figure 4.5*, further signifies the non-stationary growth of the film [4, 5].

In the PLD process (near substrate softening temperature), the particle flux from laser produced plasma impinging on the substrate was of diverging nature having non-uniform distribution of particles.

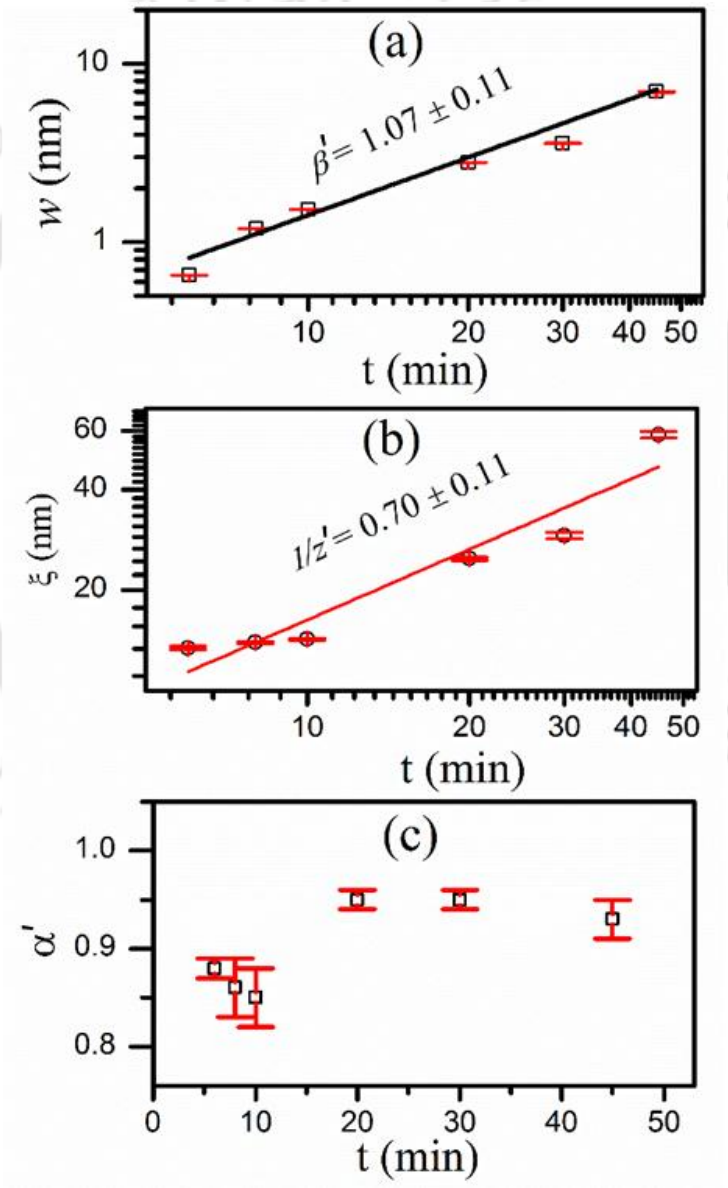

Figure 4.6*: Variation in (a) surface roughness w, (b) correlation length ξ, and (c) roughness exponent α′ with the deposition duration, t.*

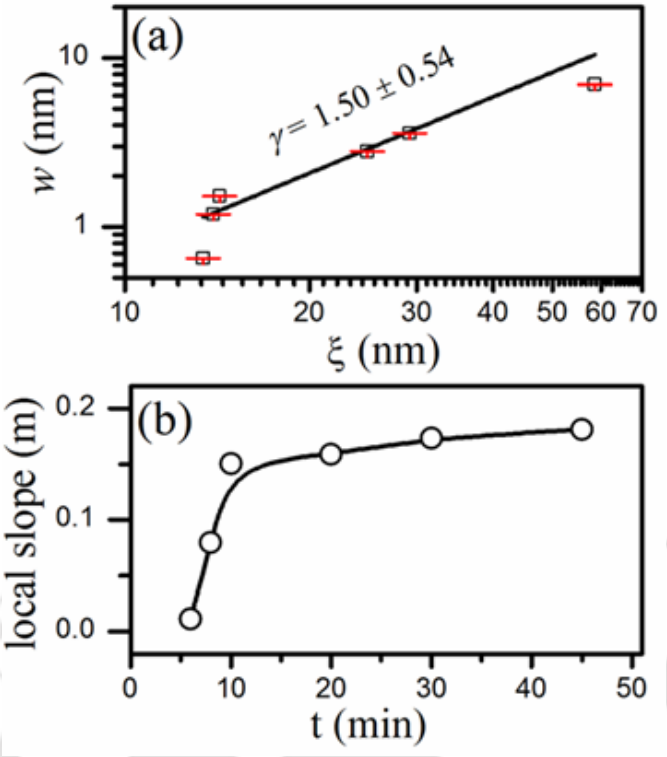

Figure 4.7*: Plot of (a) w versus ξ and (b) local slope m as a function of deposition time, t.*

Thus the growth process is dominated by shadowing effect apart from non-equilibrium growth. Another unique feature of this technique is the large kinetic energy of the particles striking the substrate, and so the deposition can be performed at relatively low substrate temperature with minimal re-emission [6]. Thus, the growth model best suited for the PLD films was that of proposed by Drotar *et al*. in which the surface under shadowing (roughening effect) and zeroth-order sticking coefficient corresponding to minimal reemission (s_0=1 and s_n=0 for n>0) were considered. It is described by stochastic continuum growth equation [6],

$$\frac{\partial h}{\partial t} = v\nabla^2 h(r,t) - k\nabla^4 h(r,t) + s_0 F_0(r,t)\sqrt{1+|\nabla h|^2} + \eta(r,t)), \qquad (4.6)$$

The first term on the right-hand side ($v\nabla^2 h$) represents the evaporation dynamics where surface relaxation was achieved by annealing mechanism, the second term ($k\nabla^4 h$) accounts for smoothening by surface diffusion due to the curvature-induced chemical

potential gradient, in the third term F_0 contains information about the shadowing effect, as well as the nature of the incoming particle flux given by $F_0 = \int_0^{2\pi}\int_0^{\theta_{max}} R(\theta,\Phi)[sin\theta(\hat{i}cos\Phi + \hat{j}sin\Phi) + \hat{j}cos\theta].\hat{n}(r)(sin\theta)d\theta d\Phi$, where θ is the local polar angle, Φ is the local azimuthal angle and R(θ ,Φ) is the distribution of the incoming flux and $\hat{n}$ is the unit vector normal to the substrate. The factor $\sqrt{1+|\nabla h|^2}$ in the third term represents growth normal to the local surface and the last term in *equation (4.6)*, $\eta(r,t)$, is the noise in the system. The values of β' and $1/z'$ via Monte Carlo simulations in 2+1 dimensions from the *equation (4.6)* was reported to be 1 and 0.93±0.1 respectively [6]. These values were in close proximity to that of obtained in the present case from HHCF analysis. In the PLD process, the impinging particles, from laser produced plasma plume on the substrate, arrive within the angular range of 0° to $\pm\theta_{1/2}$ $(\sim cos^{-1}(1/2)^p)$ [7], where $\theta_{1/2}$ is the angle between normal to the target surface and the direction where flux density becomes half of maximum and *p* varies from 7-20 depending on laser spot size on the target, laser fluence and degree of ionization of plasma [7, 8]. In the present work, on Cu target the laser spot size was of ~1 mm diameter and laser fluence was ~ 4 J/cm^2. The corresponding value of p ~ 7-8 gives rise to $\theta_{1/2}$ ~ 22-23° [7]. The glass substrate used has a melting point of ~550 °C and deposition temperature was kept at 400 °C, close to the softening temperature, which have resulted in a very high sticking coefficient, s_0~1. These deposition conditions favouring large shadowing and high sticking coefficient for substrate satisfy the requirement for the surface growth model given by *equation (4.6)* [6]. Under the dynamic scaling, $\Delta = {}^{\beta'}/_{\alpha'} - {}^{1}/_{z'}$, but in the present case, Δ = 0.37 indicates the presence of anomalous scaling behavior and the surface is not self-affine. This is understandable as the growth of the film in PLD is under strong influence of shadowing and thus dynamic scaling no longer holds [9]. Interestingly, the calculated exponents

$(\alpha', \beta', 1/z')$ are quite close to the exponents predicted by the model of mound formation [6, 10]. The oscillating behavior of the HHCF in the region where $r >> \xi$, *figure 4.5*, also indicates the formation of mounded surface particularly for thicker films (deposited for duration, t = 20, 30 and 45 minutes).

Further, the formation of mound surface by power spectral density function (PSDF) analysis was investigated for the PLD films deposited from AFM images. The PSDF [4] (detailed was discussed in *section 3.2.2, chapter 3*) for these films is shown in *figure 4.8*. It displays *P(k)* versus *k* plot extracted from the respective AFM images of Cu films deposited on glass substrates for duration of 6, 8, 10, 20, 30 and 45 minutes. The PSDF shows a characteristics peak, $k_m = 2\pi/\lambda$ (λ= wavelength) for mounded surface and is absent for self-affine surface [4]. The characteristic peak was absent in the PSDF spectra of the films deposited for 6 to 10 minutes duration, *figure 4.8 (a-c)*, indicating the self-affine film surface. The PSDF of the films deposited for duration longer than 10 minutes show characteristics peak depicting mound formation. With increasing time, the peak feature of mounded surface becomes more prominent and k_m ($\sim 1/\xi$) reduces indicating increase in average separation between the islands. Inset in *figure 4.8* shows corresponding 2D fast Fourier transform (FFT) images. It clearly shows a bright ring like structure in *k*-space for films deposited for longer duration, 30 and 45 minutes, further supported the mound growth [11]. From these observations, it is clear that the growth of the Cu film, initially, for the shorter duration of deposition is of predominantly self-affine surface but as deposition progresses film surface becomes mounded with the well-defined characteristic wavelength. The formation of mounds on any surface are basically due to different growth effects such as step-edge barrier, diffusion effect, shadowing, and re-emission, which could be local or non-local in nature. In the present case, the non-local phenomena of strong shadowing owing to the directional nature of PLD along with high sticking condition of substrate (the

deposition performed at glass softening temperature) favours mound formation in Cu films.

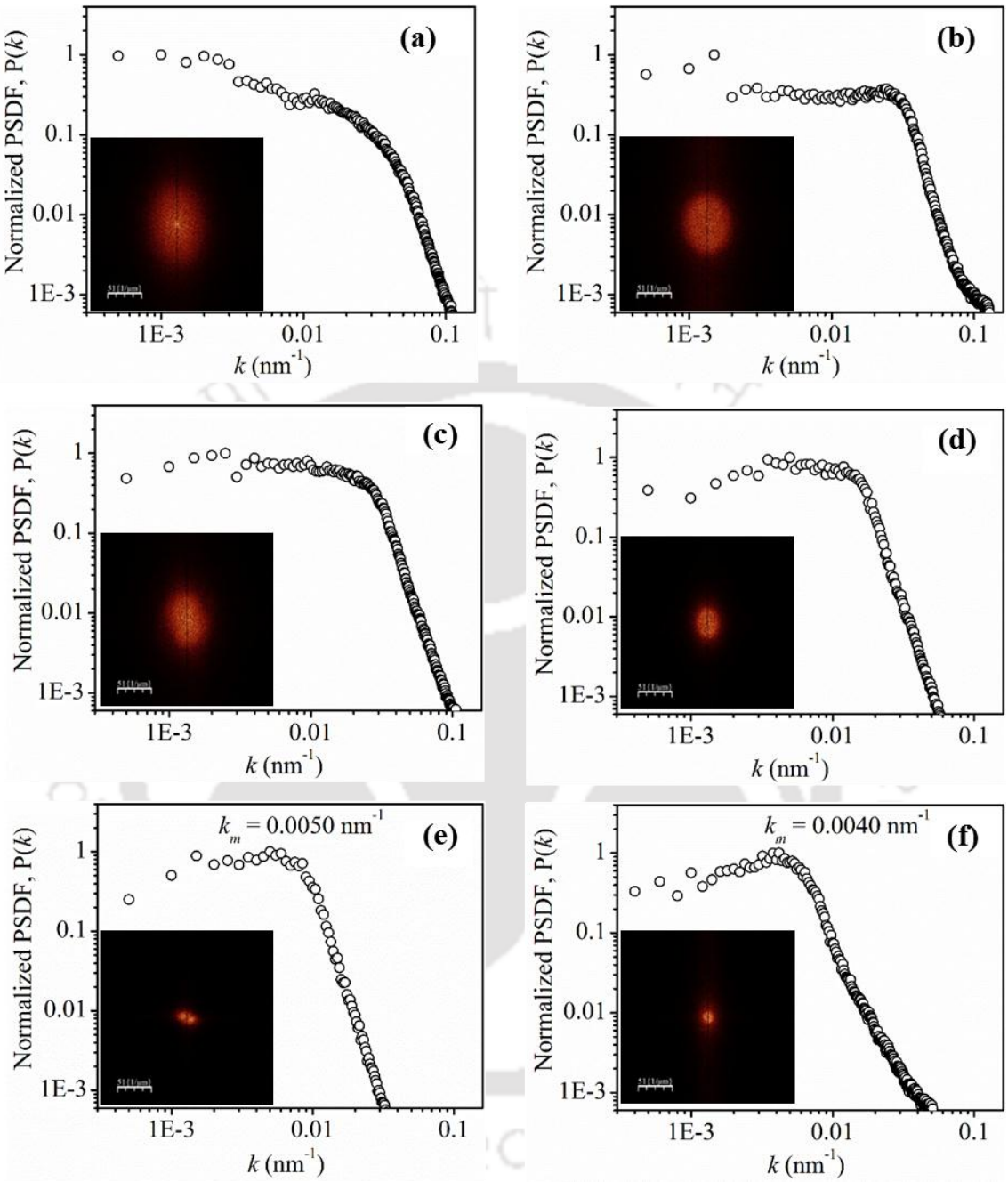

Figure 4.8*: PSDF, P(k) as a function of k (in reciprocal space) for Cu thin films deposited on glass substrate for the deposition time of (a) 6 minutes, (b) 8 minutes, (c) 10 minutes, (d) 20 minutes, (e) 30 minutes and (f) 45 minutes. Inset shows corresponding 2D FFT pattern of the AFM images.*

The PLD Cu thin films deposited at 400°C (near glass softening temperature) for the duration of < 10 minutes has self-affine while for > 10 minutes duration has mounded film. The self-affine films have exhibited better optical (linear and SPR) properties in the visible region compared to that of mounded film which is confirmed by UV-vis-NIR and SE analysis discussed in the next section. Also, due to the high sticking coefficient in the present case, there was the high probabilities for diffusion the nanoparticles towards the substrate further affecting SPR properties of PLD Cu films.

4.4 Effect of deposition time and scaling parameters on the SPR properties of semi-transparent nanostructured PLD Cu thin films

Metal nanoparticles having plasmonic properties possess characteristic SPR peak at which incident light is strongly absorbed or scattered. *Figure 4.9 (a)* and *(b)* show the absorption spectra of Cu films grown for deposition time from 6 minutes to 45 minutes via PLD. All these spectra exhibit the characteristic SPR absorption peak with asymmetric tail towards longer wavelength and broad bandwidth. All these absorbance spectra were fitted with bi-Gaussian lineshape function [12] and are shown in *figure 4.9 (a)* and *(b)* as solid lines for estimation of SPR peak positions and respective bandwidths. For the particle size below 20 nm (films deposited for 6 and 7 minutes) there is an increase in the SPR peak energy from ~1.56 to 1.60 eV (793 to 772 nm) with the increasing particle size from ~14 to 16 nm. For the particle size greater than 20 nm there is a decrease in SPR peak energy from ~1.59 to 1.34 eV with the increasing particle size from ~23 to 123 nm. For the nanoparticles of size below 20 nm, the red shift rather than the blue shift with the decrease in the size could be due to two possible reasons: (1) the scattering rate of conduction electron increases from the surface of the nanoparticles as the size of nanoparticles decreases and (2) surface damping constant of the SP increases as the size of nanoparticles decreases resulting in decrease of the SPR frequency, i.e., the red shift of SPR with

decreasing size [13-15]. For the Cu nanoparticles of size above the 20 nm, the red shift in the SPR peak is in accordance with the classical electrodynamics theory [16]. It is attributed to the retardation effect as well as the contribution due to the multipolar (quarter and octupole) terms [17]. Retardation is due to the phase difference between the field propagating from two different regions of the nanoparticles and it is dominant for coupling of large nanoparticle chains. The SPR peak position and bandwidth as a function of particle size (d) and interface width (w) are shown in *figure 4.9 (c)-(f)* respectively. The surface roughness, w, of the film is also responsible for the shift in SPR peak energy and it decreases with w and similar trend was observed in the present case as shown in *figure 4.9 (d)*.

The broadening of the SPR bandwidth increases abruptly initially from 0.90 to 1.34 eV with increase in particle size from 14 to 26 nm respectively and then it falls down to 0.78 eV with further increase in particle size to 123 nm as shown in *figure 4.9 (e)*. The similar trend was observed in the variation of bandwidth with w as shown *figure 4.9 (f)*.The broadening of SPR band as well as asymmetric nature are due to wide size distribution of nanoparticles within the film, irregularity in its shapes, and increase in surface roughness of the film [18-20]. The bandwidth of SPR has been reported to increase with decreasing particle size exhibiting inverse size effect [15] while it increases in proportion to r.m.s roughness and density of the nanoparticles [19, 21]. In the present case, SPR bandwidth increased for the films deposited from 6 minutes to 10 minutes due to increase in interface width (or r.m.s roughness) from 0.6 nm to 1.51 nm even though the particle size, d, increased from 14 to 26 nm. However, the film deposited for 20 to 45 minutes (d >30 nm) had shown an overall decrease in SPR bandwidth with an increase in d from 54 to 123 nm satisfying the inverse size effect. Thus w and d play important role in shaping up the SPR bandwidth of the plasmonic nanostructured Cu thin films.

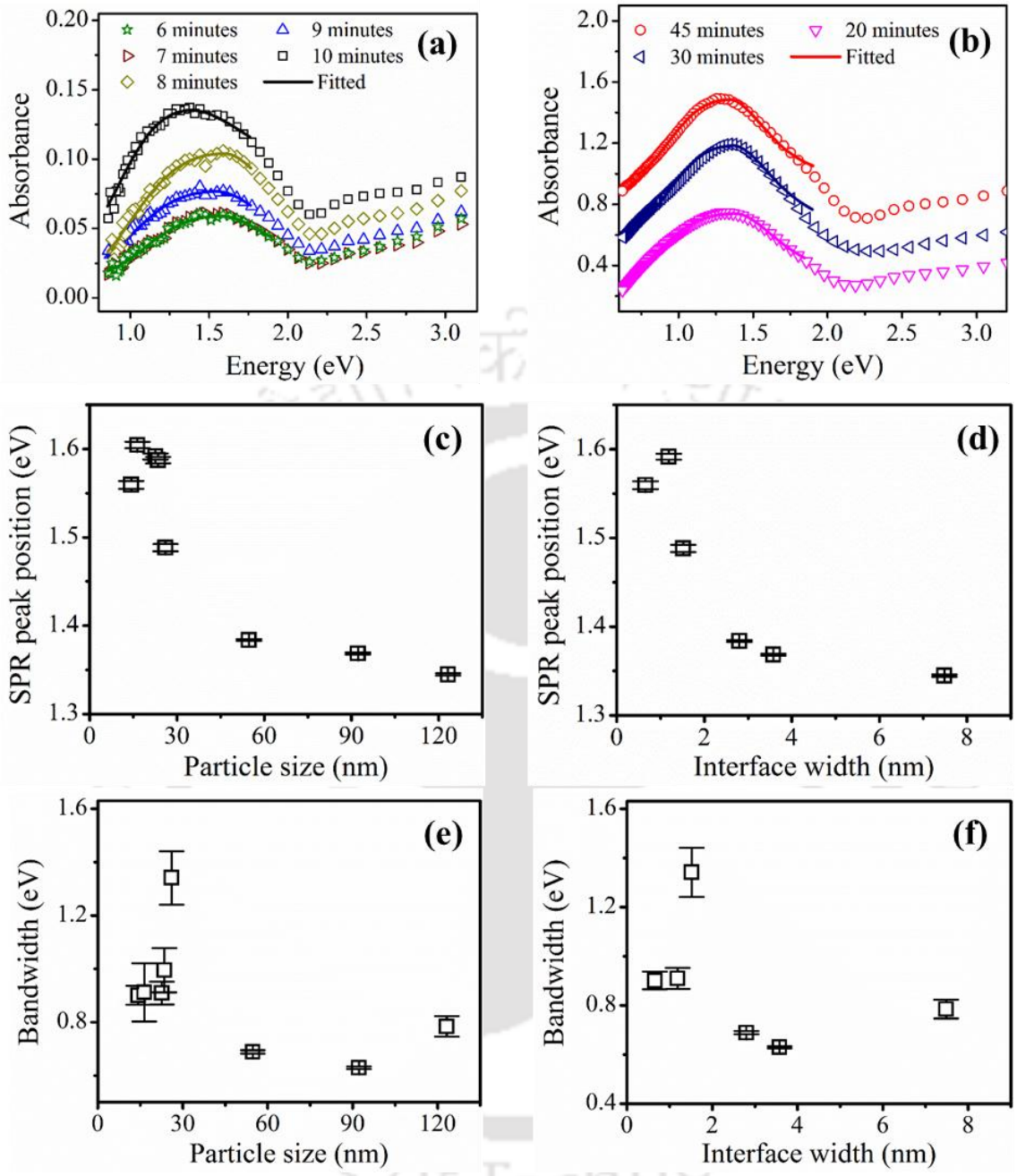

***Figure 4.9**: Absorption spectra of semi-transparent Cu thin films on glass substrate of the deposition duration (a) 6 - 10 minutes and (b) 20- 45 minutes. Variation of peak position as a function of (c) particle size (d) and (d) interface width (w). Bandwidth of SPR as a function of (e) particle size (d) and (f) interface width (w).*

4.5 Analysis of PLD semi-transparent Cu thin films via Spectroscopic Ellipsometer

In the *section 4.3*, it was concluded that the film deposited at 400°C temperature (near glass softening temperature) has very high sticking coefficient, s_o~1. Therefore, there is a large probability for the diffusion of the Cu adatoms toward the substrate forming an oxide interfacial layer in between the metal and glass interface. The formation of oxides at the interface affects the optical and electronic properties [22-24]. The interfacial layer, the composition of PLD main layer and plasmonic behaviour of these semi-transparent nanostructured copper thin films deposited on the glass substrate as a function of deposition time from 6 to 10 minutes were investigated by SE and are presented in this following subsections.

4.5.1 Layer structure considered for ellipsometric analysis

For the estimation of optical constants and thickness of the various layers of the film via SE, appropriate physical model was applied and fitted to the ellipsometric parameters (detailed in *section 3.4, chapter 3,*). Layer structure incorporated in the present case of the semi-transparent copper thin film is shown in *figure 4.10*. This layer structure exhibited the minimum root mean square error (RMSE) value. The first dielectric layer (from the bottom) is of glass substrate (coverslip) having a thickness of ~10^5 nm, which was very large compared to that of the Cu films under investigation. The second layer above the substrate comprises of Cu_2O/CuO interface which was formed due to the formation of bonds between free copper ions (deposited by laser) and oxygen molecules residing at the interface of the glass substrate. The third layer is the main nanoparticles of copper (NP Cu) layer on which an appropriate dispersion law is to be applied. Finally, the top fourth layer is of the cuprous oxide (Cu_2O) film which was formed due to the contamination of copper

surface in the presence of an open atmosphere. In the present case, the top layer of Cu_2O is assumed to be perfectly planar because the roughness of the top layer estimated via AFM was ≤1.6 nm. The space above the top layer and below the substrate is void.

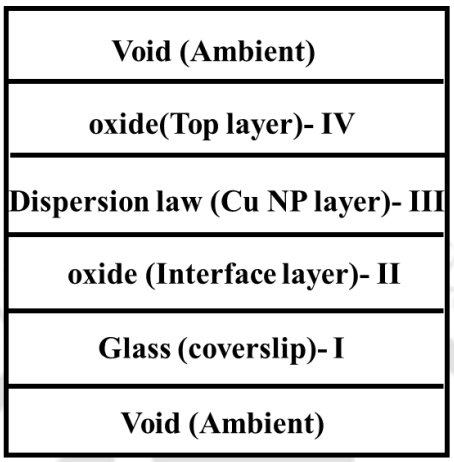

***Figure 4.10**: Schematic of the assumed layer structure.*

4.5.2 Dispersion law for the assessment of layer thickness

For the analysis of ellipsometric data, the substrate, interfacial layer and oxide layer, *n & k′* system generated file (from SEA software) [25] was implemented but for the main nanostructured Cu metallic layer (*figure 4.10*), an appropriate dispersion law was applied. The four oscillators model (combination of one Lorentz and three Gauss model) similar to that of described earlier (*section 3.4*, *chapter 3*), was found to be the most appropriate (giving the minimum value of RSME) for analyse of these thin films and is described by *equation 3.8* and rewritten below [26]

$$\varepsilon_{eff} = \varepsilon_{Lorentz} + \sum_{j=1}^{3} \varepsilon_{j\,Gauss} + \varepsilon_{\infty} \qquad (4.7)$$

Here, the contribution of interband transition was modeled using Lorentz oscillator, $\varepsilon_{Lorentz}$, whereas the two of the Gauss oscillators ($\varepsilon_{j\,Gauss}$ (j = 1, 2)) describe the transverse and longitudinal modes of SPR [27, 28], and contribution of oxide (in fused via interfacial layer and the top layer) was modeled using the third Gauss oscillator which takes into

account of its effect on the plasmonic nanoparticles of Cu. *Figure 4.11* shows the plot of experimentally obtained values of ellipsometry parameters; $tan\psi$ and $cos\Delta$ as a function of energy along with the fitted one, using L-G oscillator dispersion law, *equation 4.7*. The values of RMSE with deposition time for the above stated formulation are listed in *table 4.1*. Further these RMSE values were least for the top layer comprising of Cu_2O for all the films, the interfacial layer of CuO for the films deposited for 6 and 7 minutes and that of Cu_2O for the remaining films. The extremely low values of RMSE as well as excellent matching of the fitted values with the experimental data confirmed the validity of the model considered in the present system. The thickness of each layer with the deposition time obtained from these analyses are listed in *table 4.2*.

***Table 4.1**: RMSE values with the deposition time.*

Deposition time (min.)	RMSE
6	0.00648
7	0.00443
8	0.00372
9	0.00259
10	0.00267

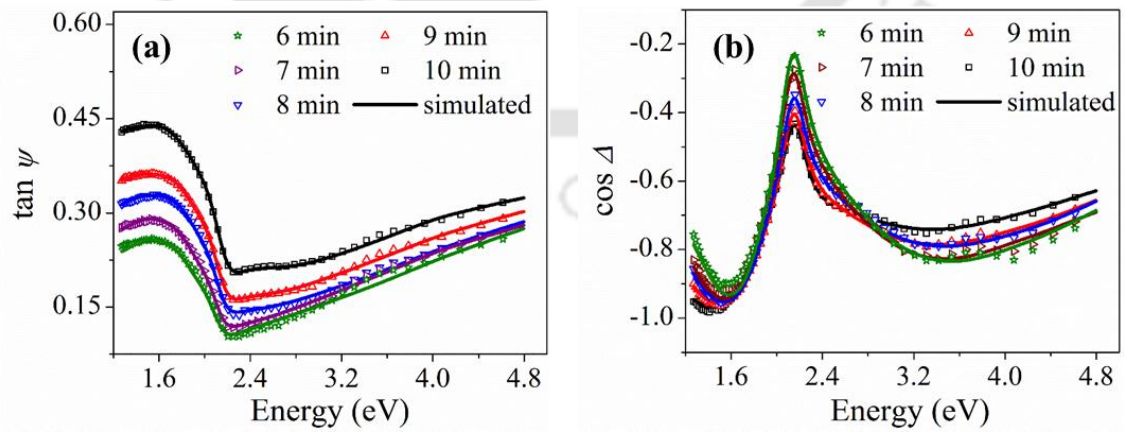

***Figure 4.11**: The estimated and fitted graph of Cu thin films via PLD with the energy (a) $tan\psi$ and (b) $cos\Delta$.*

The formation of oxide layers on the top surface of the film and interface between glass and NP Cu layer have also been reported in the literature [29-31].

***Table 4.2**: Top oxide and interfacial layer thicknesses with deposition time measured via ellipsometry.*

Deposition time (min.)	Top oxide layer thickness (nm)	Cu NPs layer thickness (nm)	Interface thickness (nm)
6	2.58±0.11	30.23± 1.50	0.538±0.027 (CuO)
7	2.88±0.14	34.34±1.70	0.543±0.027 (CuO)
8	2.47±0.12	37.91±1.80	0.374±0.018 (Cu_2O)
9	2.73±0.13	43.08±2.10	0.252±0.012 (Cu_2O)
10	3.29±0.16	47.93±2.30	0.607±0.030 (Cu_2O)

The thickness of the top oxide layer and interfacial layer are small and does not follow any specific trend. However, there is a change in the phase of the oxide in the interfacial layer with the deposition time or alternatively with the thickness of the film. The formation of the interfacial layer depends on the number of free copper ions interacting with free oxygen molecules on glass surface [32]. As the thickness of the copper film increases with the deposition time**,** the probability of availability of free copper ions on the substrate increases and subsequently facilitating the formation of oxygen deficient phase Cu_2O [8].

Figure 4.12 (a) and *(b)* show the real (ε_1) and imaginary (ε_2) part of the pseudo effective dielectric constant for all the films, obtained by considering the layer structure of *figure 4.10* and the dispersion model described by *equation 4.7*. The spectra for ε_2 clearly exhibit the peak around 1.22- 1.83 eV further confirming the formation of oxide layer [30]. The energy of all the four oscillators (*equation 4.7*) obtained for Cu thin film are listed in *table 4.3*.

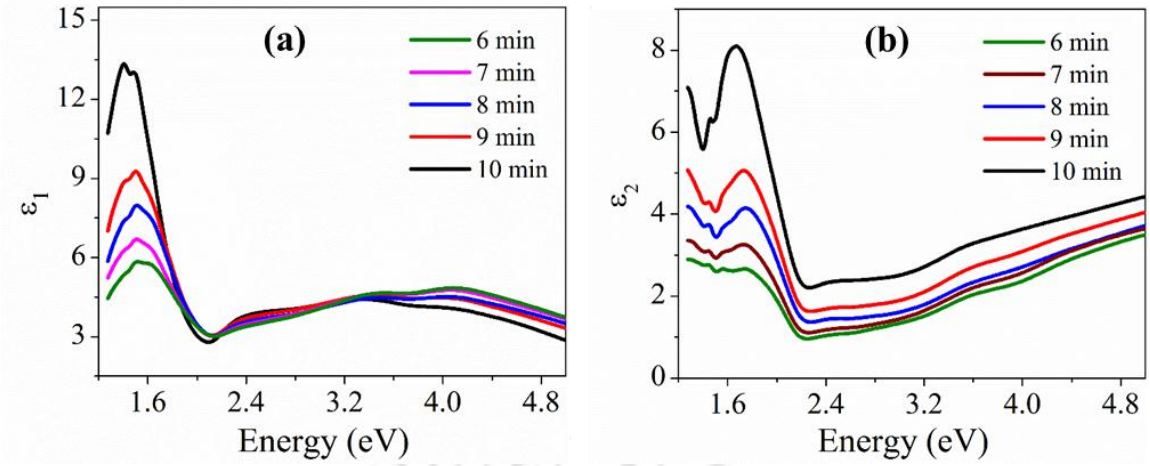

***Figure 4.12**: Effective dielectric constant of the deposited copper film considering the native oxide top and the interface layer (a) real part ε_1 and (b) imaginary part ε_2.*

***Table 4.3**: Values of all the four oscillator energy with the deposition time.*

Deposition time (min.)	E_{o1} (eV)	E_{o2} (eV)	E_{o3} (eV)	E_{o4} (eV)
6	1.71±0.013	1.75±0.013	1.50±0.050	2.01±0.025
7	1.72±0.009	1.84±0.029	1.63±0.108	2.03±0.017
8	1.89±0.018	1.83±0.030	1.62±0.196	2.03±0.014
9	2.03±0.020	1.83±0.018	1.58±0.145	2.02±0.009
10	2.24±0.023	1.79±0.009	1.47±0.010	2.02±0.006

The first oscillator energy (E_{o1}, Lorentz model) contributes to the interband transition. The reported value of interband transition energy of Cu lies the range of 2.1 to 5.1 eV [33]. However, it was also reported that the interband transition or d-band transition peak of metal is shifted towards lower energy as the size of the nanoparticles decreases [34]. In the present case, the interband oscillator peak energy shows a subtle shift towards the lower energy from 2.24 eV to 1.70 eV on the reduction of particle size from 26.04 nm to 14.22 nm. The second oscillator (E_{o2}, Gauss model) corresponds to the transverse mode of the SPR due to the columnar shape of the nanoparticles (*figure 4.3 (i)*) having the energy within the range of 1.75 eV to 1.84 eV [15, 28]. The third oscillator (E_{o3}, Gauss model) corresponds to the longitudinal mode of the SPR which varies with the size of the

nanoparticles and nearly matching with the absorbance peak obtained from the UV-visible transmission spectrum (*figure 4.9*). There was not much variation in the fourth oscillator peak energy (E_{04}, Gauss model) and its value was around 2.01-2.03 eV. It is attributed to the oxide formation on the top of Cu film and is in agreement with the band gap energy of Cu_2O which was reported to be around 2.1 – 2.4 eV [35]. *Figure 4.13* shows the evolution of linear refractive index and extinction coefficient of plasmonic Cu NPs thin layer over the energy ranging from 1.3 to 5 eV. Plasmonic Cu nanoparticles embedded in the glass substrate exhibits larger refractive index compared to that of the bulk copper [36]. The extinction coefficient of plasmonic Cu nanoparticles layer shows a peak near around 1.88-1.80 eV for all the samples and follow the similar trend as that of the absorption spectrum of Cu thin film (*figure 4.9*) [30]. The shift in the absorption peak, asymmetric tail and broadening in the extinction coefficient (absorption spectrum) was due to the presence of oxide in the Cu film apart from wide size distribution of nanoparticle [37].

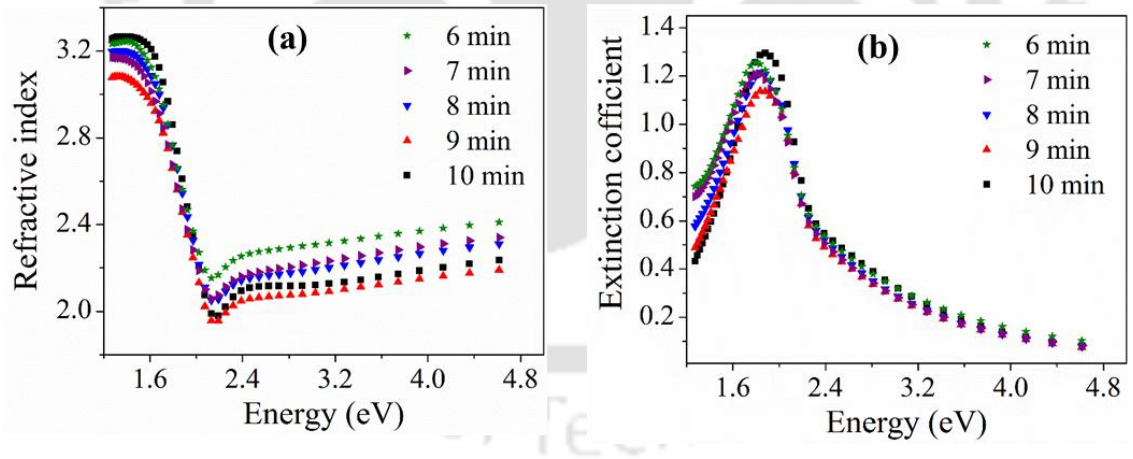

***Figure 4.13**: The plasmonic copper thin films deposited at different deposition time (a) linear refractive index and (b) extinction coefficient as a function of energy.*

4.5.3 Application of Bruggeman Effective medium approximation (BEMA)

The layer structure considered for the estimation of the type of the constituent species and their volume fraction using Bruggman effective medium approximation

(BEMA) model [38] for the semi-transparent PLD Cu thin film is shown in *figure 4.14*. In this case, above the glass substrate, the main layer of PLD Cu nanostructured film is considered to be a combination of the plasmonic nanoparticle of Cu (NP Cu), copper oxide (Cu_2O) and voids.

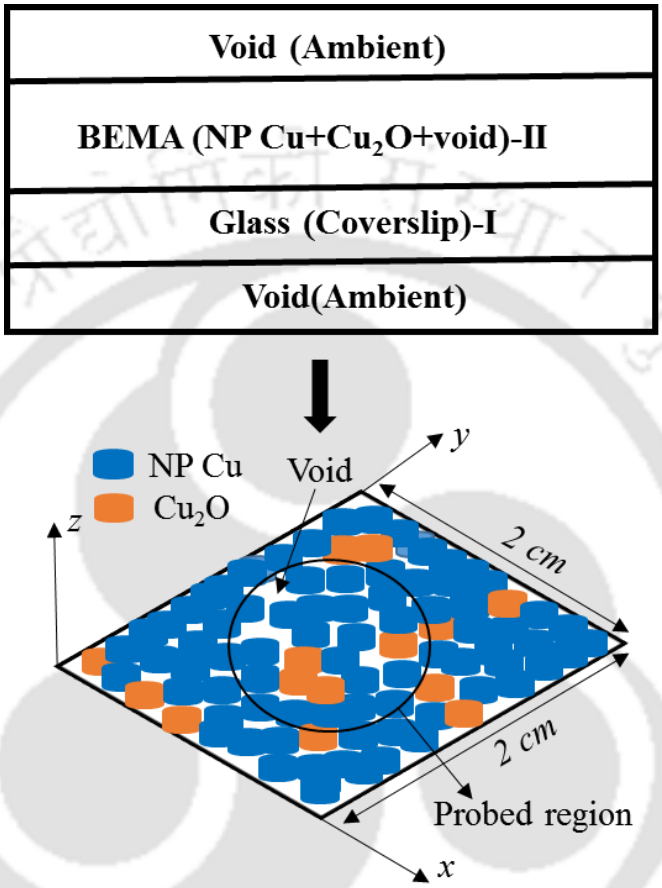

***Figure 4.14**: Schematic of the assumed layer structure of PLD Cu thin film deposited at 400°C substrate temperature.*

4.5.4 Layer thickness, percentage of composition and oscillator energies as a function of deposition duration for PLD Cu thin film via BEMA

To determine the type of the constituent species and optical properties of the thin film, the numerical simulation of the ellipsometer spectra were performed using BEMA (detailed was discussed in *section 3.4*, *chapter 3*) for the layered structure as shown in *figure 4.14*. In the present case, the constituent species are Cu_2O (cuprous oxide), plasmonic

nanoparticles and void. The values of dielectric constant; ε_{Cu_2O}, and ε_{void}were taken directly from the system generated file (from SEA software) whereas for the NP Cu, $\varepsilon_{plasmonic}$, using the suitable dispersion law formed with a combination of Lorentz and Gauss oscillators (L-G) (*section 3.4, chapter 3, equation 3.8*). *Figure 4.15* illustrates the experimental and fitted data for the physical model discussed in *section 4.5.3* for which the values of RMSE is least. The estimated value of percentage of the constituent species with the deposition time for the PLD Cu films from BEMA is listed in *table 4.4* and *4.5* respectively.

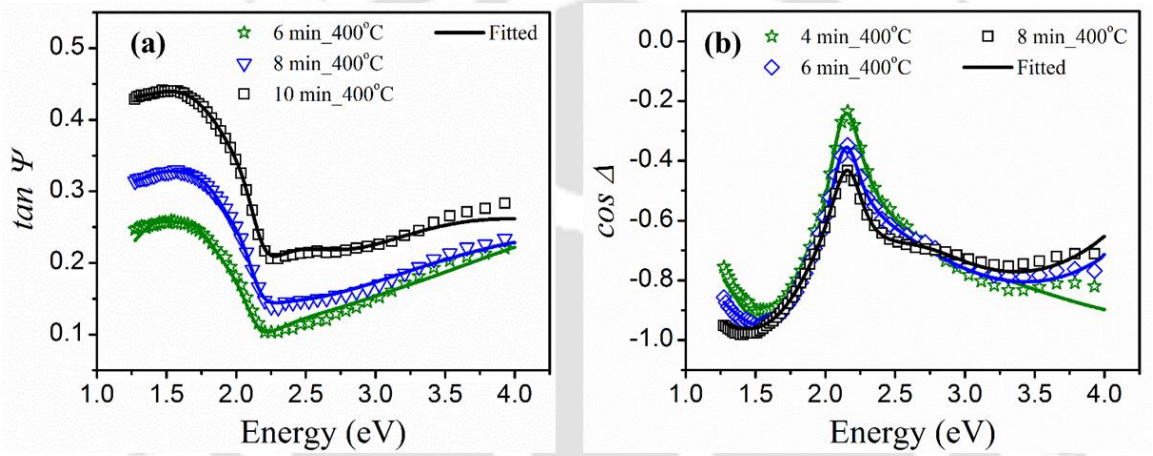

Figure 4.15: *The experimental and fitted graph of PLD nanostructured Cu thin film as the function of energy (a) tanψ and (b) cosΔ.*

In the BEMA analysis, it was observed that the film thickness measured by dispersion law is nearly matching with that of obtained in previous *section 4.5, table 4.2*. The percentage of void and Cu_2O were observed to be very small. It signifies that all the deposited films are highly dense packed which was also confirmed by 2D AFM images (*figure 4.3*). The estimated oscillators energy values are also nearly matching with the results obtained from dispersion law only. But the fitted curve for $tan\psi$ and $\cos\Delta$ shows the deviation with respect to the corresponding experimental values, *figure 4.15* as compared to that of *figure 4.11*.

***Table 4.4**: Thickness and percentage of the constituent species for films deposited at 400°C with the deposition time measured via ellipsometry.*

Deposition Time (minutes)	Thickness (nm)	% NP Cu	% Cu_2O	% void
6	33.00±0.08	100.03	-0.03	---
8	43.86±0.01	99.90	0.02	---
10	52.15±0.06	97.30	0.07	2.63

***Table 4.5**: Fitting parameter of oscillator energy for all the oscillator model for films deposited at 400°C with deposition time.*

Deposition time (minutes)	E_{01} (eV)	E_{02} (eV)	E_{03} (eV)	E_{04} (eV)
6	1.46±0.12	1.73±0.02	1.45±0.03	2.00±0.05
8	1.79±0.01	1.85±0.07	1.65±0.28	2.03±0.03
10	2.43±0.15	1.78±0.02	1.48±0.13	2.02±0.05

4.6 Conclusions

In this chapter properties of PLD semi-transparent Cu films deposited at a temperature of 400°C are presented. The XRD spectra showed the dominating peak corresponding to Cu (111) and relatively week peak corresponding to Cu (220) with average crystallite size increasing from 3.6 to 29.5 nm with increasing deposition time. From HHCF analysis (obtained from AFM images), the interface width (RMS roughness), *w*, was observed to scale with depositing time (*t*) as, $\sim t^{1.07\pm0.11}$ while lateral correlation length ξ grows as $t^{0.70\pm0.10}$affirming the faster vertical growth compared to the lateral growth. The average roughness exponent $\alpha'$was observed to be nearly 0.95. The results showed that shadowing instability model for deposition with no remission explains well the growth of PLD Cu films onto SiO_2. The strong shadowing effect is attributed to the directional nature of PLD. The high sticking probability was due to the deposition taking

place at around softening temperature of the substrate. From the analysis of PSDF and 2D FFT, the evolution of the PLD Cu films follows strong shadowing assisted mound-like growth. The high sticking probability has certainty to diffuse the incoming nanoparticles towards the substrate and form a Cu oxide interfacial layer and was confirmed by SE analysis. The shift and broadening of the SPR peak were due to the change in the size and shape of the nanoparticles as well as the formation of the oxides layer at the top surface and between the metal-glass interfaces. From the analysis of surface morphology, the scaling behaviour, the growth model of the film deposited can be predicated ex-situ which is not only helpful in understanding the nucleation process but also plays an important role in correlating with the physical properties of the thin film. All this information will prove to be very useful to assess the device performance. The dispersion model was observed to be best fitted to assess the thickness of the top oxide layer and interfacial layer. By applying BEMA the percentage of composition of Cu NP, Cu_2O and voids are obtained. But otherwise the deviation in $tan\psi$ and $\cos\Delta$ were large as compared to that of obtained via dispersion model only.

Bibliography

[1] V. Figueiredo, E. Elangovan, G. Goncalves, P. Barquinha, L. Pereira, N. Franco, E. Alves, R. Martins, E. Fortunato, Effect of post-annealing on the properties of copper oxide thin films obtained from the oxidation of evaporated metallic copper, Applied Surface Science, 254 (2008) 3949-3954.

[2] P.P. Dey, A. Khare, Stoichiometry-dependent linear and nonlinear optical properties of PLD SiOx thin films, Journal of Alloys and Compounds, 706 (2017) 370-376.

[3] M. Pelliccione, T.-M. Lu, Evolution of thin film morphology modeling and simulations, Berlin: Springer, 2008. ISBN: 978-0-387-75108-5, (2008).

[4] M. Pelliccione, T.-M. Lu, Evolution of thin film morphology, Springer, 2008.

[5] J. Jeffries, J.-K. Zuo, M. Craig, Instability of kinetic roughening in sputter-deposition growth of Pt on glass, Physical review letters, 76 (1996) 4931.

[6] J.T. Drotar, Y.-P. Zhao, T.-M. Lu, G.-C. Wang, Surface roughening in shadowing growth and etching in 2+ 1 dimensions, Physical Review B, 62 (2000) 2118.

[7] I. Weaver, C. Lewis, Polar distribution of ablated atomic material during the pulsed laser deposition of Cu in vacuum: Dependence on focused laser spot size and power density, Journal of applied physics, 79 (1996) 7216-7222.

[8] D.B. Chrisey, G.K. Hubler, Pulsed laser deposition of thin films, John Wiley & Sons, Inc., 1994.

[9] J.J. Ramasco, J.M. López, M.A. Rodríguez, Generic dynamic scaling in kinetic roughening, Physical review letters, 84 (2000) 2199.

[10] J.H. Yao, H. Guo, Shadowing instability in three dimensions, Physical Review E, 47 (1993) 1007.

[11] S.M. Obaidulla, P. Giri, Surface roughening and scaling behavior of vacuum-deposited SnCl2Pc organic thin films on different substrates, Applied Physics Letters, 107 (2015) 221910.

[12] T. Buys, K. De Clerk, Bi-Gaussian fitting of skewed peaks, Analytical Chemistry, 44 (1972) 1273-1275.

[13] S. Link, M.A. El-Sayed, Size and temperature dependence of the plasmon absorption of colloidal gold nanoparticles, The Journal of Physical Chemistry B, 103 (1999) 4212-4217.

[14] O.A. Yeshchenko, I.M. Dmitruk, A.A. Alexeenko, A.V. Kotko, J. Verdal, A.O. Pinchuk, Size and temperature effects on the surface plasmon resonance in silver nanoparticles, Plasmonics, 7 (2012) 685-694.

[15] S. Link, M.A. El-Sayed, Shape and size dependence of radiative, non-radiative and photothermal properties of gold nanocrystals, International reviews in physical chemistry, 19 (2000) 409-453.

[16] C. Noguez, Surface plasmons on metal nanoparticles: the influence of shape and physical environment, The Journal of Physical Chemistry C, 111 (2007) 3806-3819.

[17] T.J. Davis, K.C. Vernon, D.E. Gómez, Effect of retardation on localized surface plasmon resonances in a metallic nanorod, Optics express, 17 (2009) 23655-23663.

[18] V.N. Rai, A.K. Srivastava, C. Mukherjee, S.K. Deb, Surface enhanced absorption and transmission from dye coated gold nanoparticles in thin films, Applied optics, 51 (2012) 2606-2615.

[19] G. Rasigni, F. Varnier, M. Rasigni, J. Palmari, A. Llebaria, Roughness spectrum and surface plasmons for surfaces of silver, copper, gold, and magnesium deposits, Physical Review B, 27 (1983) 819.

[20] L.M. Liz-Marzán, Tailoring surface plasmons through the morphology and assembly of metal nanoparticles, Langmuir, 22 (2006) 32-41.

[21] N. Fang, Z. Liu, T.-J. Yen, X. Zhang, Experimental study of transmission enhancement of evanescent waves through silver films assisted by surface plasmon excitation, Applied Physics A, 80 (2005) 1315-1325.

[22] A. Agrawal, R.W. Johns, D.J. Milliron, Control of localized surface plasmon resonances in metal oxide nanocrystals, Annual Review of Materials Research, 47 (2017) 1-31.

[23] N. Benito, M. Flores, Evidence of Mixed Oxide Formation on the Cu/SiO2 Interface, The Journal of Physical Chemistry C, 121 (2017) 18771-18778.

[24] D. Das, T. Kundu, M. Dey, S. Chakraborty, D. Chakravorty, Electrical conduction in composites containing copper core-copper oxide shell nanostructure in silica gel, Journal of Chemical Sciences, 115 (2003) 341-348.

[25] E. Palik, Handbook of optical constants of solids, Orlando : Academic Press, 1985., 1985.

[26] H. Bakkali, E. Blanco, M. Dominguez, M. de la Mora, C. Sánchez-Aké, M. Villagrán-Muniz, Optical properties of Au–TiO2 and Au–SiO2 granular metal thin films studied by spectroscopic ellipsometry, Applied Surface Science, 405 (2017) 240-246.

[27] M. Lončarić, J. Sancho-Parramon, H. Zorc, Optical properties of gold island films—a spectroscopic ellipsometry study, Thin Solid Films, 519 (2011) 2946-2950.

[28] X.-Y. Zhang, A. Hu, T. Zhang, W. Lei, X.-J. Xue, Y. Zhou, W.W. Duley, Self-Assembly of Large-Scale and Ultrathin Silver Nanoplate Films with Tunable Plasmon Resonance Properties, ACS Nano, 5 (2011) 9082-9092.

[29] I. Platzman, R. Brener, H. Haick, R. Tannenbaum, Oxidation of Polycrystalline Copper Thin Films at Ambient Conditions, The Journal of Physical Chemistry C, 112 (2008) 1101-1108.

[30] M. Rauh, P. Wiβmann, M. Wölfel, Ellipsometric studies on the oxidation of thin copper films, Thin solid films, 233 (1993) 289-292.

[31] M. He, T.-M. Lu, Metal-dielectric interfaces in gigascale electronics: thermal and electrical stability, Springer Science & Business Media, 2012.

[32] T. Fukuda, H. Nishino, A. Matsuura, H. Matsunaga, Force Driving Cu Diffusion into Interlayer Dielectrics, Japanese Journal of Applied Physics, 41 (2002) L537-L539.

[33] P.B. Johnson, R.-W. Christy, Optical constants of the noble metals, Physical review B, 6 (1972) 4370.

[34] B. Balamurugan, T. Maruyama, Size-modified d bands and associated interband absorption of Ag nanoparticles, Journal of applied physics, 102 (2007) 034306.

[35] N. Serin, T. Serin, Ş. Horzum, Y. Çelik, Annealing effects on the properties of copper oxide thin films prepared by chemical deposition, Semiconductor Science and Technology, 20 (2005) 398-401.

[36] H. Savaloni, F. Babaei, S. Song, F. Placido, Influence of substrate rotation speed on the nanostructure of sculptured Cu thin films, Vacuum, 85 (2011) 776-781.

[37] O. Peña-Rodríguez, U. Pal, Effects of surface oxidation on the linear optical properties of Cu nanoparticles, JOSA B, 28 (2011) 2735-2739.

[38] H. Fujiwara, Spectroscopic ellipsometry: principles and applications, John Wiley & Sons, 2007.

Chapter 5

Third order nonlinear optical properties of the PLD semi-transparent nanostructured Cu thin films

The large nonlinear signal and fast response time of the metallic nanostructured thin film can be of potential applications in fast optoelectronics devices, optical switches, optical limiters, optical computing, optical memories, and nonlinear spectroscopy [1-9]. Additionally, metal nanoparticles embedded in the glass/dielectric exhibit second-harmonic generation (SHG), third-harmonic generation (THG) [10-13], sum-frequency generation (SFG), self-focusing and defocusing, multi-photon absorption [2, 5, 14, 15], nonlinear Raman stimulated scattering [16, 17] , optical parametric amplification (OPA) [18, 19], self-phase modulation (SPM) [20-22], optical solitons [23], four-wave mixing (FWM) [24, 25] etc. The origin of optical nonlinearity in the metallic nanostructured thin films is due to intraband transition, interband transition, and hot electrons formation [5, 14]. The intraband transition is due to the oscillations of free electrons and depends on the size and shape of the nanoparticles but it dominates only for the size below 20 nm [26]. The interband transition is due to the bound electron transition from inner core d- band to conduction band and is dependent on the size of the nanoparticles [27]. In the noble metals (Au, Ag, Cu), the contribution of the interband transition plays a significant role in the optical nonlinearity [26, 28]. The nonlinear optical (NLO) effect via hot electrons is normally independent of size and shape of the nanoparticles. However, there are some reports which show that the tuning of the size and shape of the nanoparticles could effect the formation of hot electron [29, 30]. The formation of the hot electrons modifies the

density of the conduction band electrons which in turn alter the dielectric constant of metal nanoparticles affecting the optical nonlinearity of the nanostructured metal thin film [31]. Moreover, the hot electrons contribution becomes dominant compared to that of the intraband and interband transition under the continuous wave (cw) pump laser instead of the pulsed laser. In the case of photon energy of the incident laser beam being shorter than the interband transition threshold, the energy transfer to the electron gas occurs through free carrier absorption, without perturbing the d-band electrons [26, 28]. The NLO properties of the nanostructured metallic thin films are influenced by the mismatch between the photon energy of incident laser (pump) and SPR peak and pulse duration (for pulsed laser) of pump laser apart from nanoparticle size, shape and surface roughness [26].

In this chapter, the measurement of the third order optical nonlinearity of pulsed laser deposited (PLD) nanostructured copper (Cu) thin films using modified Z-scan setup is documented. In the modified Z-scan setup, the photodiode of the conventional Z-scan is replaced by a charge-coupled device (CCD) camera, thereby improving the sensitivity of the technique [32]. The effect of size of the nanoparticles and substrate temperature on the NLA and NLR coefficient of the nanostructured Cu thin films is detailed in this chapter.

5.1 Experimental details

For NLO studies, both the sets of PLD Cu thin films, deposited at room temperature (RT) and gradually annealed and another set deposited directly at elevated substrate temperature of 400°C, *chapter 2, section 2.1*, were subjected to modified Z-scan for the NLO characterization. In the modified Z-scan set-up, employed in present thesis (*chapter 2, section 2.2.5*), a continuous wave (cw) Helium-Neon (He-Ne) laser was focused on the PLD Cu thin film using a convex lens of focal length of 50 mm. The film was translated from -15 mm to +15 mm w.r.t. focal plane on both the sides of the lens in a step of 1 mm

and transmitted beam was imaged on CCD. The recorded CCD images of the transmitted beam through the thin film positioned at 10 mm from the focal point is shown as an example in *Figure 5.1 (a)* for OA Z-scan and *(b)* corresponding masked image for CA Z-scan for S~ 0.40 (where S is the ratio of transmitted intensity with aperture (closed aperture (CA)) to that of without aperture (open aperture (OA))) by implementing a software aperture [32]. The transmitted intensity through the film at each location (*z*) was obtained by integrating the grey values of the recorded respective CCD image using a Matlab program. The corresponding data for CA was obtained from the cropped images for S~ 0.4. From these images, the value of nonlinear absorption (NLA) and nonlinear refraction (NLR) coefficients were measured.

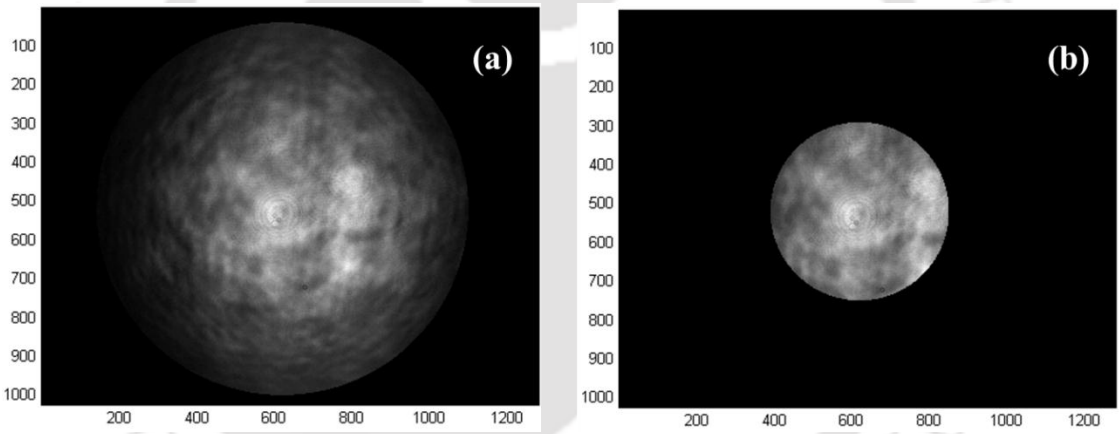

Figure 5.1: *CCD image of transmitted beam through PLD nanostructured Cu film, fabricated at a substrate temperature of 400 °C, positioned at 10 mm from the focal point: (a) open aperture and (b) closed aperture for S~0.40.*

5.2 Estimation of NLA and NLR coefficients

The intensity dependent absorption coefficient, $\alpha(I)$, and refraction index, $n(I)$, are expressed by, $\alpha(I) = \alpha + \beta I$ and $n(I) = n + n_2 I$, where α is the linear absorption coefficient (obtained from SE measurement), n is the linear refractive index (obtained from SE measurement), β is the nonlinear absorption coefficient, n_2 is nonlinear refractive index

coefficient and I the intensity of the laser beam incident on the sample [19]. The experimental open and closed aperture transmission curves were fitted to following *equations (5.1)* and *(5.2)* to obtain the values of β and n_2, respectively [14, 33].

$$T_{open}(z) = 1 \pm \frac{\beta I_o L_{eff}}{2^{3/2}[1+(z/z_o)^2]} \quad (5.1)$$

$$T_{closed}(z) = 1 + \frac{4n_2 I_o L_{eff}(z/z_o)k}{[1+(z/z_o)^2][9+(z/z_o)^2]} \quad (5.2)$$

where T_{open} and T_{closed} are the normalized transmission for OA and CA Z-scan respectively. In the *equation (5.1)*, the -ve sign is for reverse saturation absorption (RSA) and that of +ve sign for saturation absorption (SA) [32]. The I_o, L_{eff}, z_o, and k represent peak intensity at the focal plane, effective sample thickness, Rayleigh length, and magnitude of wave vector respectively. The L_{eff} is the effective thickness of the film given by equation,

$$L_{eff} = \frac{1-\exp(-\alpha L)}{\alpha} \quad (5.3)$$

where, L is the film thickness.

In the CA Z-scan, if a transmittance minimum (valley) prior to focus followed by a transmittance maximum (peak) after focus occur then this type of valley-peak signature indicates the self-focusing property, which corresponds to the positive nonlinear refractive index coefficient, n_2. On the other hand if the peak prior to focus followed by a valley after focus appear then it is the indication of the self-defocusing property, corresponding to negative value of n_2. The Rayleigh length, z_o, is given by [34],

$$z_o = \frac{\pi w_o^2}{\lambda} \quad (5.4)$$

where w_o is the beam diameter at the focus (z = 0) which was estimated using the relation,

$$w_0^2 = \frac{f\lambda}{D} \quad (5.5)$$

where *f* is the focal length of the lens (5 cm), *D* is the laser beam diameter coming out of the laser (~ 1.40 mm) and λ is the laser wavelength (632.8 nm). From this, the value of $z_0$comes out to be ~ 2.50 mm. The thickness of the films, in the present work, is less than 60 nm and thus it satisfies the thin film approximation [19].

5.3 Effect of annealing temperature and deposition time on the third order NLR coefficient of PLD nanostructured Cu thin films

Figure 5.2 shows the normalized transmittance plot for CA Z-scan as a function of the sample position (*z*) w.r.t focus of the lens for nanostructured Cu thin films deposited at RT and then finally annealed up to 400°C for the deposition duration of (a) 4 minutes, (b) 6 minutes and (c) 8 minutes (*section 2.1, chapter 2*). All these CA Z-scan spectra (*Figure 5.2(a-c)*), demonstrate a transmittance minimum (valley) prior to focus followed by a transmittance maximum (peak) after focus. This valley-peak signature indicates the self-focusing property, which corresponds to positive nonlinear refractive index n_2. The value of n_2 was calculated from the CA Z-scan data after fitting to *equation (5.2)*. The measured valley to-peak separation, Δz_{p-v}, is close to $1.7z_o$, confirming the third order optical nonlinearity [32]. In the nanostructured Cu thin film, both self-focusing and de-focusing in refraction has been reported in literature [26, 28].

In the present case of nanostructured metal thin film, the incident laser photon energy (~1.96 eV) lies far away from the SPR peak, a non-resonant regime, thus the positive nonlinearity is arising from the hot electron contribution. But on tuning the laser photon energy near to the SPR peak, resonant regime, the sign and magnitude of the nonlinearity undergo a change due to the complex nature of the local field [26, 28, 35]. In the present case, the Z-scan measurements, a cw-laser was used, therefore optical nonlinearity induced

in the films could be dominated by hot electron formation particular in non-resonant regime [36].

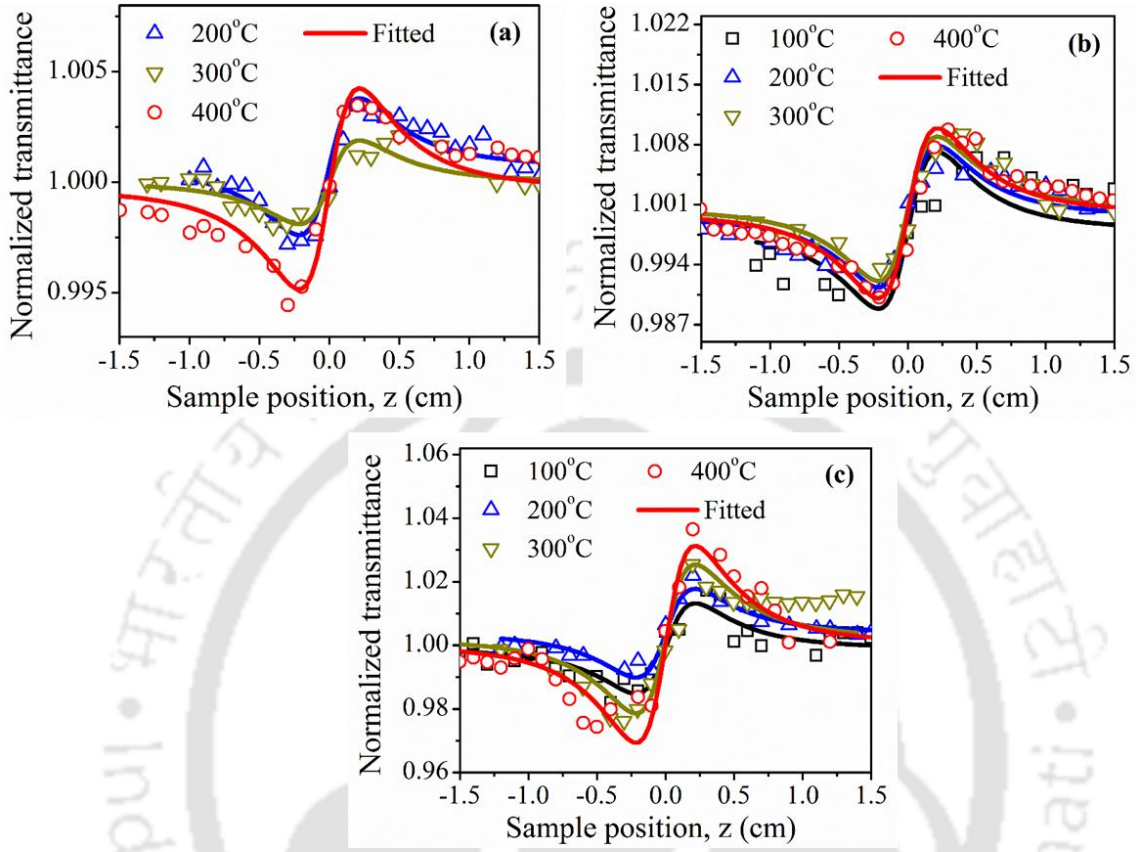

***Figure 5.2**: CA normalized transmittance curve of nanostructure Cu thin films deposited at RT and then gradual annealed for 100°C, 200°C, 300°C and 400°C for the deposition time of (a) 4 minutes, (b) 6 minutes and (c) 8 minutes.*

The fractal nature and roughness of the film also play a significant role on the NLO properties of the nanostructured metal films [37, 38]. In the present set of films, the Gaussian beam from a cw He-Ne laser (wavelength ~ 632.8 nm (~1.96 eV)), far from both the transverse and longitudinal SPR peaks position of the deposited films (detailed in *section 3.3, chapter 3*), propagates through the sample. The sample absorbs the laser light and immediately gives rise to local heating which results in the generation of a large amount of electrons in the conduction band (hot electrons). The number of hot electrons thus

formed is proportional to the local temperature changes on the film surface due to the laser heating. This change in the electron distribution near the Fermi level thus affects the nonlinear properties of the film. The change in the refractive index depends on the distribution of electrons near the Fermi level which in turn varies linearly with change in local temperature [29]. Due to the Gaussian nature of the He:Ne laser beam, a gradient in temperature and hence a spatially varying refractive index region forming a thermal lens. This results in the self-focusing effect (*figure 5.2*) [31, 39]. The variation of the NLR coefficient as a function of annealing temperature and deposition time are shown in *figure 5.3 (a) and (b)* respectively. The measured values of NLR coefficient for all the samples are listed in *table 5.1*.

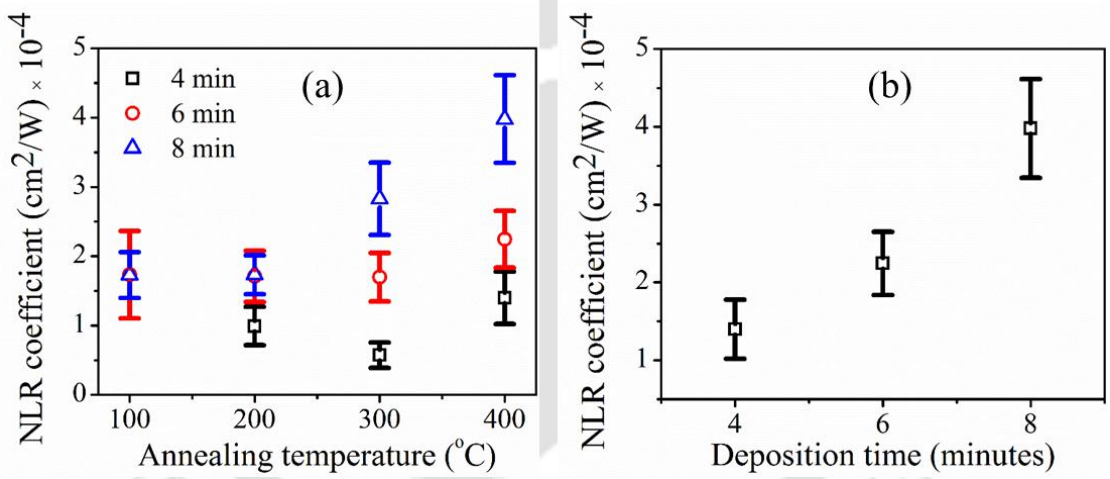

***Figure 5.3**: (a) NLR coefficient of PLD deposited nanostructured Cu thin film as a function of annealing temperature and (b) NLR coefficient of gradually post annealed to 400°C PLD Cu thin film as a function of deposition duration.*

The films deposited for the duration of 4, 6 and 8 minutes at RT do not display any optical nonlinearity. It was observed that the 4 minutes duration film annealed at 100°C also did not show any optical nonlinearity. However, after gradual annealing for 200°C and above it, 300°C and 400°C, it exhibited the nonlinear refraction. The value of n_2 for the film annealed up to 200°C and 300°C were $(0.99 \pm 0.27) \times 10^{-4}$ cm^2/W and $(0.57 \pm 0.18) \times 10^{-}$

^{4} cm^2/W respectively. After annealing finally up to 400°C, the value of NLR coefficient was enhanced to $(1.40 \pm 0.39) \times 10^{-4}$ cm^2/W.

Table 5.1: *NLR coefficient of post annealed PLD Cu thin films.*

Deposition duration (minutes)	NLR coefficient (n_2) (cm^2/W) × 10^{-4}			
	Annealing temperature (°C)			
	100	200	300	400
4	---	0.99 ± 0.27	0.57 ± 0.18	1.40 ± 0.39
6	1.73 ± 0.62	1.71 ± 0.37	1.70 ± 0.35	2.24 ± 0.40
8	1.72 ± 0.33	1.73 ± 0.28	2.83 ± 0.52	3.98 ± 0.63

The changes in the NLO coefficient as a function of annealing temperature due to the change in the shape and size of the nanoparticles as well as modification of the electron density near Fermi level. It was observed that from the RT to a final annealing temperature of 400°C, the shape of the nanoparticles changed from columnar to conical with the broad base while the size of nanoparticle changed from ~ 10 nm to 288 nm (*section 3.2, chapter 3*). Moreover, the distribution of electrons in the d-band near the Fermi level (responsible for hot electron formation) was modified at higher annealing temperature. The activation energy (*section 3.2.2, chapter 3*) and SE analysis (*section 3.4, chapter 3*) confirmed the change in electron distribution near the Fermi level of post annealed films. It was observed that the activation energy of film annealed to 400°C is positive which signified the modification in the Fermi level. Similarly, in the SE analysis, four oscillators dispersion model was fitted well for annealed films while that of for RT films, two oscillators model, further confirming the modification of distribution of electrons near Fermi level. Hence resulted into an increase in the NLR coefficient at higher annealing temperature [29, 31, 40].

The 6 minutes deposited film after gradually annealed for 100°C, 200°C, 300°C

and any effect of annealing temperature up to 300ºC on the NLR coefficient and its value remained ~1.71 ± 0.37 × 10^{-4} cm^2/W. But the film annealed to a final temperature of 400ºC exhibited the higher value of NLR coefficient and is found to be (2.24 ± 0.40) × 10^{-4} cm^2/W. It was again due to the change in the size and shape of the nanoparticle (size less than 4 minutes film) which give rise to more than one plasmonic peaks (*section 3.3, chapter 3*). The absorption peaks around 1.70 ± 0.04 and 1.89 ± 0.03 eV of this film (*table 3.2*) lying close to the energy of incident laser beam, (1.96 eV for 632.8 nm) result in enhanced absorption, thereby increased in local heating resulting in generation of more hot electron and hence enhancement in the NLR coefficient.

The value of the NLR coefficient for 8 minutes duration deposited films increases with the annealing temperature. While the size distribution of the nanoparticles for as-deposited and annealed to a final temperature of 400°C was almost similar (*section 3.2, chapter 3*). In this case, annealing modified the electron distribution near the Fermi energy level and also changed the percentage of the constituent species rather than size and shape of the nanoparticles as confirmed by the activation energy and SE analysis (*section 3.2 and 3.4* respectively). The size of the nanoparticles in this film is ~ 38 nm, less than that of 4 and 6 minutes deposited films and thus the 8 minutes duration film possess large electron density, resulting in higher NLR coefficient [40]. Moreover, the 8 minutes duration as-deposited RT film displayed self-affine surface and which was further improved on gradual annealing as observed from fractal analysis (*section 3.2.2, chapter 3*). The self-affine fractal surfaces exhibits better NLO properties [37, 38]. Hence the film deposited for 8 minutes duration exhibited better NLO behaviour compared to that of deposited for 4 and 6 minutes as shown in *figure 5.3 (b).*

None of these above samples (a total of 15, *chapter 2*) showed any nonlinear absorption. It could be due to the shape and size of the metal nanoparticles and polarization

direction of the incident probe beam which has been reported in the literature [26, 41, 42]. For the films finally annealed to temperature of 400°C, the shape of the nanoparticle was conical with broad base (*section 3.2, chapter 3*) and showed longitudinal as well as transverse SPR (*section 3.3, chapter 3*). The transverse mode of SPR is responsible for RSA while the longitudinal mode of SPR is responsible for SA. The incident laser wavelength lying in between both these SPR peaks result into the SA as well as RSA, thus cancelling out the overall NLA [26].

5.4 Effect of particle size on the third order NLA and NLR coefficients of PLD nanostructured Cu thin films deposited at a substrate temperature of 400°C

The best SPR and NLO properties were observed at annealing temperature of 400ºC. Therefore another set of films was fabricated at 400ºC directly as described in section 2.1, chapter 2. All these films exhibited the SPR properties as discussed in detail, *section 4.4, chapter 4*. *Figure (5.4)* and *(5.5)* exhibit the OA and CA Z-scan spectra, respectively, for the Cu thin films deposited for 5 to 10 minutes duration via PLD at 400°C and annealed further at 400°C for 120 minutes. The nonlinear absorption coefficient, β and nonlinear refractive index coefficient, n_2, were estimated from the Z-scan data using the *equations (5.1)* and *(5.2)* respectively. The required linear refractive index '*n*' and linear absorption coefficient 'α' were obtained from the spectroscopic ellipsometric (SE) measurement and are listed in *table 5.2* at a wavelength of 632.8 nm. The estimated values of NLA and NLR coefficients are also listed in *table 5.2*. The change in the NLA and NLR coefficients as a function of particle size (or deposition time) are shown in figure *(5.6)* and *(5.7)* respectively. Unlike gradually annealed films deposited at RT, the films deposited directly around the glass softening temperature of 400ºC exhibited SA behaviour except the one deposited at 5 minutes. The Cu film deposited directly at 400°C for 5 minutes duration exhibited RSA (*figure 5.4*). As already mentioned, the magnitude of NLA depends

on the shape and size of nanoparticles, surface morphology, SPR peak position, intensity and the wavelength of the incident laser beam. In this set of films, the shape of the nanoparticles is nearly spherical (*section 4.3, chapter 4*) and exhibited only the longitudinal mode of SPR having energy below (*table 4.3, section 4.5.2, chapter 4*) the incident photon energy (~1.96 eV) of He:Ne laser. The film deposited for the duration of 5 minutes exhibited RSA because the longitudinal SPR peak lies near ~1.45 eV (855 nm) which is far from the energy of the incident laser beam (~1.96 eV). Moreover, the average particle size for 5 minutes deposited film was less than 20 nm, so, both the intraband and interband contributions are dominant compared to that of hot electron formation [26, 28] and hence it displayed the RSA behaviour.

All the other films from 6 to 10 minutes having SPR peaks around the wavelength of the incident laser beam, exhibited the SA behaviour. The value of the nonlinear absorption coefficient initially increased from 11.03 to 68.95 cm/W with the increase in size of nanoparticles from ~12 to 16 nm (deposition time from 5 to 7 minutes) then there was a marginal fall down in its values, 62.33 and 61.62 cm/W for the film deposited for 8 and 9 minutes duration respectively. Finally for the film having average particle size of 26 nm (deposition for 10 minutes duration), there is a drastic fall in the value of β to 26.47 cm/W. This behaviour could be due to the tuning of the gap of electronic intraband and interband which increases with decrease in the size of the nanoparticles; an increase in the gap between the bands decreases the absorption probability (linear and nonlinear) of the material [27, 28]. Also, the smaller size can increase the scattering probability on the surface electron of the nanoparticle and subsequently reduces the absorption probability which decreases the NLA coefficient [42]. But for the particle size ~26 nm, the contribution due to intraband and interband transition was less as well as more off resonant SPR peak

(~1.48 eV (833 nm)) to that of incident laser beam hence the value of NLA coefficient was decreased.

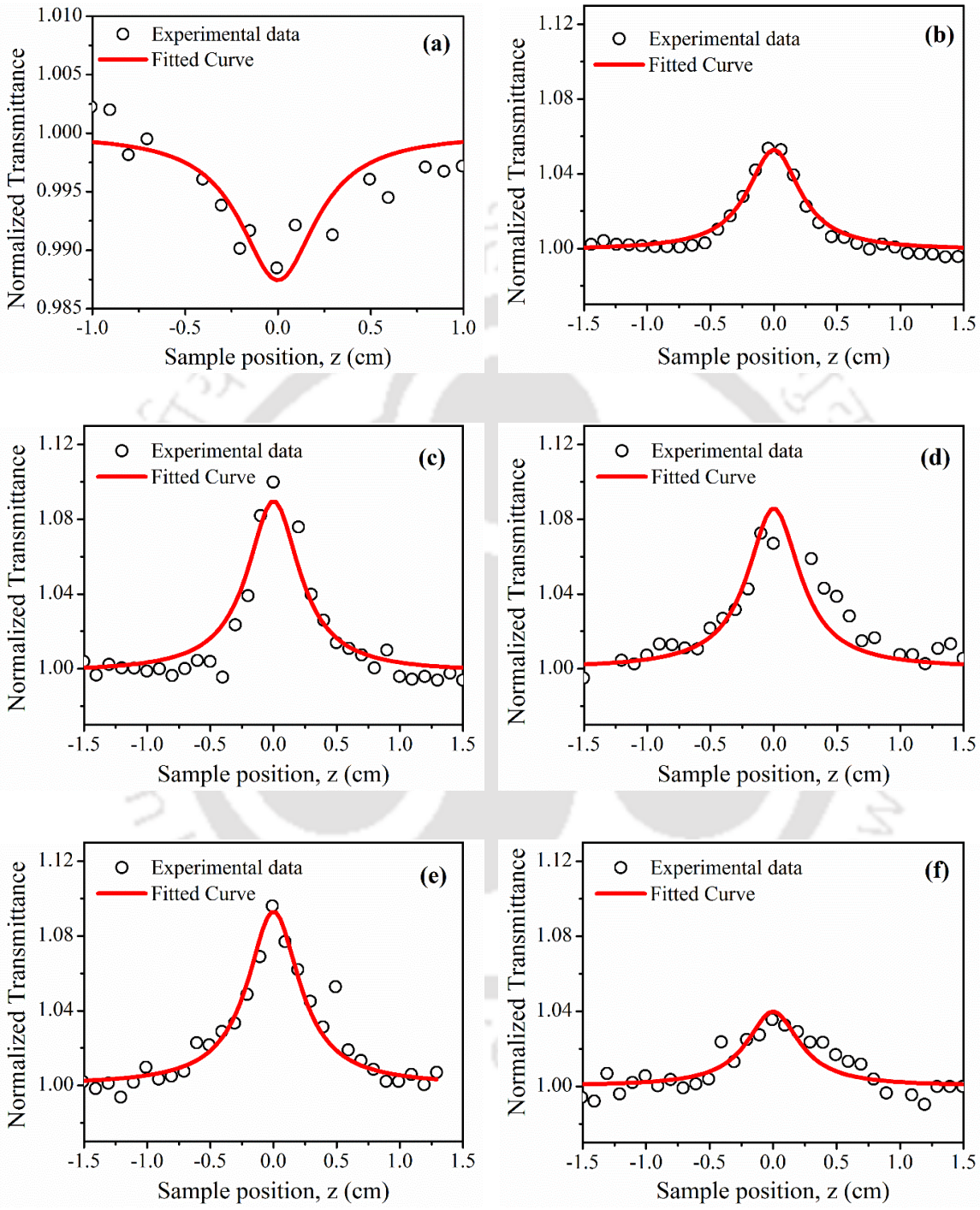

***Figure 5.4**: OA Z-scan normalized transmittance curve of nanostructure Cu thin films deposited at 400°C for the deposition time of (a) 5 minutes, (b) 6 minutes, (c) 7 minutes (d) 8 minutes (e) 9 minutes and (f) 10 minutes.*

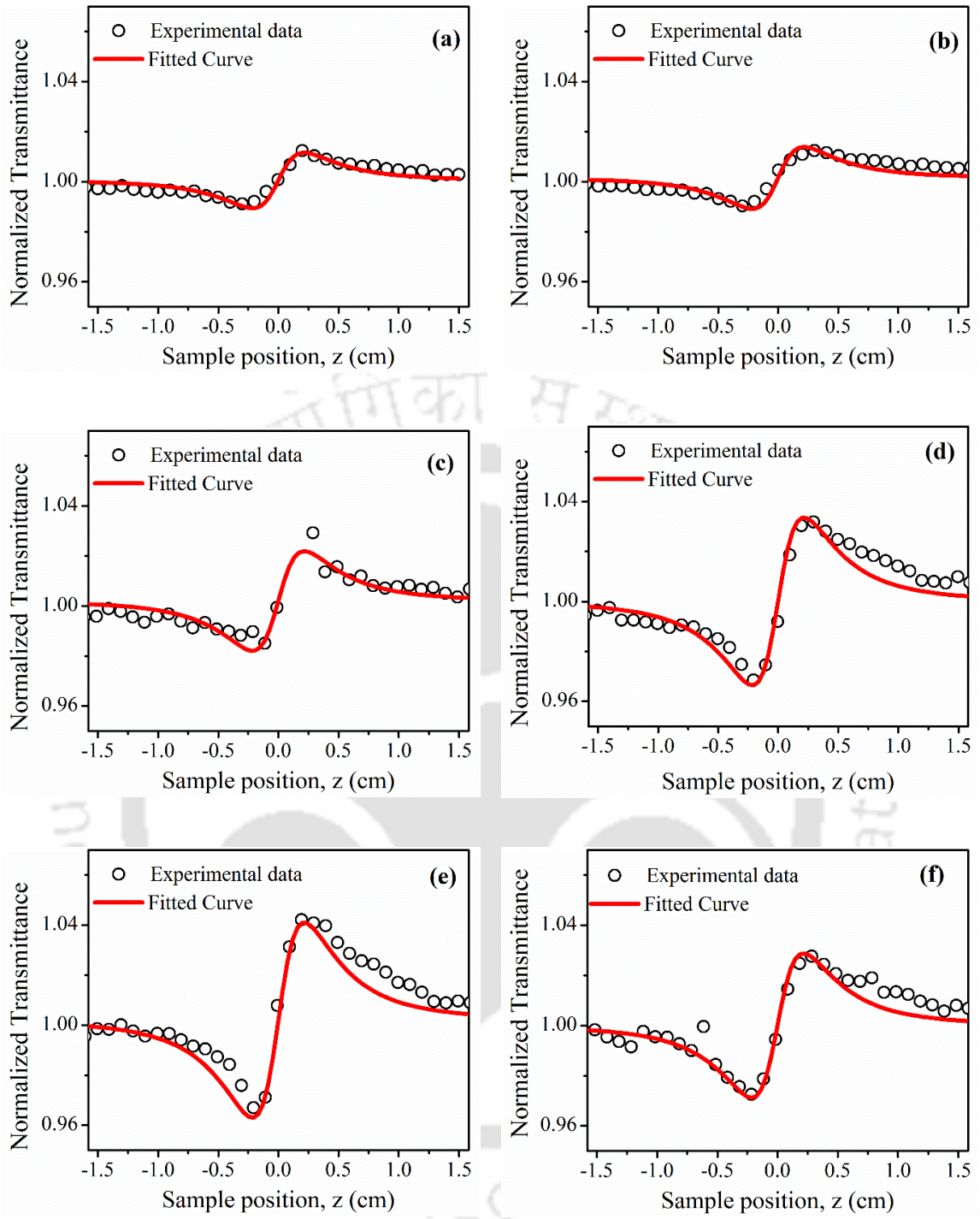

***Figure 5.5**: CA Z-scan normalized transmittance curve of nanostructure Cu thin films deposited at 400°C for the deposition time of (a) 5 minutes, (b) 6 minutes, (c) 7 minutes (d) 8 minutes (e) 9 minutes and (f) 10 minutes.*

Moreover, the amount of hot electrons slowly increases with increasing in the size of the metal nanoparticle but simultaneously decreases the energy efficiency of these hot electrons

[29]. Hence the NLO coefficient is decreased as reflected in our result.

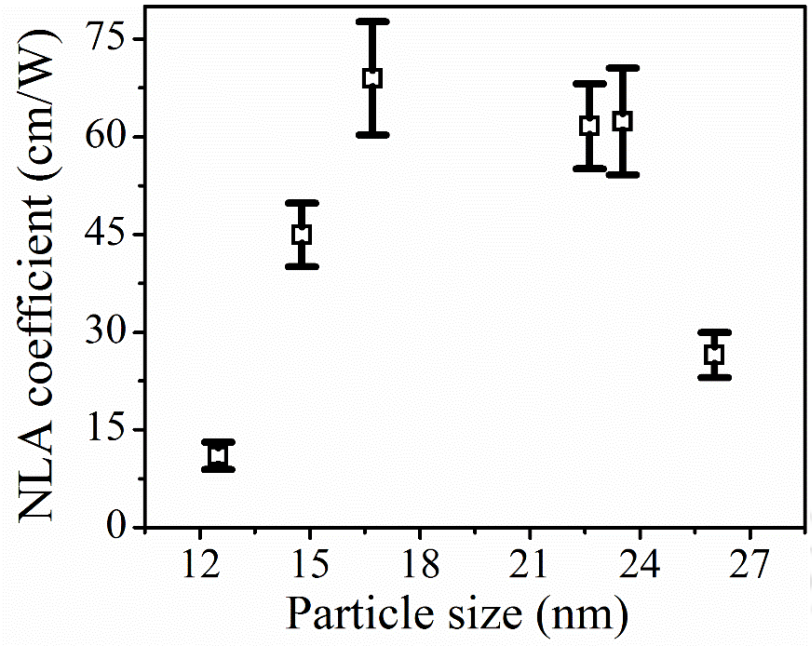

***Figure 5.6**: NLA coefficient of PLD deposited nanostructured Cu thin film at 400°C as a function of particle size.*

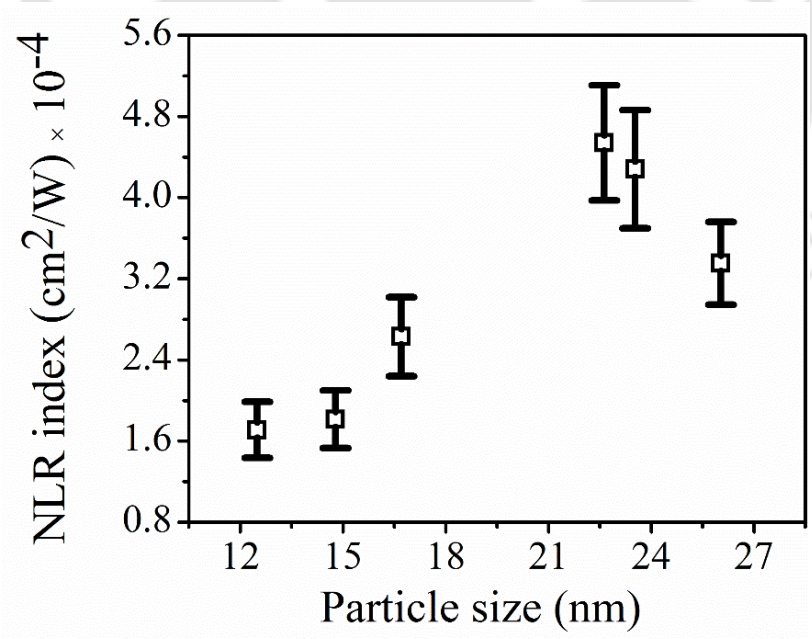

***Figure 5.7**: NLR coefficient of PLD deposited nanostructured Cu thin film at 400°C as a function of particle size.*

***Table 5.2**: List of linear and nonlinear optical constants of Cu thin metal film.*

Deposition time (minutes)	Average particle size (nm)	Linear absorption (α cm^{-1}) × 10^5	n_o (at 632.8 nm)	NLA coefficient (β cm/W)	NLA coefficient (n_2 cm^2/W) × 10^{-4}
5	12	1.56	2.85	11.03±2.10 (RSA)	1.71±0.22
6	14	2.34	2.48	44.94±4.88 (SA)	1.81±0.28
7	16	2.20	2.30	68.94±8.67 (SA)	2.63±0.39
8	23	2.28	2.35	62.33±8.19 (SA)	4.28±0.58
9	23	2.17	2.27	61.62±6.53 (SA)	4.53±0.56
10	26	2.50	2.38	26.47±3.50 (SA)	3.35±0.40

All the Cu films deposited at 400°C exhibited self-focusing behaviour corresponding to positive n_2. The n_2 of Cu thin films was increased from 1.71×10^{-4} to 4.54×10^{-4} cm^2/W with the size of the nanoparticles from 12 to 23 nm, but for larger sized nanoparticles 26 nm, it was decreased slightly to 3.35×10^{-4} cm^2/W as shown in *figure 5.7*.

5.5 Conclusions

The effect of annealing temperature, substrate temperature and particle size on the third order NLO property of PLD nanostructured Cu thin films is presented in this chapter. The NLR and NLA coefficients of PLD Cu thin films were measured by modified *Z*-scan technique under cw He-Ne laser irradiation. A cw-laser was used, therefore optical nonlinearity induced in the films is dominated by hot electron formation due to the laser heating. The films deposited at RT did not show any optical nonlinearity. The value of NLR coefficient (n_2) was observed to be increased with increase in the annealing temperature from 100ºC to 400ºC. The films annealed to a final temperature of 400ºC possessed self-affine surface, showed large NLR coefficient and it increases with the deposition time. The CA *Z*-scan curves showed valley–peak signature indicating the self-focusing property,

positive nonlinear refractive index coefficient. The value of n_2 was of the order of ~10^{-4} cm^2/W in all the cases. The gradual annealed film didn't display any NLA. The films deposited directly at 400ºC showed both NLA and NLR. In this case, NLA coefficient increases with the particle size initially, attain a maximum value of 68.94 cm/W for a particle size of ~16 nm and then it falls down with further increases in particle size.

Bibliography

[1] M. Kauranen, A.V. Zayats, Nonlinear plasmonics, Nature Photonics, 6 (2012) 737.

[2] Y.-x. Zhang, Y.-h. Wang, Nonlinear optical properties of metal nanoparticles: a review, RSC Advances, 7 (2017) 45129-45144.

[3] C. Min, P. Wang, C. Chen, Y. Deng, Y. Lu, H. Ming, T. Ning, Y. Zhou, G. Yang, All-optical switching in subwavelength metallic grating structure containing nonlinear optical materials, Optics letters, 33 (2008) 869-871.

[4] T. Jiang, Z. Kang, G. Qin, J. Zhou, W. Qin, Low mode-locking threshold induced by surface plasmon field enhancement of gold nanoparticles, Optics Express, 21 (2013) 27992-28000.

[5] B. Karthikeyan, M. Anija, C.S.S. Sandeep, T.M.M. Nadeer, R. Philip, Optical and nonlinear optical properties of copper nanocomposite glasses annealed near the glass softening temperature, Optics Communications, 281 (2008) 2933-2937.

[6] R. Udayabhaskar, M.S. Ollakkan, B. Karthikeyan, Preparation, optical and non-linear optical power limiting properties of Cu, CuNi nanowires, Applied Physics Letters, 104 (2014) 013107.

[7] T. Schumacher, K. Kratzer, D. Molnar, M. Hentschel, H. Giessen, M. Lippitz, Nanoantenna-enhanced ultrafast nonlinear spectroscopy of a single gold nanoparticle, Nature communications, 2 (2011) 333.

[8] N.C. Panoiu, W.E.I. Sha, D.Y. Lei, G.C. Li, Nonlinear optics in plasmonic nanostructures, Journal of Optics, 20 (2018) 083001.

[9] L. Caspani, C. Xiong, B.J. Eggleton, D. Bajoni, M. Liscidini, M. Galli, R. Morandotti, D.J. Moss, Integrated sources of photon quantum states based on nonlinear optics, Light: Science & Applications, 6 (2017) e17100.

[10] F.X. Wang, F.J. Rodríguez, W.M. Albers, R. Ahorinta, J.E. Sipe, M. Kauranen, Surface and bulk contributions to the second-order nonlinear optical response of a gold film, Physical Review B, 80 (2009) 233402.

[11] S.A. Zolotovskaya, M.A. Tyrk, A. Stalmashonak, W.A. Gillespie, A. Abdolvand, On second harmonic generation and multiphoton-absorption induced luminescence from laser-reshaped silver nanoparticles embedded in glass, Nanotechnology, 27 (2016) 435703.

[12] M. Chandra, P.K. Das, Size dependence and dispersion behavior of the first hyperpolarizability of copper nanoparticles, Chemical Physics Letters, 476 (2009) 62-64.

[13] M. Lippitz, M.A. van Dijk, M. Orrit, Third-harmonic generation from single gold nanoparticles, Nano letters, 5 (2005) 799-802.

[14] R. Kesarwani, A. Khare, Surface plasmon resonance and nonlinear optical behavior of pulsed laser-deposited semitransparent nanostructured copper thin films, Applied Physics B, 124 (2018) 116.

[15] A.I. Ryasnyanskiy, B. Palpant, S. Debrus, U. Pal, A. Stepanov, Third-order nonlinear-optical parameters of gold nanoparticles in different matrices, Journal of luminescence, 127 (2007) 181-185.

[16] D.W. Forslund, J.M. Kindel, E.L. Lindman, Theory of stimulated scattering processes in laser-irradiated plasmas, The Physics of Fluids, 18 (1975) 1002-1016.

[17] S.S. Kharintsev, A.V. Kharitonov, S.K. Saikin, A.M. Alekseev, S.G. Kazarian, Nonlinear Raman Effects Enhanced by Surface Plasmon Excitation in Planar Refractory Nanoantennas, Nano letters, 17 (2017) 5533-5539.

[18] X.L. Yu, C.B. Cao, H.S. Zhu, Q.S. Li, C.L. Liu, Q.H. Gong, Nanometer-Sized Copper Sulfide Hollow Spheres with Strong Optical-Limiting Properties, Advanced Functional Materials, 17 (2007) 1397-1401.

[19] R.W. Boyd, Nonlinear optics, Elsevier, 2003.

[20] A.R. Sadrolhosseini, S.A. Rashid, H. Shojanazeri, A.S.M. Noor, H. Nezakati, Spatial self-phase modulation patterns in graphene oxide and graphene oxide with silver and gold nanoparticles, Optical and Quantum Electronics, 48 (2016) 222.

[21] J.Z. Anvari, R. Karimzadeh, N. Mansour, Thermo-optic properties and nonlinear responses of copper nanoparticles in polysiloxane oil, Journal of Optics, 12 (2010) 035212.

[22] A.R. Sadrolhosseini, A.S.B.M. Noor, K. Shameli, G. Mamdoohi, M.M. Moksin, M.A. Mahdi, Laser ablation synthesis and optical properties of copper nanoparticles, Journal of Materials Research, 28 (2013) 2629-2636.

[23] R. Noskov, P. Belov, Y. Kivshar, Oscillons, solitons, and domain walls in arrays of nonlinear plasmonic nanoparticles, Scientific reports, 2 (2012) 873.

[24] J. Renger, R. Quidant, N. Van Hulst, L. Novotny, Surface-enhanced nonlinear four-wave mixing, Physical review letters, 104 (2010) 046803.

[25] Y. Wang, C.-Y. Lin, A. Nikolaenko, V. Raghunathan, E.O. Potma, Four-wave mixing microscopy of nanostructures, Advances in optics and photonics, 3 (2011) 1-52.

[26] S. Mohan, Third-order optical nonlinearities of glass-metal nanocomposites, (2011).

[27] B. Balamurugan, T. Maruyama, Size-modified d bands and associated interband absorption of Ag nanoparticles, Journal of applied physics, 102 (2007) 034306.

[28] Y. Gao, D. Kong, Nonlinear Optical Response of Noble Metal Nanoparticles, in: Laser Technology and its Applications, IntechOpen, 2018.

[29] G.V. Hartland, L.V. Besteiro, P. Johns, A.O. Govorov, What's so hot about electrons in metal nanoparticles?, ACS Energy Letters, 2 (2017) 1641-1653.

[30] D. Compton, L. Cornish, E. van der Lingen, The third order nonlinear optical properties of gold nanoparticles in glasses, part I, Gold Bulletin, 36 (2003) 10-16.

[31] F. Hache, D. Ricard, C. Flytzanis, U. Kreibig, The optical Kerr effect in small metal particles and metal colloids: the case of gold, Applied Physics A, 47 (1988) 347-357.

[32] I. Kumar, A. Khare, Modified Z-scan set-up using CCD for measurement of optical nonlinearity in PLD carbon thin film, Optics & Laser Technology, 77 (2016) 51-54.

[33] G.P. Bharti, A. Khare, Structural and linear and nonlinear optical properties of Zn 1-x Al x O ($0 \leq x \leq 0.10$) thin films fabricated via pulsed laser deposition technique, Opt. Mater. Express, 6 (2016) 2063-2080.

[34] J.T. Luxon, D.E. Parker, J. Karkheck, Waist location and Rayleigh range for higher-order mode laser beams, Applied optics, 23 (1984) 2088-2090.

[35] S. Kumar, A. Sood, Ultrafast Response of Plasmonic Nanostructures, in: Reviews in Plasmonics 2015, Springer, 2016, pp. 131-167.

[36] M. Bache, A.V. Lavrinenko, Ultrafast nonlinear dynamics of thin gold films due to an intrinsic delayed nonlinearity, Journal of Optics, 19 (2017) 094004.

[37] V.M. Shalaev, V.A. Markel, E.Y. Poliakov, R.L. Armstrong, V.P. Safonov, A.K. Sarychev, Nonlinear optical phenomena in nanostructured fractal materials, Journal of Nonlinear Optical Physics & Materials, 7 (1998) 131-152.

[38] V.M. Shalaev, R. Botet, J. Mercer, E.B. Stechel, Optical properties of self-affine thin films, Physical Review B, 54 (1996) 8235.

[39] F.L.S.A. Cuppo, A.M.F. Neto, S.L. Go ´mez, P. Palffy-Muhoray, Thermal-Lens Model Compared with the Sheik-Bahae Formalism in Interpreting Z-Scan Experiments on Lyotropic Liquid Crystals, (2002).

[40] Y. Fu, R.A. Ganeev, P.S. Krishnendu, C. Zhou, K.S. Rao, C. Guo, Size-dependent off-resonant nonlinear optical properties of gold nanoparticles and demonstration of efficient optical limiting, Opt. Mater. Express, 9 (2019) 976-991.

[41] O. Sanchez-Dena, P. Mota-Santiago, L. Tamayo-Rivera, E.V. García-Ramírez, A. Crespo-Sosa, A. Oliver, J.-A. Reyes-Esqueda, Size-and shape-dependent nonlinear optical response of Au nanoparticles embedded in sapphire, Opt. Mater. Express, 4 (2014) 92-100.

[42] Y. Hua, K. Chandra, D.H.M. Dam, G.P. Wiederrecht, T.W. Odom, Shape-dependent nonlinear optical properties of anisotropic gold nanoparticles, The journal of physical chemistry letters, 6 (2015) 4904-4908.

Chapter 6

PLD Cu thin films as a viable SERS substrate for carbon nanotubes

Nanostructured metallic plasmonic thin films, are gaining importance due to variety of applications as described in pervious chapters. Surface enhanced Raman scattering (SERS) is the one of the very important application based on SPs particularly for molecules possessing weak Raman signals or are in trace quantities [1]. Strongly enhanced Raman signals have been documented for the molecules interacting with metallic nanoparticles and this phenomena is known as SERS [2, 3]. The enhancement in the Raman spectrum of the molecules interacting with the metallic nanoparticles, is attributed to either of the two phenomenon (i) Electromagnetic SERS (EM-SERS) effect, which is due to the resonant interaction between optical fields and the electronic excitations in the metallic nanostructures and (ii) Chemical SERS effect, which is due to the interaction between the molecules and metal surfaces [4-6]. SERS is strongly influenced by the surface morphology of the metallic film being used as SERS substrate. The flat surface of the metallic film is not suitable to enhance the Raman signal [7, 8]. Apart from surface morphology, the SERS depends on the type of substrate on which metal nanoparticles are grown as well as on its, size and shape [9-11].

In the present chapter, the plasmonic interaction of copper (Cu) nanoparticles with metallic single wall carbon nanotube (M-SWCNT) for SERS is reported. SWCNTs, is referred to the carbon nanotubes (CNTs) having diameters ranging from 0.7 nm to 2 nm. Depending on the diameter and chirality, the SWCNT may be either metallic or semiconducting in nature [12]. Samples enriched in metallic SWCNTs (M-SWCNTs), are

inherently more useful for the development of efficient plasmonic devices [13, 14]. Recently, the researchers have experimentally reported the observation of Luttinger-liquid plasmon phenomena in M-SWCNT [15]. The hybrid CNT-Cu composite material shows 1000 times higher conductivity than that of pristine nanotubes whereas the ampacity is found to be 100 times higher than that of pure Cu [16]. CNT-Cu composite has been shown to be of great potential in fabrication of faster electro-optical switches and electronic inks with high conductivity [17]. The characteristic Raman bands of SWCNT; radial breathing mode (RBM), D, G and G´ are highly sensitive to small changes in the electronic nature of the nanotubes [18, 19]. Thus, the presence of metallic nanoparticles in the vicinity of SWCNT enhances drastically the Raman signal via plasmonic interaction [20].

The effect of substrate on the SERS properties of Cu thin film was also presented in this chapter. For this, PLD Cu thin films were deposited on to the glass as well as on the silicon (Si) substrate at room temperature (RT) and 400°C to act as the SERS substrate for M-SWCNT. The SERS signals for all the prominent bands; RBM, D, G and G´ bands are detailed in this chapter.

6.1 Experimental details

The five samples; three on glass and remaining two on Si, were prepared to study the efficacy of Cu thin film for SERS. The detailed configuration of these samples are illustrated in *chapter 2, section 2.3, figure 2.7* and is repeated in *figure 6.1* for quick recall. For the comparison, the drop casted M-SWCNT on bare glass as well as on Si substrate was annealed at 400°C. Raman spectra of all the samples were recorded using laser micro Raman spectrometer operating at a wavelength of 514 nm of Ar ion laser. The sample was probed at four different locations.

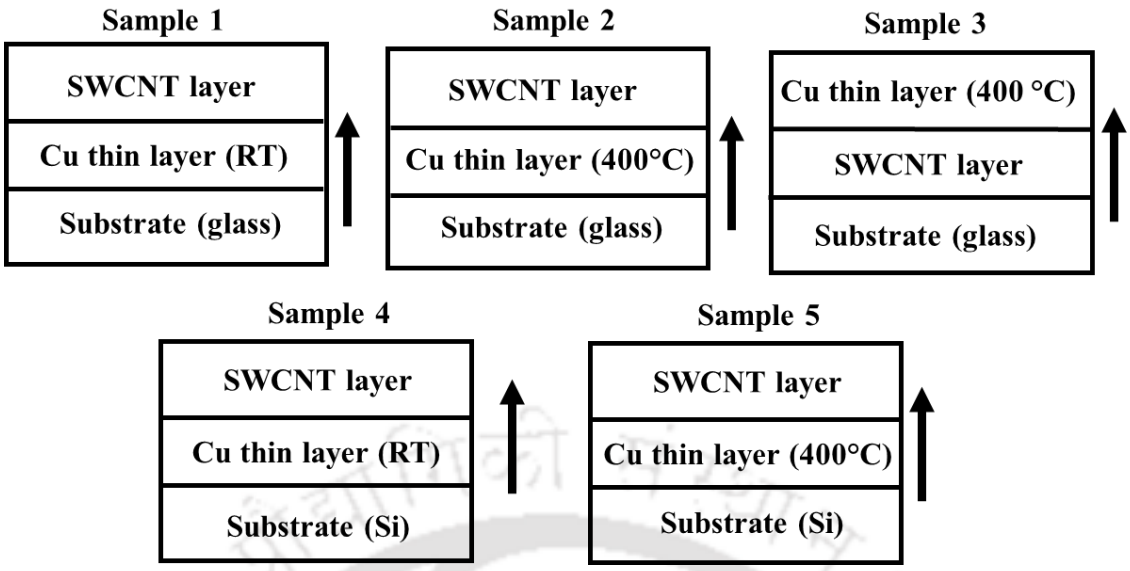

***Figure 6.1**: Schematic of SERS samples on glass and Si substrate.*

6.2 Surface enhanced Raman scattering from the carbon nanotubes interacting with Cu nanoparticles on glass substrate

Figure 6.2 (a), (b) and *(c)* exhibit the Raman spectra of the M-SWCNT for samples 1, 2 and 3 respectively prepared on PLD Cu thin film at RT and 400°C. In all the three cases the four Raman bands; RBM, D, G and G´ bands around at 160-190 cm^{-1}, 1300-1400 cm^{-1}, 1550-1600 cm^{-1} and 2600-2700 cm^{-1} respectively are clearly observed and labelled in the *figure 6.2. Figure 6.2 (d)* shows the comparison of the intensity of Raman signal for samples 1 and 2 along with the bare M-SWCNT on glass substrate (without Cu). A significant enhancement is observed in the Raman signals from sample 2 as compared to that of sample 1 with respect to the M-SWCNT on bare glass substrate. However, there is no enhancement in the Raman signal of sample 3 with respect to the M-SWCNT on bare glass substrate. In the present case, observed SERS effect on metal coated substrate (sample 1 and 2) is influenced by SPs due to the presence of Cu nanoparticles and is attributed to the EM-SERS [5]. The Cu film deposited at elevated temperature exhibit the pronounced plasmonic properties compared to that of RT as illustrated in *chapter 3 and 4*.

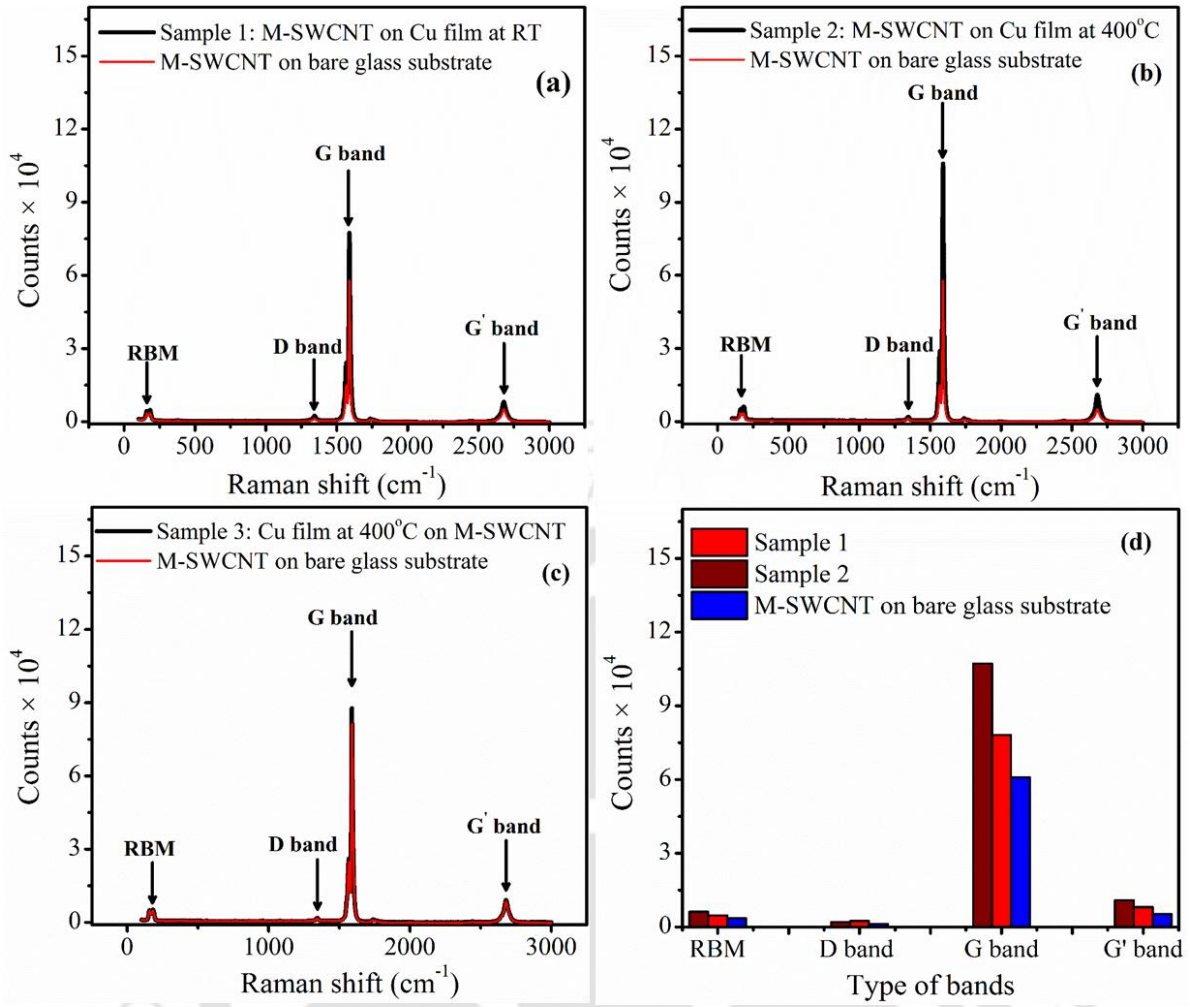

Figure 6.2*: Raman spectra of (a) Sample 1, (b) Sample 2, (c) Sample 3 and (d) comparison of the intensity of RBM, D, G and G´bands of M-SWCNT for sample 1 and 2.*

Thus the Raman enhancement factor is more in sample 2 as compared to that of sample 1. *Figure 6.3 (a-c)* portrait the enlarged view of RBM, G, and G´ band for sample 1 as well as sample 2. The percentage enhancement in Raman signal of these bands is shown in *figure 6.3 (d)*. The RBM band, in sample 2 exhibits nearly 70% increase in the intensities. The other bands, D, G and G´bands are enhanced more than 80% as shown in *figure 6.3 (d)*. *Figure 6.4* shows the comparison of sample 2 and 3. The enhancement in sample 3 for the three Raman bands of M-SWCNT is much lower compared to that of the sample 2. Histogram in the *figure 6.4 (d)* compares the relative enhancement in the individual peaks of sample 2 and 3. The first three bands; RBM, D and G band, in sample

2 exhibit more than 90% increase in the intensities whereas G´ band has undergone nearly 120% enhancement, *figure 6.4 (d)*.

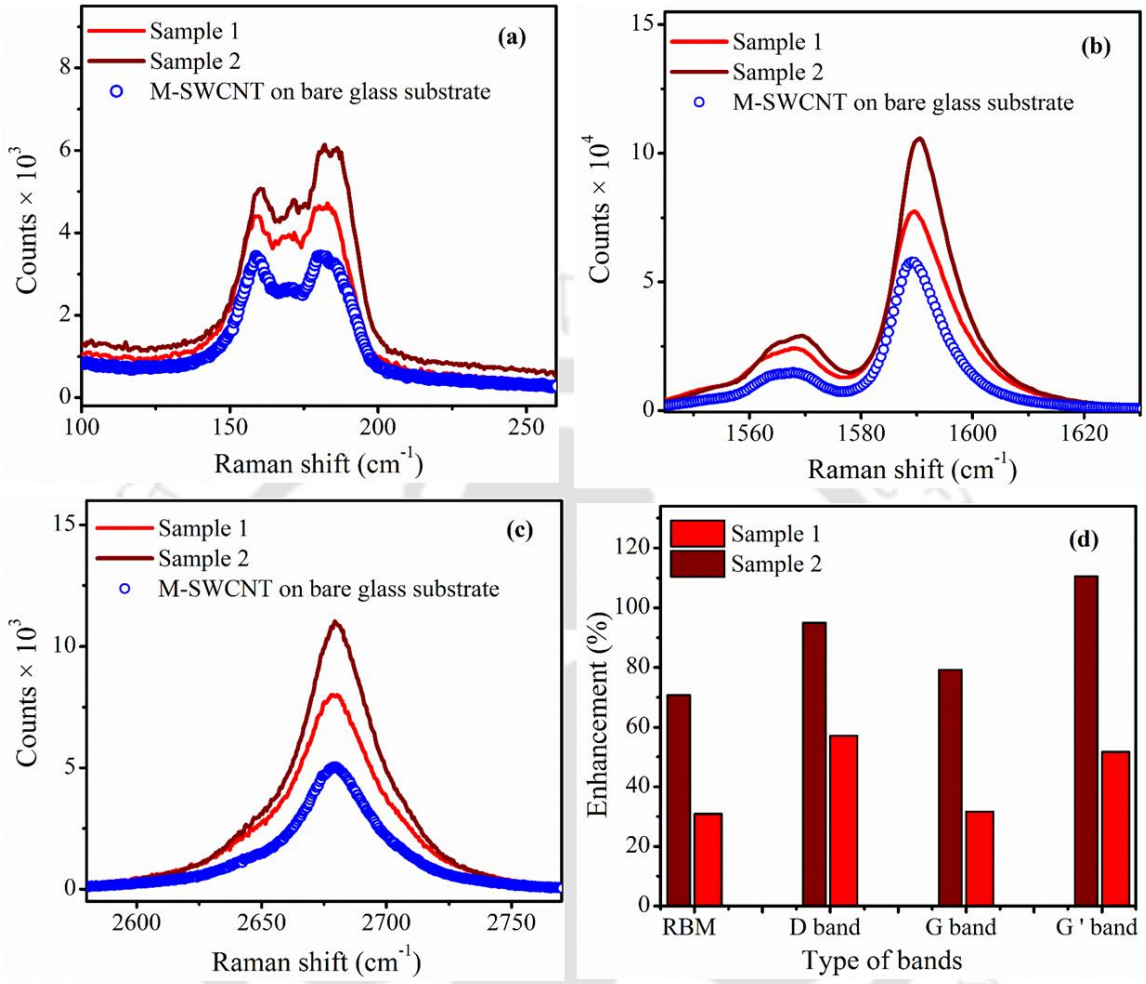

Figure 6.3*: Comparison of the intensities of each Raman modes in sample 1 and sample 2; (a) RBM, (b) G band, (c) G' band respectively and (d) the percentage enhancement in the individual peaks.*

The G´ band of SWCNTs is very sensitive to the charge transfer and it exhibits the red or blue shift depending on electronic interaction and mechanical strain on the SWCNTs in presence of the functional nanoparticles [21, 22]. In the sample 2, the G' band undergoes a blue shift of ~2 cm^{-1}, further indicating strong interaction and plasmonic coupling between the copper nanoparticles and M-SWCNTs. The red shift in its G' band is ~ 0.4 cm^{-1} in sample 3, indicates the M-SWCNT is under stress which could be due to the formation

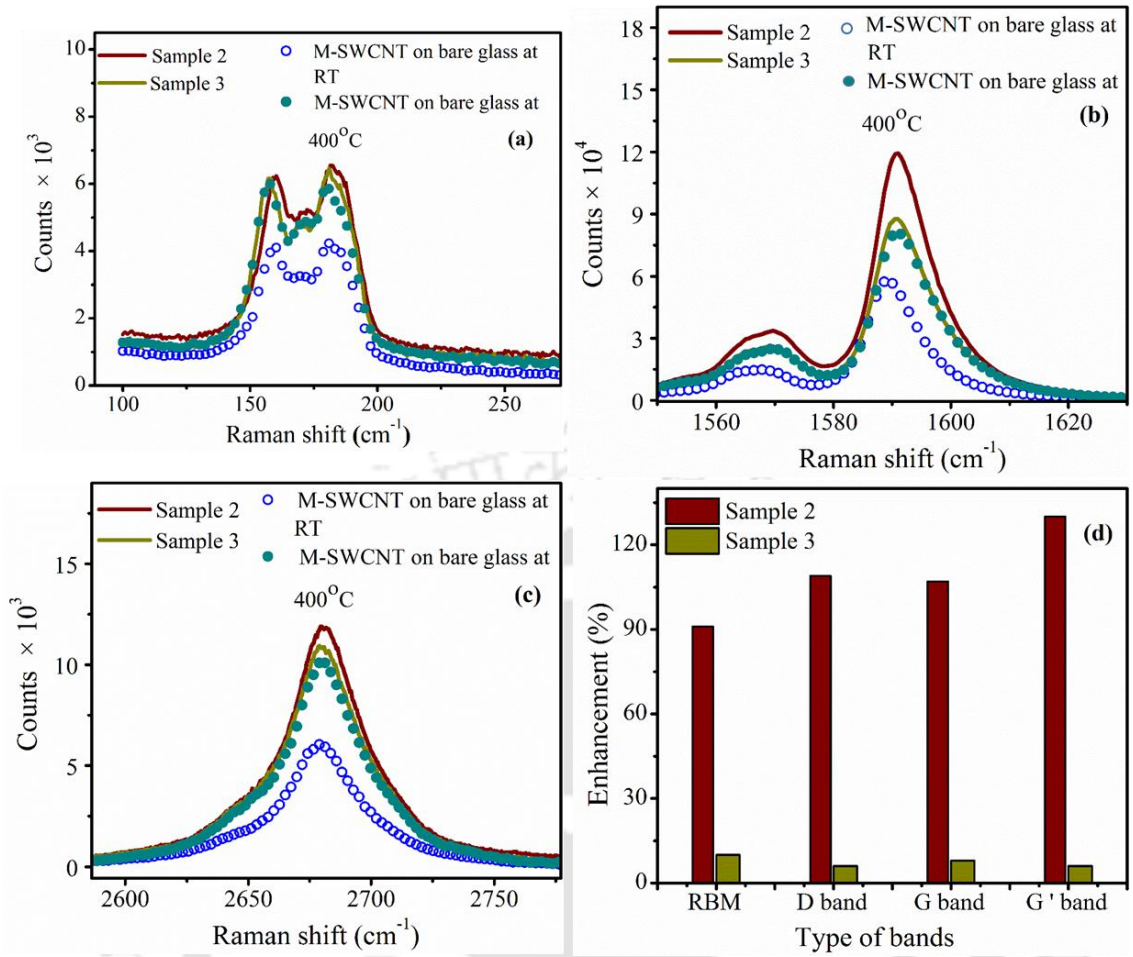

***Figure 6.4**: Comparison of intensities of each Raman modes in sample 2 and 3. (a) RBM, (b) G band, (c) G´ band respectively and (d) the percentage enhancement in the individual peaks.*

of Cu layer above the SWCNT in sample 3. Finally, it is concluded that the sample 2 is the best configuration for the Raman enhancement of the M-SWCNT compared to that of sample 1 and 3. The RBM peaks of sample 2 were fitted with the multiple Lorentzian function and resulted into five distinguished peaks at 156 cm^{-1}, 160 cm^{-1}, 170 cm^{-1}, 180 cm^{-1} and 188 cm^{-1} respectively. The corresponding diameter of the M-SWCNT can be obtained from the relation [12] $\omega_{RBM} = 234/d'' + 10$, where ω_{RBM} is Raman shift of RBM band and d'' is the diameter of M-SWCNT, and is found to be in the range of 1.38 nm to 1.60 nm.

6.3 Surface enhanced Raman scattering from the carbon nanotubes interacting with Cu nanoparticles on Si substrate

To study the effect of substrate, two more samples were prepared on Si substrate while keeping rest of the parameters same. *Figure 6.5 (a)* and *(b)* exhibit the Raman spectra of the M-SWCNT for sample 4 and 5 respectively prepared on PLD Cu thin film at RT and 400°C respectively.

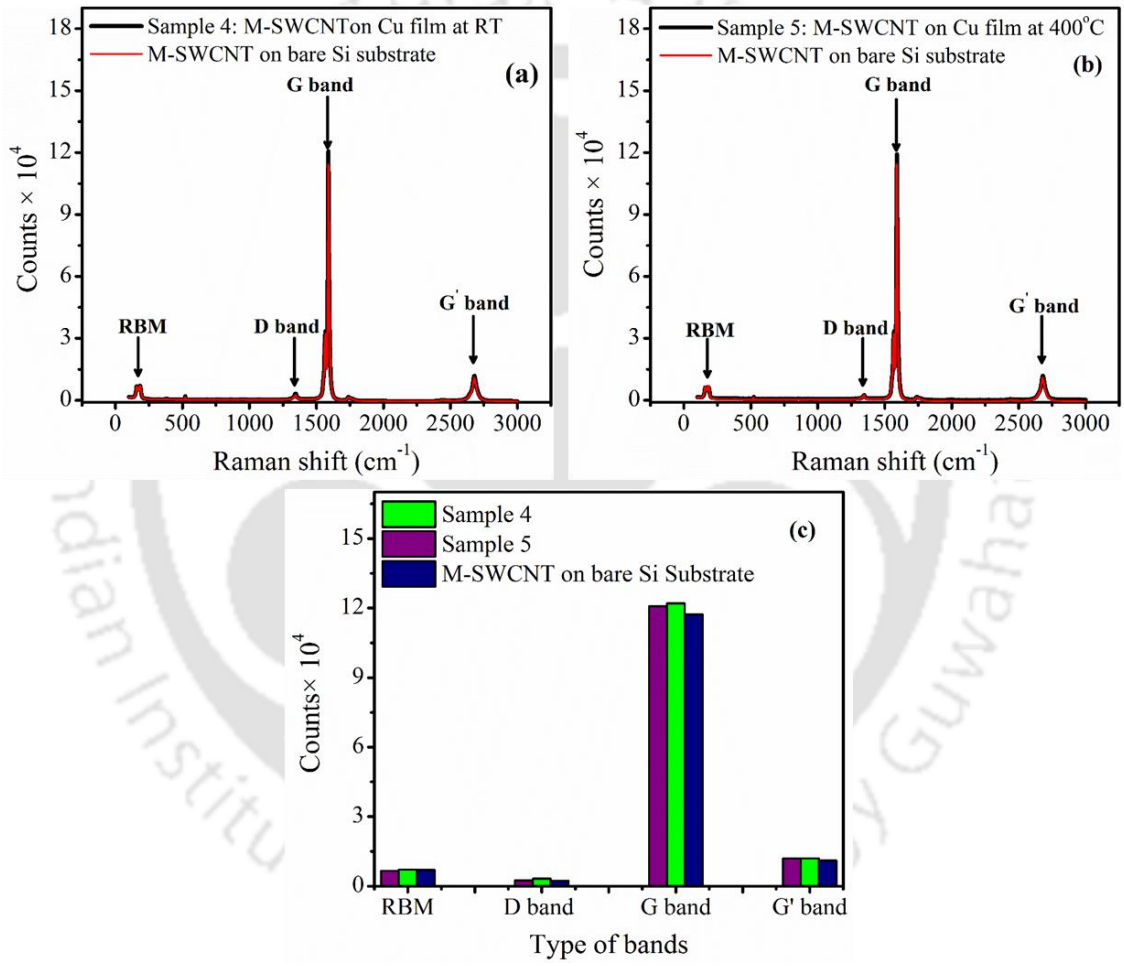

Figure 6.5*: Raman spectra of (a) Sample 4, (b) Sample 5 and (c) RBM, D, G and G′ bands of M-SWCNT for sample 4 and 5.*

All the Raman bands; RBM, D, G and G´ band at 160-190 cm^{-1}, 1300-1400 cm^{-1}, 1550-1600 cm^{-1} and 2600-2700 cm^{-1} respectively are clearly observed and are labelled in the *figure 6.5. Figure 6.5 (c)* shows the comparison of the intensity of Raman signal for

samples 4 and 5 along with the bare M-SWCNT on Si. It was observed that there is no significant enhancement in the Raman intensity with respect to the M-SWCNT on the bare Si substrate. Hence, it is concluded that the Cu film deposited on Si is not a viable substrate for SERS.

6.4 Conclusions

SERS samples were fabricated in five different configurations for identifying the best suitable SERS substrate. The enhancement in the Raman signal was maximum for sample 2 in which Cu film was deposited at 400ºC via PLD and then M-SWCNT was drop casted on it. Blue shift in G´ band in this film further confirms the strong plasmonic interaction between the copper nanoparticles and M-SWCNTs. There is no significant enhancement in the Raman signal for M-SWCNT on Cu coated Si substrate. Thus the PLD nanostructure Cu thin film on glass acts as a good SERS substrate. From the Raman shift of RBM peaks, the diameter of the SWCNT was found to be in the range of 1.38 nm to 1.68 nm.

Bibliography

[1] J. Zhang, L. Zhang, W. Xu, Surface plasmon polaritons: physics and applications, Journal of Physics D: Applied Physics, 45 (2012) 113001.

[2] G.C. Schatz, R.P. Van Duyne, Electromagnetic mechanism of surface-enhanced spectroscopy, Handbook of vibrational spectroscopy, (2006).

[3] B. Sharma, R.R. Frontiera, A.-I. Henry, E. Ringe, R.P. Van Duyne, SERS: Materials, applications, and the future, Materials Today, 15 (2012) 16-25.

[4] S.Y. Ding, X.M. Zhang, B. Ren, Z.Q. Tian, Surface-Enhanced Raman Spectroscopy (SERS): General Introduction, Encyclopedia of Analytical Chemistry: Applications, Theory and Instrumentation, (2006) 1-34.

[5] N. Guillot, M.L. de la Chapelle, The electromagnetic effect in surface enhanced Raman scattering: Enhancement optimization using precisely controlled nanostructures, Journal of Quantitative Spectroscopy and Radiative Transfer, 113 (2012) 2321-2333.

[6] A. Campion, J. Ivanecky III, C. Child, M. Foster, On the mechanism of chemical enhancement in surface-enhanced Raman scattering, Journal of the American Chemical Society, 117 (1995) 11807-11808.

[7] S. Kruszewskh, J. Skonieczny, Roughness effects in surface enhanced Raman scattering-evidence for electromagnetic and charge transfer enhancement mechanism, Acta Physica Polonica A, 4 (1991) 611-620.

[8] R. Panneerselvam, G.-K. Liu, Y.-H. Wang, J.-Y. Liu, S.-Y. Ding, J.-F. Li, D.-Y. Wu, Z.-Q. Tian, Surface-enhanced Raman spectroscopy: bottlenecks and future directions, Chemical Communications, 54 (2018) 10-25.

[9] D.M. Solís, J.M. Taboada, F. Obelleiro, L.M. Liz-Marzán, F.J. García de Abajo, Optimization of nanoparticle-based SERS substrates through large-scale realistic simulations, ACS photonics, 4 (2017) 329-337.

[10] S. Hong, X. Li, Optimal size of gold nanoparticles for surface-enhanced Raman spectroscopy under different conditions, Journal of nanomaterials, 2013 (2013) 49.

[11] N.D. Israelsen, C. Hanson, E. Vargis, Nanoparticle properties and synthesis effects on surface-enhanced Raman scattering enhancement factor: an introduction, The Scientific World Journal, 2015 (2015).

[12] M.S. Dresselhaus, G. Dresselhaus, R. Saito, A. Jorio, Raman spectroscopy of carbon nanotubes, Physics reports, 409 (2005) 47-99.

[13] Q. Zhang, E.H. Hároz, Z. Jin, L. Ren, X. Wang, R.S. Arvidson, A. Lüttge, J. Kono, Plasmonic nature of the terahertz conductivity peak in single-wall carbon nanotubes, Nano letters, 13 (2013) 5991-5996.

[14] Y. Battie, L. Broch, A.E. Naciri, J.-S. Lauret, M. Guézo, A. Loiseau, Diameter dependence of the optoelectronic properties of single walled carbon nanotubes determined by ellipsometry, Carbon, 83 (2015) 32-39.

[15] Z. Shi, X. Hong, H.A. Bechtel, B. Zeng, M.C. Martin, K. Watanabe, T. Taniguchi, Y.-R. Shen, F. Wang, Observation of a Luttinger-liquid plasmon in metallic single-walled carbon nanotubes, Nature Photonics, 9 (2015) 515.

[16] C. Subramaniam, T. Yamada, K. Kobashi, A. Sekiguchi, D.N. Futaba, M. Yumura, K. Hata, One hundred fold increase in current carrying capacity in a carbon nanotube–copper composite, Nature communications, 4 (2013) 2202.

[17] H.-J. Hwang, S.-J. Joo, H.-S. Kim, Copper nanoparticle/multiwalled carbon nanotube composite films with high electrical conductivity and fatigue resistance fabricated via flash light sintering, ACS applied materials & interfaces, 7 (2015) 25413-25423.

[18] L. Bokobza, J. Zhang, Raman spectroscopic characterization of multiwall carbon nanotubes and of composites, Express Polymer Letters, 6 (2012).

[19] A. Paipetis, Stress induced changes in the raman spectrum of carbon nanostructures and their composites, in: Carbon nanotube enhanced aerospace composite materials, Springer, 2013, pp. 185-217.

[20] S. Heeg, A. Oikonomou, R. Fernandez-Garcia, C. Lehmann, S.A. Maier, A. Vijayaraghavan, S. Reich, Plasmon-enhanced Raman scattering by carbon nanotubes optically coupled with near-field cavities, Nano letters, 14 (2014) 1762-1768.

[21] F. Wan, H. Shi, W. Chen, Z. Gu, L. Du, P. Wang, J. Wang, Y. Huang, Charge transfer effect on Raman and surface enhanced Raman spectroscopy of furfural molecules, Nanomaterials, 7 (2017) 210.

[22] M. Huang, H. Yan, T.F. Heinz, J. Hone, Probing strain-induced electronic structure change in graphene by Raman spectroscopy, Nano letters, 10 (2010) 4074-4079.

Chapter 7

Conclusions

The present thesis work was aimed towards the fabrication of semi-transparent nanostructured copper (Cu) thin films via pulsed laser deposition (PLD) technique exhibiting the surface plasmon resonance (SPR) and nonlinear optical (NLO) properties and the correlation of these with surface structure, growth dynamics, size and shape of the nanoparticles within the film. The viability of these films as surface enhanced Raman spectroscopy (SERS) substrate for metallic single-wall carbon nanotubes (M-SWCNT) is also explored.

The atomic force microscopy (AFM) was used to estimate the particle size and RMS roughness. The surface characteristics and scaling behaviour of these Cu films were studied via height-height correlation function (HHCF) and power spectral density function (PSDF) from the AFM images. The SPR signals in the films were recorded via absorption spectra in UV-visible range of 1 to 4 eV. The Bruggeman effective medium approximation (BEMA) theory was applied to determine the composition of the nanoparticles of copper (NP Cu), oxides and voids whereas the thickness of the interfacial layer and plasmonic behaviour were investigated by applying the appropriate dispersion model via spectroscopic ellipsometer (SE). The multiple oscillators (including SPR) were also unveiled from SE data.

None of the Cu films deposited at room temperature (RT) for the deposition duration of 4, 6 and 8 minutes showed plasmonic behaviour. But, after gradually annealing to a final temperature of 400ºC, these films exhibited plasmonic behaviour. It was observed that the size of the nanoparticle for 4 and 6 minutes duration films were

increased with increasing the annealing temperature whereas that of for 8 minutes duration film remained unchanged. The nature of surface fractal, assessed from the power spectral density function (PSDF), was changed with annealing temperature and the post annealed films to a final temperature of 400ºC, exhibited Brownian fractals. In the SE analysis, BEMA model was applied and the best fitted model for as-deposited films was of two oscillators model (one Lorentz and one Gauss) whereas that of post annealed to 400ºC fitted with four oscillators model (one Lorentz and three Gauss). Also, the void percentage was negligible in the annealed films (except 4 minutes duration) but the other new copper species (Cu (II) and oxides) were evolved. The measured thickness of the films was found to be in the range of ~11 nm to ~32 nm for the deposition time of 4 to 8 minutes respectively.

It was observed from above that the films annealed to a temperature of 400ºC displayed the best plasmonic properties. Therefore another set of films were directly deposited at 400ºC for the deposition time of 6 to 45 minutes in order to study the effect of film thickness on the properties of nanostructured Cu PLD films. The film thickness was found to be ranging from ~33 to 280 nm for the deposition time of 6 to 45 minutes respectively. The AFM images of film were recorded to study the film growth mechanism. The estimated average size of the nanoparticles was ranging from ~14 to 123 nm for the deposition time of 6 to 45 minutes respectively. The scaling exponents α, β, $1/z$ and γ and surface characteristic of the films were determined from HHCF. These values of exponents conveyed that the growth dynamics of PLD Cu films can be best described by combination of local and non-local models under shadowing mechanism and highly sticking substrate. In the SE analysis of 6 to 10 minutes duration films, four oscillators model was found to be the most appropriate similar to that of gradually annealed films.

The SPR peaks obtained from the UV- visible spectra matched well with that of obtained via SE. The interfacial and top oxide layer thicknesses and its oxide nature were also determined from SE analyses.

The effect of substrate temperature and particle size on the third order NLO property of PLD nanostructured Cu thin films were carried out by using modified Z-scan technique under cw He-Ne laser irradiation. The as-deposited RT films did not exhibit any NLO behaviour. The post annealed films exhibited the NLO behaviour and the value of nonlinear refractive index (NLR) coefficient was observed to be increasing with the annealing temperature. All the annealed films exhibited the self-focusing properties and the observed value of NLR was of the order of 10^{-4} cm^2/W. None of these annealed films showed nonlinear absorption (NLA) behaviour. The films deposited directly at a substrate temperature of 400ºC exhibited both NLA and NLR behaviour. The film deposited for 5 min duration exhibited reserve saturation absorption (RSA) behaviour whereas all the other samples displayed saturation absorption (SA) behaviour. The nonlinear absorption coefficient (β), estimated from the open aperture Z-scan data, was found to initially increase from 11.03 to 68.95 cm/W with the increase in size of nanoparticles from 12 to 16 nm, respectively, and thereafter it decreased with the further increase in particle size and goes down to 26.47 cm/W for the particle size of ~ 26 nm. The similar behaviour with particle size was exhibited for the NLR coefficient of these films which exhibited self-focusing properties having the magnitude of the order of 10^{-4} cm^2/W.

Finally, it is observed that the structural and plasmonic properties of films deposited for 4 and 6 minutes duration directly at 400ºC substrate temperature and that of post annealed films to 400ºC (originally deposited at RT) does not show much similarity. But the 8 minutes duration film for both the cases exhibited similar structural and plasmonic properties because both the films were highly dense and had similar average

particle size. Therefore the properties of these thin films are compared in *table 7.1*. Thus one can conclude that it is important to treat the metallic films around the softening temperature of the glass for proper binding with the substrate to obtain the plasmonic properties.

***Table 7.1**: Compared the common features of the 8 minutes duration gradually annealed to 400ºC and directly deposited at 400ºC films*

S.No.	Characterization of PLD Cu thin films	8 minutes duration as-deposited and gradually annealed to a final temperature of 400ºC	8 minutes duration deposited directly at 400ºC
1	Thickness	~ 32 nm	~ 40 nm
2	Fractal nature	Self-affine	Self-affine
3	Surface morphology	• Particle size- ~ 38 nm • No surface diffusion • Surface roughness – 1.2 nm • Dense surface	• Particle size- ~ 23 nm • No surface diffusion • Sticking coefficient ~ 1 • Surface roughness – 1.18 nm • Dense surface
4	SPR	• Peak position- ~ 1.63 eV • Relatively narrow peak	• Peak position- ~ 1.59 eV • Broad peak
5	Ellipsometer	• Four oscillators dispersion • Oscillator energies- 0.80, 1.63, 2.32 and 1.98 eV • Void percentage < 5%	• Four oscillators dispersion • Oscillator energies- 1.63, 1.83, 1.89 and 2.02 eV • Void percentage < 5%
6	Nonlinearity	• NLR coefficient (n_2)- 3.98± 0.63 × 10^{-4} cm^2/W • Self-focusing	• NLR coefficient (n_2)- 4.28± 0.58 × 10^{-4} cm^2/W • Self-focusing

The viability of nanostructured Cu thin film via PLD for SERS substrate was tested on metallic single wall carbon nanotube (M-SWCNT). For this, the SERS samples were fabricated in five different configurations. The Cu film deposited on the glass substrate at 400ºC for one minutes duration via PLD and the M-SWCNT drop casted on the top displayed the maximum enhancement of 90 % in the Raman signal as compared to that of the M-SWCNT drop casted on bare glass. But when Cu coated Si was used as substrate no such enhancement in the Raman signal of M-SWCNT was observed.

Future scopes

The plasmonic peak energy of the PLD Cu thin films was observed to be in the range of 1.3 to 2.4 eV. This can be further tuned and enhanced easily by varying the size and shape of the nanoparticles and forming the periodic structures on the film. Therefore it is proposed to draw the periodic structure on these Cu films via laser lithography in future which will enable propagation of the plasmonic as well as electrical signal simultaneously along a single device.

The third order optical nonlinearity of nanostructured PLD Cu thin films using cw laser is also reported in this thesis. The similar studies are to be taken up for Ag and Au nanostructured thin films. The plasmonic systems are also foreseen as a fast optical devices such as second- (SHG) and third-harmonic generation (THG), nonlinear phase control, nonlinear switching and routing etc. Therefore there is a need to characterize the nonlinear optical properties of these films with nanosecond and femtosecond laser. Further, the nonlinear response of metallic thin films can be increased by making the pattern on the film surface through lithography. These studies will be undertaken in future.

List of Publications

Journal Papers: *Related to thesis work*

1. ***Rahul Kesarwani*** and Alika Khare, "*Assessment of interfacial layer thickness of pulsed laser deposited plasmonic copper thin films via Spectroscopic Ellipsometer*", Optical Materials **93** (2019) 98.

2. **Rahul Kesarwani**, Partha P. Dey and Alika Khare, "*Correlation between surface scaling behavior and surface plasmon resonance properties of semitransparent nanostructured Cu thin films deposited via PLD*", RSC Adv., **9** (2019) 7967.

3. **Rahul Kesarwani** and Alika Khare, "*SPR and NLO behavior of pulsed laser deposited semitransparent Cu thin film*", **Appl. Phy. B**, 124 (2018) 116.

4. Partha P. Dey, **Rahul Kesarwani** and Alika Khare, '*Efficacy of Raman mapping over ellipsometric spectroscopy and XRD for characterization of structurally heterogeneous PLD nc-Si thin films*', Optical Materials **84** (2018) 221–226.

5. **Rahul Kesarwani** and Alika Khare, "*Compositional Study of Pulsed Laser Deposited Semitransparent Cu Thin Film using BEMA*", AIP Conf. Proc. **1942** (2017) 080045.

6. **Rahul Kesarwani**, Harsh Chaturvedi and Alika Khare, "*Plasmonic interaction between copper nanoparticles and metallic single walled carbon nanotubes*", *doi.org/10.1364/PHOTONICS.2016.P1A.18.*

7. **Rahul Kesarwani** and Alika Khare, "*Effect of annealing on the stoichiometry and plasmonic properties of PLD nanostructured semitransparent copper thin film using BEMA*", (to be submitted).

8. **Rahul Kesarwani** and Alika Khare, "*Surface diffusion and fractal analysis of the as-deposited gradually annealed plasmonic Cu thin film using power spectral density function*", *(to be submitted).*

Patent

System, Apparatus and Method for Monitoring of Surface Profile and Thickness Measurement in Thin Films, **Pub no.: WO/2017/098343 and PCT/IB2016/054261**

Conference presentations

1. **Rahul Kesarwani** and Alika Khare, "Photoluminescence of semi-transparent nanostructure copper thin film fabricated via PLD", Research conclave- 2019.
2. **Rahul Kesarwani** and Alika Khare, "Compositional Study of Pulsed Laser Deposited Semitransparent Cu Thin Film using BEMA", 62nd DAE Solid State Physics symposium (DAE- 2017), 2017.
3. **Rahul Kesarwani**, Partha Pritam Dey and Alika Khare, "Characterization of PLD thin film via spectroscopic ellipsometry", Research conclave- 2017.
4. **Rahul Kesarwani**, Partha Pritam Dey and Alika Khare, "Characterization of PLD thin film via spectroscopic ellipsometry", International Conference on Sophisticated Instruments in Modern Research (ICSIMR-2017), 2017.
5. **Rahul Kesarwani**, Harsh Chaturvedi and Alika Khare, "Plasmonic interaction between copper nanoparticles and metallic single walled carbon nanotubes", 13th international conference on Fiber Optics and Photonics- 2016.
6. **Rahul Kesarwani** and Alika Khare, "Surface structural analysis of plasmonic film using power spectral density technique", XL conference of optical society of India, International Conference on Light and Light based Technologies (ICLLT-2016), 2016.
7. **Rahul Kesarwani**, Ashwini K Sharma and Alika Khare, "Ellipsometric technique for determining the thickness and optical constant of thin film", International year of light (IYL-2015), 2015.
8. **Rahul Kesarwani** and Alika Khare, "The effect of annealing on SPR and NLO properties of Semitransparent Copper thin film on glass via PLD", 4th International Conference on Current Developments in Atomic, Molecular, Optical and Nano Physics with Applications (CDMOP-2015), 2015.

9. **Rahul Kesarwani**, G. P. Bharti, Partha P. Dey, **Indrajeet Kumar** and Alika Khare," NLO behaviour of semitransparent Cu thin film deposited by PLD", International conference on Optics & Opto-electronics (ICOL 2014).

Workshops/Schools attended

1. **One- Day Workshop on Vacuum Technology and its Application in Optical Science**, 19th August, 2017 organised by SPIE student chapter, IIT Guwahati.

2. **Department day, Physics 12th March, 2016** organized by the Research Scholar Forum (RSF), Department of Physics, IIT Guwahati.

3. **National workshop on Advanced Probing Techniques in TEM** during 15-16 February 2016 organised by IIT Guwahati.

4. **TEQIP Symposium** to celebrate the 2015 international year of light, 31st October 2015 Organized by Department of Physics, IIT Guwahati.

5. **Quality Improvement Programme (QIP)** Short Course on Micro & Nano Fabrication during 16th to 20th March 2015 orgainzed by IIT Kanpur (India).

6. **DST-SERC School on Nonlinear Optics and Materials** during 3rd to 21st February 2014 organized by SSN College of Engineering and Pondicherry University (India) (attended from 3rd to 9th February).